Christian Gruber, BSc

Photonic Metal Structures via Self-Assembly Processes

MASTERARBEIT

zur Erlangung des akademischen Grades
Diplom-Ingenieur

Masterstudium Technische Physik

Technische Universität Graz

Betreuer:

Univ.-Prof. Dipl.-Ing. Dr.techn. Günther Leising

Institut für Festkörperphysik

Graz, April 2010

Abstract

Patterning of thin metal films with periodic structures in the visible wavelength range has attracted a high level of attention due to the availability of high resolution fabrication techniques such as focused ion beam milling or electron beam lithography. Due to long writing times the obtainable area sizes are small, e.g. a 100×100 µm² sized sub-micrometer periodic structure in a metal film requires a writing time of about 2 days. Beside these costly and time consuming techniques a rather simple and variable approach using the self-assembly of colloidal spheres as template for etching and coating procedures is established.

Based on commercially available, monodispersed polystyrene (PS) sphere suspensions with sphere diameters of 300 nm and 500 nm respectively, the arrangement of the spheres in a close-packed manner in two dimensions is obtained by the drop casting technique and by the dip coating procedure. Optimizing the respective fabrication process, large-area ($\sim$ cm²) monolayers are achieved.

Proceeding from these PS sphere monolayer regions, differently structured thin metal films are fabricated: i) PS sphere monolayers coated with metals like palladium (Pd) and gold (Au) and alternatively with the alloy AuPd and ii) hole arrays of Au. The hole arrays are obtained by a coating procedure with Au subsequent to reactive ion etching in order to reduce the PS sphere diameters while keeping the periodicity constant. The removal of the size reduced spheres yields the particular hole array.

Because of their periodicities in the order of the wavelength of visible light these structures feature interesting optical properties in terms of transmission enhancement and transmission suppression at characteristic wavelengths correlated with the dimensions of the textured structure. The fabricated patterned metal layers are characterized by means of optical microscopy and scanning electron microscopy as well as by optical transmission measurements. The Au hole arrays are further investigated with respect to their electrical resistivity and their dielectric properties.

Regarding the Au hole arrays, the correlation of the optical transmission with the electrical resistivity demonstrates that the optical properties of the metal layer can be dramatically altered while the electrical properties scale with the metal fill factor.

Kurzfassung

Die derzeit verfügbaren lithographischen Produktionsverfahren, wie z.B. fokussierte Ionenstrahl- oder Elektronenstrahllithographie, erlauben die Herstellung von strukturierten Metallschichten, wobei Strukturgrößen und Strukturperiodizitäten kleiner als die Lichtwellenlänge realisiert werden können. Neben diesen aufwendigen Technologien etablierte sich eine relativ simple und flexible Strukturierungsmethode, die auf der Selbstorganisation monodisperser, kolloider Kugeln basiert. Die Anordnung der Kugeln dient dabei als Grundlage für anschließende Ätz- und Beschichtungsverfahren.

Für diese Arbeit werden kommerziell verfügbare, in Wasser gelagerte Kugeln aus Polystyrol (PS) mit Durchmessern von 300 nm und 500 nm mittels zweier unterschiedlicher Verfahren in dichtest gepackten Monolagen angeordnet: Tropfverfahren bzw. Tauchverfahren. Durch Optimierung beider Verfahren konnten Monolagen mit Flächen von einigen cm^2 hergestellt werden. Solche Größenordnungen sind mit den derzeit verfügbaren lithographischen Verfahren unerreicht. Mit fokussierter Ionenstrahllithographie zum Beispiel erzielt man in einem akzeptablen Zeitraum von etwa zwei Tagen ähnlich strukturierte Schichten in einer Größe von ca. $100 \times 100\,\mu m^2$.

Ausgehend von diesen Monolagen werden verschieden strukturierte Metallschichten produziert: i) PS-Kugel-Monolagen beschichtet mit Palladium (Pd), Gold (Au) und der Legierung AuPd sowie ii) regelmäßige Löcherstrukturen in Au-Schichten. Die regelmäßige Anordnung von Löchern entsteht nach einem Ätzschritt, wodurch sich der Durchmesser der PS Kugeln reduziert, anschließender Beschichtung mit Gold sowie dem Entfernen der verbliebenen PS Kugeln. Die Periodizität der Struktur ist durch den ursprünglichen Durchmesser vorgegeben, die Dimension der Löcher kann über die Ätzzeit eingestellt werden.

Aufgrund der periodischen Struktur der Metallfilme erhöht sich für bestimmte Bereiche des sichtbaren Spektrums die Transmission während sie sich für andere Wellenlängenbereiche beinahe zur Gänze verringert. Die hergestellten, strukturierten Metallschichten werden mittels eines optischen Mikroskops und eines Rasterelektronenmikroskops sowie mittels Transmissionsmessungen charakterisiert. An den Lochstrukturen erfolgt auch die Messung der spezifischen elektrischen Leitfähigkeit sowie die Bestimmung der dielektrischen Funktion mittels spektroskopischer Ellipsometrie.

Die Korrelation zwischen der optischen Transmission und der elektrischen Leitfähigkeit an den Lochstrukturen zeigt, dass aufgrund einer periodischen Anordnung von Löchern in Metallschichten deren Transmissionseigenschaften drastisch verändert werden können, währenddessen sich ihre elektrischen Eigenschaften nur dem Flächenfüllgrad entsprechend ändern.

Contents

1 Motivation

The dielectric properties of thin metal layers in the optical wavelength regime can be significantly modified by patterning the layer with a sub-wavelength periodic structure. Although the currently available structuring techniques facilitate even much smaller structure dimensions the obtainable area sizes in general are small due to very long writing times. Nanosphere lithography using the self-assembly of monodispersed spheres as template for etching and coating procedures allows to fabricate metallic hole arrays extended over large areas ($\sim \mathrm{cm}^2$) with sub-micrometer periodicities. Furthermore the tunable periodicity, hole diameter and shape enable tailoring of both the optical and electrical properties.

Since the report of the extraordinary direct transmission of visible light through optically thick sub-wavelength metallic hole arrays in 1998 by [1], a large number of experimental as well as theoretical work has followed. Depending on the periodicity of the array and on the media involved (metal and dielectric), at particular wavelength ranges of the incident light electromagnetic surface waves propagating right at the boundary are excited. These so-called surface plasmons lead to a high electromagnetic field in the surface decaying exponentially both into the metal and into the dielectric. Mediated by these excitations more light can be transmitted through the holes as compared to the light incident on the area occupied by the holes.

The large localized field density at the surface of a sub-wavelength metallic hole array offers a broad spectrum of applications. Some of them are already used in spectroscopy to enhance weak signals, e.g. surface-enhanced Raman spectroscopy [2] or surface-enhanced fluorescence spectroscopy [3], there are reports on a change in the fluorescent lifetime of organic dyes deposited inside the hole arrays [4] and on an efficiency enhancement of an organic light emitting diode with an aluminum hole array as electron-injecting cathode [5].

The used nanosphere lithography suitable for large-area periodical structures in general and for metallic hole arrays in particular is a powerful tool impressing by its simplicity and by the fact that the parameters of the hole arrays can be varied over a wide range: i) in principle usable for all metals which can be deposited as uniform thin film, ii) monodispersed spheres are commercially available with diameters from about 50 nm to several micrometers, iii) different hole diameters are obtainable by different etching times and iv) the metal layer thickness can be varied with respect to sphere diameters.

Tailoring the electrical and dielectric properties of metallic hole arrays, this work targets to establishing a basis for brand-new and innovative device designs.

2 Fundamentals

This chapter summarizes the characteristics of metals with respect to their optical and electrical properties. Considering the bulk material, the variation of its properties as regards thin films and the subsequent patterning of these films are discussed.

2.1 Bulk Metal

Starting with a homogeneous isotropic medium with dielectric function ε, permeability μ, conductivity σ and no charge sources (charge density $\rho = 0$), the dispersion relation of the wavevector and the relationship between the dielectric function and the refractive index are derived. Main part of this section stems from [6], [7] and [8].

Introducing a set of vectors namely the electric field vector $\mathbf{E}$, the magnetic induction $\mathbf{B}$, the electric current density $\mathbf{j}$, the electric displacement $\mathbf{D}$ and the magnetic field vector $\mathbf{H}$, the material equations are represented by:

$$\mathbf{j} = \sigma\mathbf{E}, \quad \mathbf{D} = \varepsilon\mathbf{E}, \quad \mathbf{B} = \mu\mathbf{H}$$

The macroscopic Maxwell equations in SI-units are:

$$\nabla \cdot \mathbf{E} = 0 \tag{2.1}$$

$$\nabla \cdot \mathbf{H} = 0 \tag{2.2}$$

$$\nabla \times \mathbf{E} + \mu\frac{\partial \mathbf{H}}{\partial t} = 0 \tag{2.3}$$

$$\nabla \times \mathbf{H} - \varepsilon\frac{\partial \mathbf{E}}{\partial t} = \sigma\mathbf{E} \tag{2.4}$$

If field is strictly monochromatic with angular frequency ω and wavevector $\mathbf{q}$, the fields are of plane wave form:

$$\mathbf{E}(\mathbf{r}, t) = \mathbf{E}(\mathbf{q}, \omega)\mathrm{e}^{\imath(\mathbf{q}\cdot\mathbf{r}-\omega t)}$$

$$\mathbf{H}(\mathbf{r}, t) = \mathbf{H}(\mathbf{q}, \omega)\mathrm{e}^{\imath(\mathbf{q}\cdot\mathbf{r}-\omega t)}$$

Thus, the macroscopic Maxwell equations simplify to

$$\mathbf{q} \cdot \mathbf{E} = 0 \tag{2.5}$$

$$\mathbf{q} \cdot \mathbf{H} = 0 \tag{2.6}$$

$$\imath\,\mathbf{q} \times \mathbf{E} - \imath\,\omega\mu\mathbf{H} = 0 \tag{2.7}$$

$$\imath\,\mathbf{q} \times \mathbf{H} + \imath\,\omega\varepsilon_0\varepsilon(\omega)\mathbf{E} = \sigma(\omega)\mathbf{E} \tag{2.8}$$

whereby the frequency dependence of the dielectric function $\varepsilon = \varepsilon_0\varepsilon(\omega)$, ε_0 being the permittivity of the free space, and of the conductivity $\sigma = \sigma(\omega)$ is used.

Combination of Eq. 2.7 with Eq. 2.8 yields to

$$\imath\frac{1}{\mu\omega}\underbrace{\mathbf{q}\times\mathbf{q}\times\mathbf{E}}_{\mathbf{q}(\underbrace{\mathbf{q}\cdot\mathbf{E}}_{=0})-\mathbf{E}\mathbf{q}^2} +\imath\,\omega\varepsilon_0\varepsilon(\omega)\mathbf{E}-\sigma(\omega)\,\mathbf{E}=0$$

$$\Rightarrow q^2=\omega^2\mu\varepsilon_0\underbrace{\left[\varepsilon(\omega)+\imath\,\frac{\sigma(\omega)}{\varepsilon_0\omega}\right]}_{\tilde{\varepsilon}} \tag{2.9}$$

This dispersion relation is formally identical to the case of nonconducting media when introducing a complex dielectric function $\tilde{\varepsilon}$ and thus a complex wave vector $\tilde{\mathbf{q}}$ respectively

$$\mathbf{q}\rightarrow\tilde{\mathbf{q}}=\mathcal{N}\mathbf{q}$$

$\mathcal{N}$ indicating the complex refractive index defined as

$$\mathcal{N}=n+\imath k=n\,(1+\imath\kappa) \tag{2.10}$$

$n\ldots$ refractive index
$k\ldots$ extinction coefficient
$\kappa\ldots$ absorption index (2.11)

Thus the dispersion relation (Eq. 2.9) can also be written as

$$\tilde{q}^2=\underbrace{\frac{\omega^2}{\mathrm{c}^2}}_{q^2}\underbrace{\left(\varepsilon(\omega)+\imath\frac{\sigma(\omega)}{\varepsilon_0\,\omega}\right)}_{\mathcal{N}^2} \tag{2.12}$$

Consequently the complex dielectric function $\tilde{\varepsilon}(\omega)$ is related to the complex refractive index $\mathcal{N}$ as follows:

$$\mathcal{N}^2=n^2(1+\imath\kappa)^2=\tilde{\varepsilon}(\omega)=\varepsilon'(\omega)+\imath\,\varepsilon''(\omega) \tag{2.13}$$

splitted in real and imaginary part:

$$\varepsilon'(\omega)=n^2-k^2=n^2(1-\kappa^2) \tag{2.14}$$
$$\varepsilon''(\omega)=\quad 2nk\quad=\quad 2n^2\kappa \tag{2.15}$$

2.1.1 Dielectric function

As described above the dielectric function represents the material response to an external electric field. According to the Drude model (model of free electrons) the conductivity $\sigma(\omega)$ of a metal can be written in the form

$$\sigma_{\mathrm{met}}(\omega) = \frac{\sigma(0)}{1 - \imath\omega\tau} \tag{2.16}$$

$$\sigma(0) = \frac{n_{\mathrm{el}} \mathrm{e}^2 \tau}{m^*_{\mathrm{el}}} \ldots \text{ DC conductivity in the model of free electrons}$$

$\tau \ldots$ mean collision time (relaxation time), $n_{\mathrm{el}} \ldots$ electron density

$\mathrm{e} \ldots$ elementary charge, $m^*_{\mathrm{el}} \ldots$ mean electron mass

The Drude model considers the conducting electrons as free moving particles. Thus by applying an external electric field these electrons would not notice a restoring force. m^*_{el} accounts for the forces induced by the periodic potential of the crystal.

Applying this to the complex dielectric function (Eq. 2.9) and considering $\varepsilon'(\omega)$ as the contribution of the bounded electrons to the dielectric function one ends with

$$\begin{aligned}
\tilde{\varepsilon}(\omega) &= \varepsilon'(\omega) + \imath \frac{\sigma_{\mathrm{met}}(\omega)}{\varepsilon_0\, \omega} \\
&= \varepsilon'(\omega) - \frac{\sigma(0)}{\varepsilon_0(\imath\omega + \omega^2\tau)} \\
&= \varepsilon'(\omega) - \frac{n_{\mathrm{el}}\, \mathrm{e}^2}{\varepsilon_0 m^*_{\mathrm{el}}} \frac{1}{\imath\frac{\omega}{\tau} + \omega^2} \\
&= \varepsilon'(\omega) - \frac{\omega_{\mathrm{p}}^2}{\omega^2 + \imath\frac{\omega}{\tau}}
\end{aligned} \tag{2.17}$$

$$\omega_{\mathrm{p}} = \sqrt{\frac{n_{\mathrm{el}}\, \mathrm{e}^2}{\varepsilon_0 m^*_{\mathrm{el}}}} \quad \ldots \text{ plasma frequency}$$

The plasma frequency indicates a resonant longitudinal plasma oscillation of the conductive (free) electrons. A plasmon being the quantum of such an oscillation and can be excited either by reflection of an electron or a photon or by passing an electron through a thin metal film. The frequency range of the plasmons is determined by the vanishing of the respective dielectric function.

In reality the dielectric function of a metal can differ significantly from this simple model because it doesn't account for electron - lattice interactions (interband transitions) as well as for electron - phonon or electron - lattice defects interactions (intraband transitions). The measured optical constants, i.e. the refractive index and the extinction coefficient, of hosts of solids are provided for a broad spectral range by [8]. According to the relationship to the optical constants (Eq. 2.14 and 2.15) the dielectric function can be calculated. Fig. 2.4 shows the dielectric function of different metals in the UV/visible spectral range.

2.1.2 Refraction and Reflection at a Metal Surface

Considering the propagation of a plane wave from a dielectric into a conductor, the boundary between the media infinitely large extended, the Fresnel amplitude reflection coefficients are

$$r_\mathrm{s} = -\frac{\sin(\theta_\mathrm{i} - \theta_\mathrm{t})}{\sin(\theta_\mathrm{i} + \theta_\mathrm{t})} = \rho_\mathrm{s} \cdot \mathrm{e}^{\imath\phi_\mathrm{s}} \tag{2.18}$$

$$r_\mathrm{p} = \frac{\tan(\theta_\mathrm{i} - \theta_\mathrm{t})}{\tan(\theta_\mathrm{i} + \theta_\mathrm{t})} = \rho_\mathrm{p} \cdot \mathrm{e}^{\imath\phi_\mathrm{p}} \tag{2.19}$$

the subscripts s and p indicate the polarization of the incident electric field vectors in reference to the plane of incidence spanned by the wavevector $\mathbf{q}$ and the surface normal vector. θ_i corresponds to the incident angle, θ_t is a complex value and related to the θ_i according to Snell's law of refraction

$$\sin(\theta_\mathrm{t}) = \frac{\sin(\theta_\mathrm{i})}{\mathcal{N}} \tag{2.20}$$

The complex reflectance ratio ρ can be expressed as

$$\rho = \frac{r_\mathrm{p}}{r_\mathrm{s}} = \frac{\rho_\mathrm{p}}{\rho_\mathrm{s}} \cdot \mathrm{e}^{\imath(\phi_\mathrm{p} - \phi_\mathrm{s})} = \tan(\psi) \cdot \mathrm{e}^{\imath\Delta} \tag{2.21}$$

with an amplitude $\tan(\psi)$ and a phase Δ. In general this equation permits the evaluation of the complex refractive index $\mathcal{N}$ and consequently the dielectric function $\tilde{\varepsilon}(\omega)$ of a metal by means of ellipsometry. Taking advantage of the change in intensity and polarization of light reflecting from the surface of a material, a defined incident beam hits the sample while a detector monitors the amplitude $\tan(\psi)$ and the phase Δ of the reflected light beam. Details about this technique are described in the experimental chapter 3.1.4.

If light hits a metallic surface the amplitude will damped exponentially (example for z-direction):

$$\mathrm{e}^{\imath(\tilde{q}z - \omega t)} = \underbrace{\mathrm{e}^{\imath(nqz - \omega t)}}_{\text{plane wave}} \cdot \underbrace{\mathrm{e}^{-kqz}}_{\text{damping}}$$

Based on the energy density I of an electric field

$$I = \|\mathbf{E}(\mathbf{r}, t)\|^2 = \|\mathbf{E}(\mathbf{q}, \omega)\|^2 \, \mathrm{e}^{-2kqz} \tag{2.22}$$

the definition of the absorption coefficient α (when $I = \frac{I_0}{\mathrm{e}}$) results in

$$\alpha = 2kq = \frac{4\pi k}{\lambda_0} \tag{2.23}$$

and the penetration depth in

$$\delta_\mathrm{pen} = \frac{1}{\alpha}\,. \tag{2.24}$$

The skin depth is the attenuation length of the amplitude of the electric field (when $E = \frac{E_0}{\mathrm{e}}$)

$$\delta_\mathrm{skin} = \frac{1}{\mathrm{Im}\,\tilde{q}} = \frac{1}{2\,\delta_\mathrm{pen}}\,. \tag{2.25}$$

2.1.3 Surface Plasmons

Besides the collective oscillations of conductive electrons in a metal, known as plasmons, also free surface charges at the boundary between a metal and a dielectric can be excited resonantly provided that the involved media (metal and dielectric) have a dielectric function of opposite sign. These charge oscillations, called as surface plasmons (SP), possess their maximum at the surface and decay exponentially both into the metal and into the dielectric (Fig. 2.1).

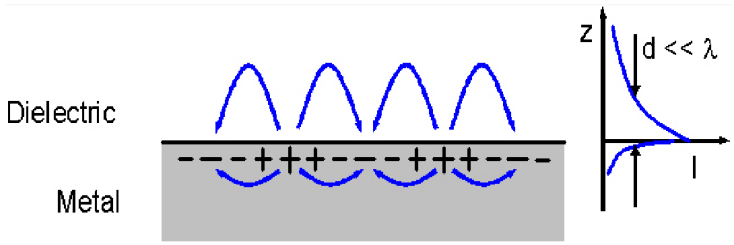

Figure 2.1: Schematic drawing[1] of the field distribution of surface plasmons at a metal - dielectric interface (left picture) and their intensity distribution in the direction perpendicular to the interface (right picture)

The fundamental properties of surface plasmons are treated in [9]. Their dispersion relation results from continuity relations of the electric and magnetic field at the metal - dielectric boundary:

$$k_{\mathrm{SP}} = k \sqrt{\frac{\varepsilon_{\mathrm{m}} \varepsilon_{\mathrm{d}}}{\varepsilon_{\mathrm{m}} + \varepsilon_{\mathrm{d}}}} \tag{2.26}$$

$k \ldots$ wave vector of the incident beam (light or electrons)
$\varepsilon_{\mathrm{m}} \ldots$ dielectric function of the metal
$\varepsilon_{\mathrm{d}} \ldots$ dielectric function of the dielectric

This equation expresses the sensitivity of surface plasmons to the dielectric function of both media (metal and dielectric).

With respect to an incident light beam this dispersion relation (depicted in Fig. 2.2) lies always below the light line $\omega = \mathrm{c}\, k$ (dashed blue line in the figure), c being the speed of light. Consequently the excitation requires an additional coupling of the SP with the incident photons e.g. via corrugation or roughness offering the necessary momentum $\mathbf{G}$.

This coupling of light with SP excite surface plasmon polaritons (SPP) and leads to a strong enhancement of EM-field in the surface (resonance amplification) as can be seen at Fig. 2.1. Ideal metals in the visible spectral range with a high absolute value of the real part and a small imaginary part of the dielectric function ε_{m} such as Ag and Au give rise to a strong enhancement and a minimization of losses.

[1] Image taken from the homepage of Center for Probing the Nanoscale, Standford University on March 17, 2010

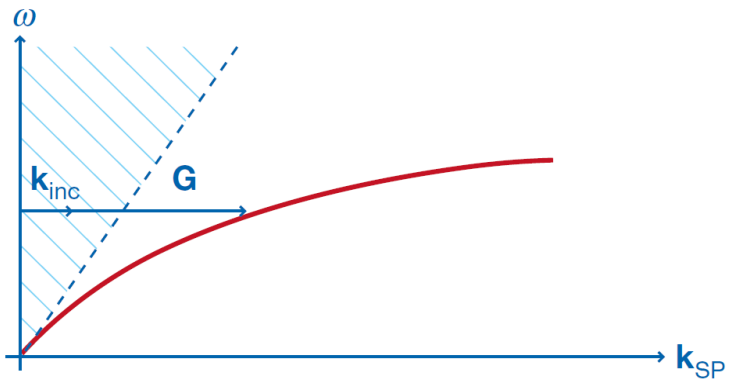

Figure 2.2: Dispersion relation of surface plasmons, image from [10]

2.2 Metallic Thin Films

Producing thin metal layers with thicknesses from a few nanometers to several micrometers, the entire range of coating procedures can be applied which are categorized into

- ▷ physical deposition techniques
  e.g. thermal evaporation, sputter deposition, laser ablation
- ▷ chemical deposition techniques
  e.g. chemical vapor deposition, plating

The properties of a thin metal film can differ significantly from the properties of the bulk material because thin films in general exhibit more imperfections and lattice defects. Furthermore the larger surface to bulk ratio as well as a possible differing packaging density influence their properties.

The optical properties (reflectance, absorption and transmission) are also associated with the skin depth of the incident electromagnetic field (Eq. 2.25) when the amplitude drops by a factor of $\frac{1}{e}$. In the optical wavelength region Au and Ag can be considered as ideal metals (a high absolute value of the real part ε' and a small imaginary part ε'' of the dielectric function) yielding to skin depths in the range of 20 - 40 nm [11].
The Center for Nanolithography Research of the Rochester Institute of Technology has investigated the optical properties of several thin metal films by means of spectroscopic ellipsometry combined with spectrophotometry [12]. Fig. 2.3 shows the refractive indices and extinction coefficients of 4 different metal films each 100 nm thick and fabricated by RF magnetron sputtering: gold (Au), silver (Ag), palladium (Pd) and platinum (Pt). The complex dielectric functions deduced from the optical constants according to Eq. 2.14 and 2.15 are plotted in Fig. 2.4.

Regarding the electrical properties, the resistivity results from the scattering of the electrons by the lattice, the average distance between two collisions is called the mean free path. At room temperature this mean free path for metals is in the range of 10 - 50 nm [13]. If the film thickness becomes compareable to the mean free path the collisions at the surface contribute significantly to an increase of the electrical resistivity. Also impurities and lattice imperfections influence the electrical properties of thin metal films.

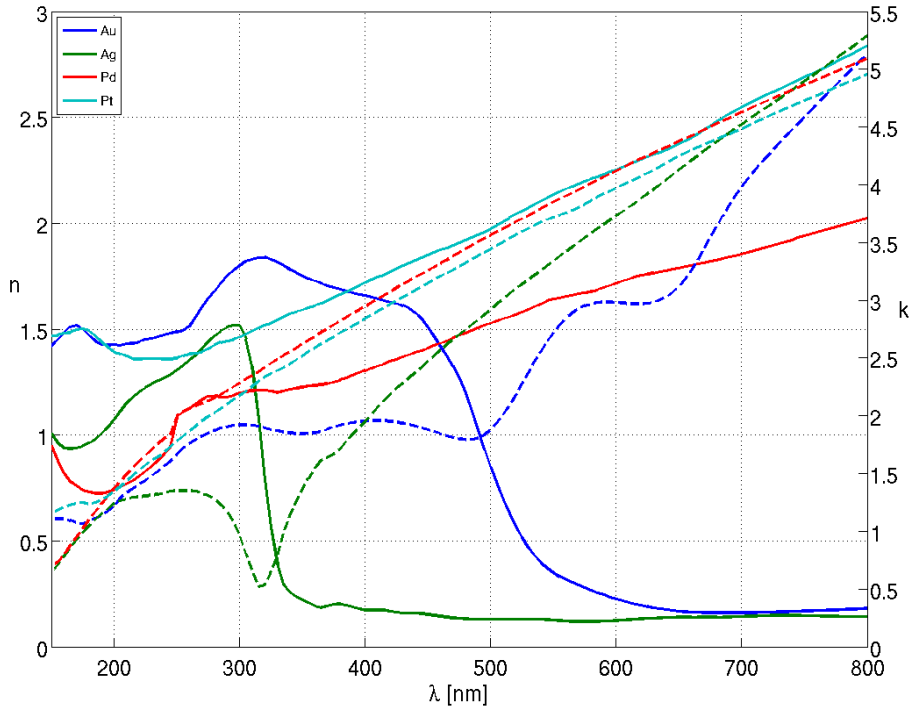

Figure 2.3: Refractive indices n (solid lines) and extinction coefficients k (dashed lines) in UV and visible spectral range of 4 different metals: Au, Ag, Pd and Pt

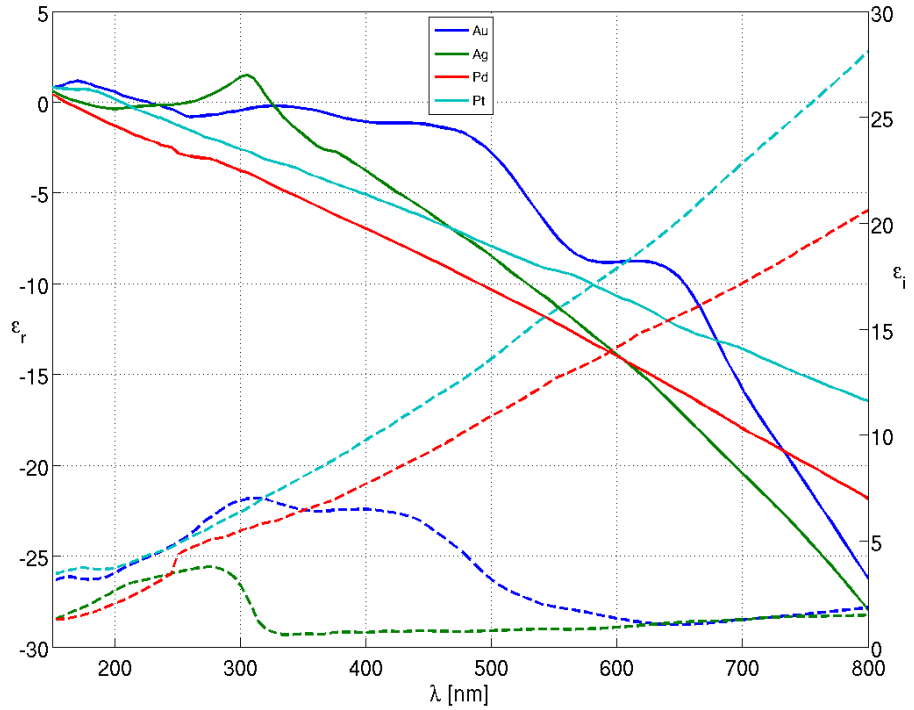

Figure 2.4: Dielectric function $\varepsilon = \varepsilon' + \imath\varepsilon''$ (ε' . . . solid lines, ε'' . . . dashed lines) in UV and visible spectral range of 4 different metals: Au, Ag, Pd and Pt

2.3 Photonic Crystals

Photonic crystals possess a periodical modulation of the dielectric function (or equivalently of the index of refraction) at least in one dimension. The topic is comprehensively treated in the textbook [14]. A photonic crystal is the photonic pendant to electrons moving in a periodic electric field inside a crystal. Propagating as wave, light has to fulfill the periodic 'potential' offered by the photonic crystal resulting in a photonic band structure. In the case of a complete band gap the propagation of light in a certain direction through this photonic crystal can be prevented and thus in principle the propagation of light can be controlled.

A periodical modulation of the refractive index in one dimension known as a stack of dielectric layers features a wide range of applications using its reflective properties, e.g. as high-reflection laser mirror, or its anti-reflective properties, e.g. anti-reflection coating of glasses.

A two-dimensional photonic crystal is periodically extended in two directions and homogeneous in the third direction, e.g. photonic-crystal fibers, a new class of optical fibers. In general the layers exhibit periodical structures in two dimensions but with finite thickness in the third. In the strict sense these hybrid structures are known as photonic-crystal slabs. These include for instance a monolayer of close-packed monodispersed spheres with diameters in the range of the visible wavelength or a metallic hole array with a hole periodicity of the same order. Focusing on both structures and being of crucial importance for the understanding of their dielectric properties, the associated reciprocal lattice vectors are explicitly deducted in the next section.

Nature provides fascinating photonic crystals with a periodical modulation of the dielectric function in three dimensions, e.g. in the form of opals, butterfly wings and moth eyes. Their color impression also refered as structural colors is based on a mixture of interference effects, diffraction and scattering [15]. Artificially fabricated 3d photonic structures like a woodpile stack of orthogonal dielectric columns or a multilayer of close-packed monodispersed spheres in principle enable to influence the propagation of light in all three dimensions. Assuming a high contrast of the dielectric functions, a complete photonic band gap material is realizable leading to prohibit the propagation of light in any direction of any polarization.

2.3.1 Reciprocal 2D Lattice Vectors

On the basis of unit vectors of the real lattice $\mathbf{a}_1$ and $\mathbf{a}_2$ one can derive the associated reciprocal lattice vectors $\mathbf{b}_1$ and $\mathbf{b}_2$.

$$\mathbf{a}_1 = \begin{pmatrix} a_{11} \\ a_{12} \end{pmatrix}, \ \mathbf{a}_2 = \begin{pmatrix} a_{21} \\ a_{22} \end{pmatrix}$$
$$\mathbf{b}_1 = \begin{pmatrix} b_{11} \\ b_{12} \end{pmatrix}, \ \mathbf{b}_2 = \begin{pmatrix} b_{21} \\ b_{22} \end{pmatrix}$$

They are related via

$$\boxed{\mathbf{a}_i \cdot \mathbf{b}_j = 2\pi\delta_{ij}}, \tag{2.27}$$

for the different components arise

$$
\begin{aligned}
a_{11}\,b_{11} + a_{12}\,b_{12} &= 2\pi \\
a_{21}\,b_{21} + a_{22}\,b_{22} &= 2\pi \\
a_{11}\,b_{21} + a_{12}\,b_{22} &= 0 \\
a_{21}\,b_{11} + a_{22}\,b_{12} &= 0
\end{aligned}
$$

or in matrix form

$$
\underbrace{\begin{pmatrix} a_{11} & a_{12} \\ a_{21} & a_{22} \end{pmatrix}}_{A} \cdot \begin{pmatrix} b_{11} & b_{21} \\ b_{12} & b_{22} \end{pmatrix} = 2\pi \begin{pmatrix} 1 & 0 \\ 0 & 1 \end{pmatrix}.
$$

Using

$$
A^{-1} = \frac{1}{\|A\|} \begin{pmatrix} a_{22} & -a_{12} \\ -a_{21} & a_{11} \end{pmatrix}
$$

$$
\|A\| \ldots \text{determinant of } A
$$

results in

$$
\begin{bmatrix} b_{11} & b_{21} \\ b_{12} & b_{22} \end{bmatrix} = \frac{2\pi}{\|A\|} \begin{pmatrix} a_{22} & -a_{12} \\ -a_{21} & a_{11} \end{pmatrix} \tag{2.28}
$$

or in vector notation

$$
\mathbf{b}_1 = \frac{2\pi}{\|A\|} \begin{pmatrix} a_{22} \\ -a_{21} \end{pmatrix} \tag{2.29}
$$

$$
\mathbf{b}_2 = \frac{2\pi}{\|A\|} \begin{pmatrix} -a_{12} \\ a_{11} \end{pmatrix} \tag{2.30}
$$

For a 2d hexagonal lattice (left-hand side of Fig. 2.5) with lattice vectors

$$
\begin{aligned}
\mathbf{a}_1 &= P\left(\cos\frac{\pi}{3}\hat{\mathbf{x}} + \sin\frac{\pi}{3}\hat{\mathbf{y}}\right) = P\left(\frac{1}{2}\hat{\mathbf{x}} + \frac{\sqrt{3}}{2}\hat{\mathbf{y}}\right) \\
\mathbf{a}_2 &= P\left(\cos\frac{\pi}{3}\hat{\mathbf{x}} - \sin\frac{\pi}{3}\hat{\mathbf{y}}\right) = P\left(\frac{1}{2}\hat{\mathbf{x}} - \frac{\sqrt{3}}{2}\hat{\mathbf{y}}\right)
\end{aligned}
$$

the reciprocal lattice vectors

$$
\mathbf{b}_1 = \frac{4\pi}{\sqrt{3}P} \begin{pmatrix} \frac{\sqrt{3}}{2} \\ \frac{1}{2} \end{pmatrix} \tag{2.31}
$$

$$
\mathbf{b}_2 = \frac{4\pi}{\sqrt{3}P} \begin{pmatrix} \frac{\sqrt{3}}{2} \\ -\frac{1}{2} \end{pmatrix} \tag{2.32}
$$

yield again a hexagonal lattice depicted on the right-hand side of Fig. 2.5.

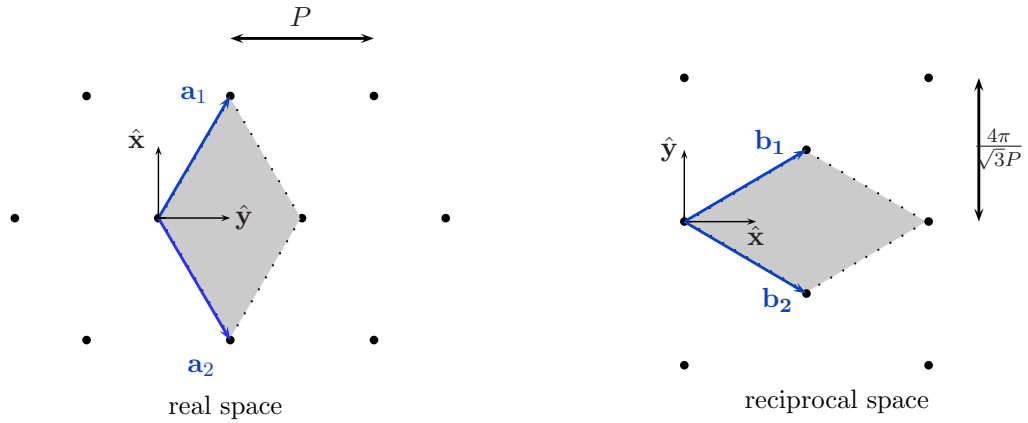

Figure 2.5: Unit Cell of a Hexagonal 2D lattice

2.4 Patterned Metallic Thin Films - Metallic Hole Arrays

In principle all types of fabrication approaches suitable for periodical patterning of thin metal films with dimensions in the visibible wavelength range can be applied such as

- ▷ focused-ion beam milling,
- ▷ electron beam lithography,
- ▷ photolithography, and
- ▷ molding and printing techniques, e.g. nanoimprint lithography.

Beside these costly and time-consuming approaches a rather simple and unconventional bottom-up method is used in this work, namely the so-called 'nanosphere lithography' or 'natural lithography' comprehensively illustrated in the section *Fabrication Methods*, whereby the self-assembly of colloidal particles serves as template for etching and coating procedures.

2.4.1 Extraordinary Transmission of Visible Light

In 1998 Ebbesen and co-workers [1] have reported transmission resonances in sub-wavelength hole arrays of an opaque Ag film with 200 nm thickness. The achieved transmission efficiencies η at the particular resonances exceed 1 normalized to the hole area meaning that more light is transfered through the holes as compared to the light incident on the area occupied by the holes. Since then a lot of practical as well as theoretical work can be found in literature. Main aspects of this topic are reviewed in [10], [16], [17] and [18]. The remainder of this section is based on this review articles.

The extraordinary transmission is believed to be mediated by the coupling of the incident light to surface plasmons. These can either be propagating surface plasmon polaritons (SPP) or localized surface plasmons (LSP). According to [18] the resonant transmission of light through a sub-wavelength hole array can be thought as follows:

1. the apertures couple the incident light into evanescent modes on both sides of the metal layer that are bounded on the surface

2. stored energy at the surface builds up

3. re-scattering of the stored energy from the back side

It's important to mention that besides the resonant transmission the metallic hole array enables non-resonant transmission as well, i.e. the direct transmission through the single apertures. The apertures have waveguide properties which could be propagative or evanescent depending on their lateral dimensions. The cutoff wavelength identifying the transition between propagation and evanescence is related to the cross-section of the aperture. With metals this cutoff is not sharply defined due to the penetration of the field inside the walls of the waveguide.
The two transmission contributions, the resonant (SP excitation) and the non-resonant (direct), interfere and produce Fano-type line shapes [19].

As mentioned in section 2.1.3 the excitation of SPP by light requires an additional momentum $\mathbf{G}$. Momentum conservation leads to

$$\mathbf{k}_{\mathrm{SP}} = \mathbf{k}_{\parallel} + \mathbf{G} \tag{2.33}$$

with $\mathbf{k}_{\parallel}$ being the portion of the incident wavevector that lies in the plane of the metal film and $\mathbf{G}$ a reciprocal lattice vector associated with the periodic surface structure.

For a hexagonal lattice (section 2.3.1) $\mathbf{G}$ looks like

$$\begin{aligned}\mathbf{G} &= n_1\mathbf{b}_1 + n_2\mathbf{b}_2 \\ &= \frac{4\pi}{\sqrt{3}P}\begin{pmatrix}\frac{\sqrt{3}(n_1+n_2)}{2} \\ \frac{n_1-n_2}{2}\end{pmatrix} \\ & n_1,\ n_2 \ldots \text{integers}\end{aligned}$$

If one illuminates the metallic hole array at normal incidence ($\mathbf{k}_{\parallel} = \mathbf{0}$) and combines the dispersion relation of SP (Eq. 2.26) with the momentum conservation (Eq. 2.33) an approximation for the transmission peaks can be given as follows:

$$k\sqrt{\frac{\varepsilon_{\mathrm{m}}\varepsilon_{\mathrm{d}}}{\varepsilon_{\mathrm{m}}+\varepsilon_{\mathrm{d}}}} = \frac{4\pi}{\sqrt{3}P}\sqrt{n_1^2+n_1n_2+n_2^2}$$

$$\text{with } k = \frac{2\pi}{\lambda}$$

$$\boxed{\lambda = \frac{P}{\sqrt{\frac{4}{3}\left(n_1^2+n_1n_2+n_2^2\right)}}\sqrt{\frac{\varepsilon_{\mathrm{m}}\varepsilon_{\mathrm{d}}}{\varepsilon_{\mathrm{m}}+\varepsilon_{\mathrm{d}}}}} \tag{2.34}$$

This approximation represents only a rough estimation because it doesn't account neither for the layer thickness t nor for the hole sizes and hole shapes. Furthermore the dielectric function depicted in Fig. 2.4 varies strongly within the considered spectral range (UV-A, visible and near IR) as well as for the different metals.

Measuring resonances, the layer thickness should exceed the finite penetration depth of EM field into metal (Eq. 2.24) but the holes should not be too deep as the surface waves on both sides are coupled via evanescent waves through them. In ultrathin sub-wavelength Au hole arrays ($t = 20\,\text{nm}$) the reverse is true: the transmission is even suppressed [20].

Beside the hole thicknesses also their size and shape affect both the localized SP mode and the cutoff wavelength above which no propagation of light is enabled.

As already mentioned above the theory of extraordinary transmission of light through sub-wavelength hole arrays mediated by surface plasmons is not fully accepted throughout the scientific community. Critics claim that for some geometries the SP play if any only a marginal role in the EOT process [21]. The authors of this paper conclude that the wavefronts transmitted by the single holes interfere and lead to the enhanced transmission. This transmission is mainly influenced by i) surface plasmons excited at the cylinder walls (rotating along circumference and propagating along the axis of the cylinder) and ii) the penetration of the incident light into the metal.

Summing up the extraordinary transmission of visible light through metallic hole arrays, the positions of transmission resonances are determined mainly by the hole periodicity and the dielectric functions of the materials involved. The respective intensity varies strongly with material, layer thickness and hole size/shape.

2.4.2 Applications

As seen in the previous section the resonance positions of the transmission through metallic hole arrays with periodicities in the range of the visible wavelength strongly depend on the dielectric environment too. This sensitivity facilitates to monitor a change of the dielectric function of the environment by a shift of the resonance wavelengths as e.g. demonstrated by an absorption of molecules at a gold hole array [22]. This method is called surface plasmon resonance sensing.

Originating from the excitation of surface plasmons, the intense electromagnetic field in the surface of sub-wavelength metallic hole array (resonance amplification) enables besides the extraordinary transmission of light further applications such as

- ▷ surface-enhanced Raman spectroscopy [2],
- ▷ surface-enhanced fluorescence spectroscopy [3],
- ▷ change of the fluorescent lifetime of organic dyes deposited inside the hole arrays [4] and
- ▷ efficiency enhancement of organic light emitting diodes [5].

3 Experimental

This chapter is structured into two main sections: in the first one the used tools to characterize the produced metal films both structured and unstructured layers are described in detail, the second section gives an insight into details of the fabrication process. The actual fabrication procedures are outlined in the chapters *Fabrication of Sphere Monolayers* and *Fabrication of Metallic Hole Arrays*.

Major parts of the fabrication procedures are performed at the laboratory of the institute except the reactive ion etching step which is executed at Institute of Nanostructured Materials and Photonics (Joanneum Research Forschungsgesellschaft mbH, Graz).

3.1 Characterization Methods

This section comprehensively illustrates the equipment applied to characterize the fabricated samples. While thickness measurements performed at the profilometer or by means of x-ray reflectivity as well as optical microscopy and scanning electron microscopy deal with the physical parameters of the samples, transmission spectroscopy, specific resistivity measurements and spectroscopic ellipsometry provide information about their physical nature.

3.1.1 Thickness Measurements

For the determination of the thickness of the deposited metal layers at a substrate two totally different techniques are used: x-ray reflectivity as non-contact method and a profilometer whose stylus touches the layer. While the profilometer directly measures the layer thickness, one has to model the x-ray refectivity data to determine the thickness.

3.1.1.1 Profilometer

The profilometer measurements are executed at the Institute of Nanostructured Materials and Photonics (Joanneum Research Forschungsgesellschaft mbH, Graz) using a Dektak 150 from Veeco Instruments Inc. (Plainview, USA) including PC and Dektak Software.

This profilometer allows to measure film thicknesses down to a few nanometers. As the sample to be measured moves underneath a diamond stylus which is in mechanical contact with its surface, the change in height is recorded as DC signal. Measuring the thickness of a thin (metal) layer on a substrate with a profilometer, the respective scan range has to contain both an area with and without the film.

The operator can adjust via the Dektak Software the measurement position, the scan length, the scan time and the applied force to the stylus. For the fabricated metal films within a thickness range between 20 and 120 nm the following settings are applied:

scan length:	400 to 1200 µm
scan time:	20 to 40 s
force:	3 - 7 mg
stylus radius:	12.5 µm / 2.5 µm

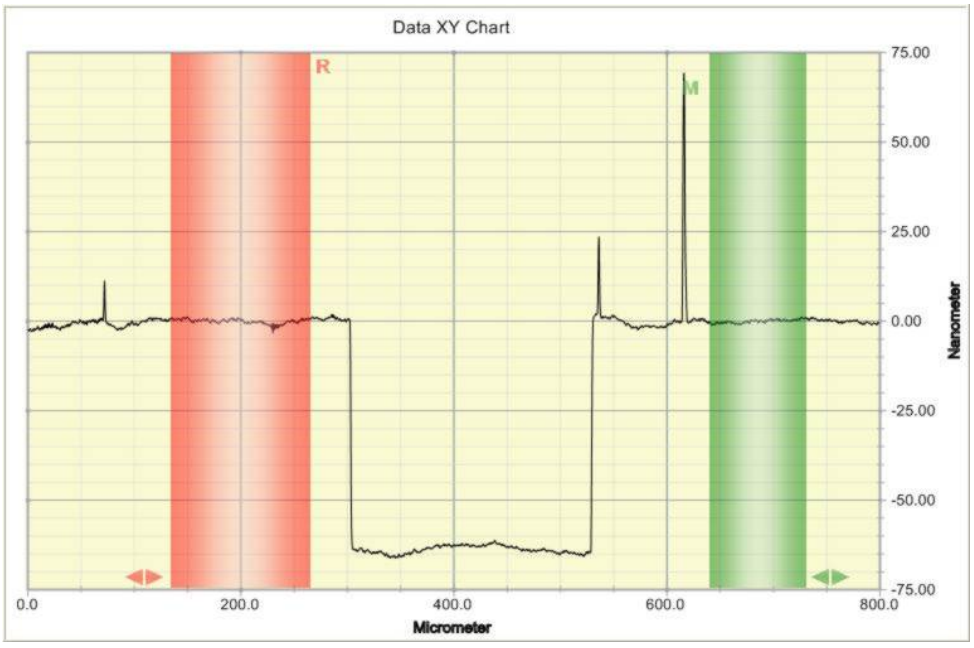

Figure 3.1: Typical step profile of a scratch in a metal film, recorded by a Dektak 150

In order to estimate the mean film thickness as well as the measurement errors of one sample, the film thickness is measured at 3 different positions at a distance of approximately 1 cm. At each position 5 measurements within 500 µm are performed. The measurement errors result from the mean of the measurement errors of the single measurements.

3.1.1.2 X-ray Reflectivity

The thickness measurements by means of x-ray reflectivity are performed by the group of professor Resel from the Institute of Solid State Physics. This non-destructive measurement technique enables to estimate roughness and thickness of thin layers independent of the material.

The setup is a Bruker D8 Discover diffractometer in Bragg Brentano configuration using an x-ray beam from a copper anode sealed tube with its characteristic wavelength $\lambda = 1.5406\,\text{Å}$ which is focused on the sample surface. The reflected beam intensity is monitored as a function of twice the incident angle (defined as angle between surface and beam) for small angles. The layer thickness d results from the distance of the minima of the Kiessig fringes [23]:

$$d = \frac{\lambda}{2\sin(\theta_1) - \sin(\theta_2)} \tag{3.1}$$

$\theta_1, \theta_2 \ldots$ position of minima

A representative characteristic of the reflection intensity as a function of twice the incident angle is depicted at Fig. 3.2.

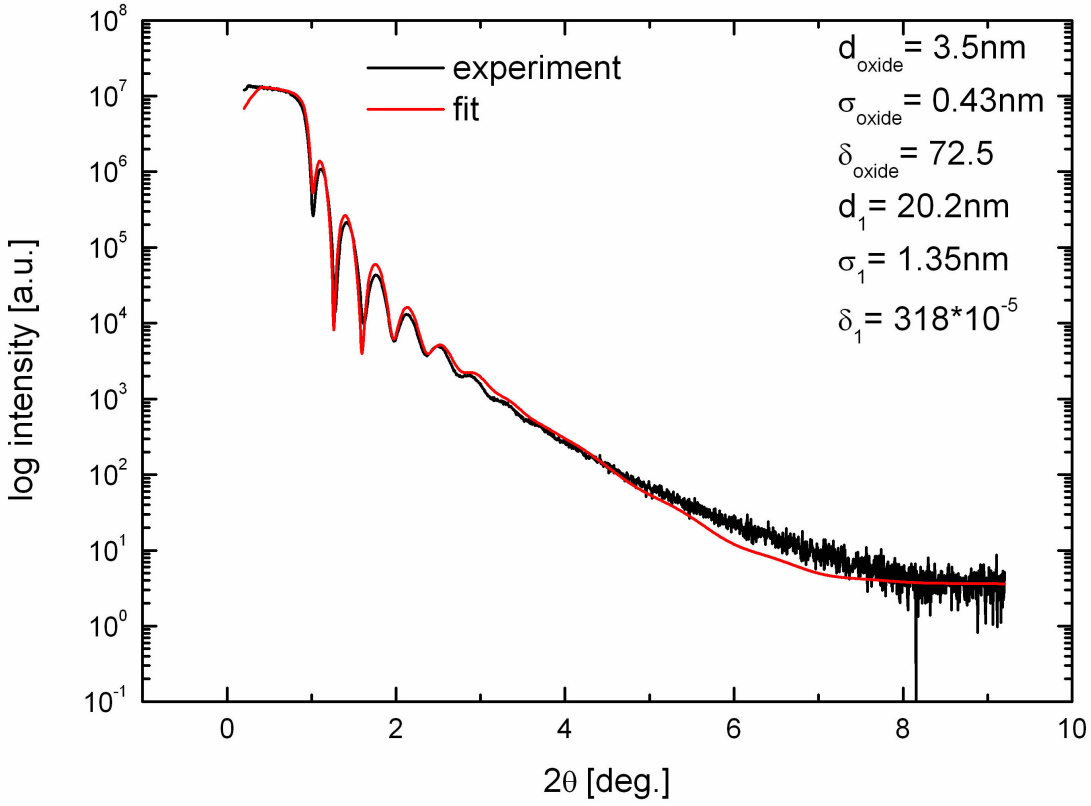

Figure 3.2: Reflection intensity of a platinum layer on top of a glass substrate as function of twice the incident angle θ, recorded by a Bruker D8 Discover diffractometer

The error of the thickness measurements by means of x-ray reflectivity are slightly overestimated with 5 %.

3.1.2 Microscopy

3.1.2.1 Optical Microscopy

The photonic structure of the samples due to the periodical modulation of the refractive index (sphere arrangement) as well as the size of the single structures in the range of the visible wavelength enable probing by means of the optical microscope. The optical microscope serves as quick and potential first characterization tool.

For this work the microscope from the institute is used:

model:	BX51 from Olympus (Tokio, Japan)
observation:	reflection and transmission
digital camera:	Olympus Camedia C-5060 WideZoom
software:	Olympus DP-Soft 5.0
ocular:	WH10×/22
object lenses:	UMPlanFI: (magnification / numerical aperture)
	5×/0.15, 20×/0.46, 50×/0.80, 100×/0.95

The resolution of an optical microscope defined as the distance d of two point objects just separated observable is determined by the used wavelength λ as well as by the numerical aperture ($NA = n \sin\theta$) of the lenses indicating their angular aperture, n being the index of refraction and θ the half acceptance angle:

$$d = \frac{\lambda}{2NA} \tag{3.2}$$

Assuming $NA = 0.95$ and $\lambda = 380\,\text{nm}$, the lowest obtainable distance d for an optical microscope is in the order of 200 nm.

3.1.2.2 Scanning Electron Microscopy

The investigations of the samples are carried out at the Institute for Electron Microscopy of the TU Graz using the scanning electron microscopy (SEM) ULTRA 55 from Carl Zeiss NTS GmbH (Oberkochen, Germany).

Analyzing a sample by means of SEM, an electrically conductive surface connected to the electrode is favorable to minimize charging of the sample. An electron beam focused on the sample scatters as the beam penetrates its surface. Due to interaction processes a variety of output is generated, e.g. photons, backscattered electrons, secondary electrons and Auger electrons. The interaction between the electron beam and the sample depends on the energy of the beam as well as on the electron density of the sample.

As regards imaging of the sample surface, the secondary electrons are detected and due to a continuing scan across the surface the image is formed. The ULTRA 55 enables a resolution of approximately 1 nm at the used electron acceleration voltage of 5 kV. The working distance is chosen to 2 mm.

3.1.3 Transmission Spectroscopy

The transmission experiments are performed applying two different approaches: a CCD spectrometer attached to a home-made fiber optics setup and a two beam spectrophotometer. Both measure the direct transmission meaning that the incident beam and the transmitted beam are collinear.

3.1.3.1 CCD-Spectroscopy

Recording transmission spectra within a small sample area ($< 500 \times 500$ µm^2), a home-made setup (Fig. 3.3) is constructed which allows spatially resolved measurements.

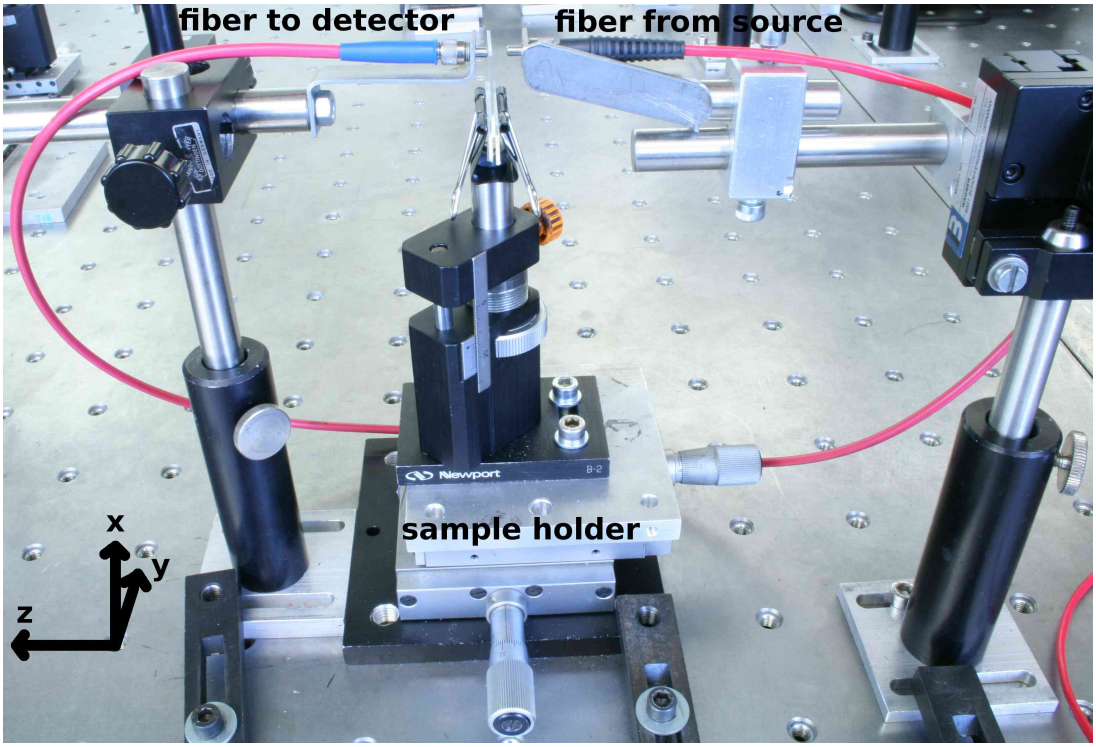

Figure 3.3: Home-made setup that enables spatially resolved transmission measurements

The sample (layer surface towards source) is mounted on a precision sample holder which is manually adjustable in y- and z-direction with 10 µm accuracy, in x-direction with 100 µm accuracy. A specimen area of 20×25 mm^2 (x- and y-direction) can be measured without repositioning of the sample.

Both light source and detector are attached to the setup via optical fibers. As light source serves a Deuterium-Halogen Light Source DH-2000 from Top Sensor Systems (Eerbeek, Netherlands) connected with a FC-UV600-2 fiber from Ocean Optics Inc. (Dunedin, USA) - core diameter:

600 µm, numerical aperture (NA): 0.22. The light source is switched on about one hour before measuring to achieve a stabilized light intensity throughout the measurements.

Two different detectors are used depending on the respective application:

detector 1: Fiber Optic Spectrometer S2000 from Ocean Optics Inc. (Dunedin, USA)
2048-element linear CCD-array detector
detector range: 200 - 1100 nm

optical fiber: FC-UV200-2 - core diameter: 200 µm, NA: 0.22
software: OOIBase, version 1.5.09
distance of source fiber to sample: ≈ 5 mm

detector 2: MS-125 1/8m spectrograph (grating: 600 grooves/mm) connected to an Instaspec IV (Model 78430-V) from Oriel Instruments (Stratford, USA)
1024×128 element CCD-array detector
cooled to -20 °C for a better signal/noise ratio

optical fiber: core diameter: 200 µm, NA: 0.22
software: Andor MCD, version 2.2
distance to source fiber sample: ≈ 4 cm

The different distance of the source fiber to the sample results from the fixed integration time at detector 2 of 19 ms. The integration time of detector 1 is variable down to 7 ms.

Both detectors collect the direct transmitted light at the backside of the sample at a distance of $l \approx 100$ µm corresponding to the thickness of an ordinary printer paper. This distance and the fiber properties (the numerical aperture of a fiber is depicted at Fig. 3.4) yield to an effective measurement area with radius

$$x = l \tan\theta + \frac{d}{2} \tag{3.3}$$

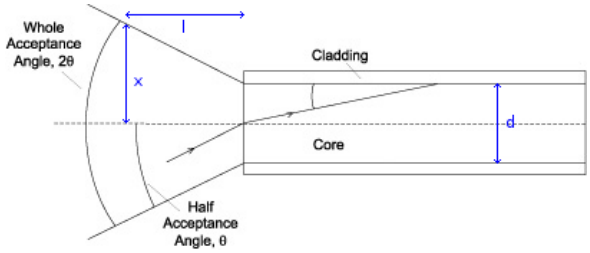

Figure 3.4: Numerical aperture[1]: $NA = n \sin(\theta)$
$n \ldots$ refractive index, $d \ldots$ core diameter,
$x \ldots$ radius of effective measurement area at a given distance l

Thus the acceptance angle of $2\theta \approx 25\,^\circ$ ($NA = 0.22$) results in a effective circular measurement area of approximately 350 µm in diameter.

[1]modified picture taken from the homepage of Ocean Optics Inc. (Dunedin, USA) on March 8, 2010

3.1.3.2 Spectrophotometry

Transmission measurements of samples with homogeneous area sizes larger than $\approx 10 \times 5\,\mathrm{mm}^2$ are performed with the double beam spectrophotometer Lambda 9 from Perkin-Elmer Inc. (Waltham, USA) too:

light sources:	Deuterium lamp (UV), Tungsten-Halogen lamp (VIS/NIR)
detectors:	photomultiplier (UV/VIS), PbS detector (NIR)
wavelength range:	185 - 3200 nm
beam height:	10 mm (reduction to 5 mm possible)
beam width:	≈ 2 mm @ 2 nm optical slit width
beam divergence:	$\approx 10\,^\circ$
substrate holder:	cuvette holder, sample fixed with double sided adhesive tape at the entrance face

The larger effective beam area of about $10 \times 2\,\mathrm{mm}^2$ in comparison to the home-made fiber optics setup described in the previous section as well as the more inaccurate positioning of the sample require an extended and homogeneous measurement field. Satisfying these prerequisites, one can take advantage of the augmented wavelength range from UV to near IR.

3.1.4 Spectroscopic Ellipsometry

The ellipsometric measurements and the corresponding modeling are performed by Dr. Georg Jakopic from the Institute of Nanostructured Materials and Photonics (Joanneum Research Forschungsgesellschaft mbH, Graz) using a VASE ellipsometer from J.A. Woolam Co., Inc. (Lincoln, USA) including PC and WVASE32 Software. The ellipsometer as non-constructive measurement method enables the estimation of the dielectric function as well as the determination of the thickness of thin films.

The VASE is a rotating analyzer ellipsometer with an autoretarder (phase compensator) in the incident beam line. As light source serves a high-pressure xenon lamp combined with a scanning monochromator (slit width variable). The detector is a Si-/GaAs tandem photodiode.

The monochromatic incident beam with a fixed amplitude and polarization is reflected from the sample through the rotating analyzer onto the detector. The time-periodical intensity signal at the detector can be recorded at various angles of incidence. The interaction of the light with the sample leads to a change of both the amplitude and the phase depending on the material properties. Separating the polarization state of the incident and the reflected beam into a p- and s-polarized part with respect to the plane of incidence, the ratio of the reflection coefficients (see 2.1.2 for details) enables an estimation of optical constants or thicknesses assumed that an electrodynamical model describes their relation.

3.1.5 Specific Resistivity Measurement

Knowing the film thickness of a solid sample, one can use the Van der Pauw method [24], a four point probe measurement, to obtain the specific resistivity. A schematic drawing shown in Fig. 3.5 illustrates the measurement setup. Applying a constant current between 2 neighboring contacts (A and B), the voltage drop along the other two contacts (C and D) is monitored. This procedure will be repeated changing the contact situation: current between B and C, voltage drop between D and A.

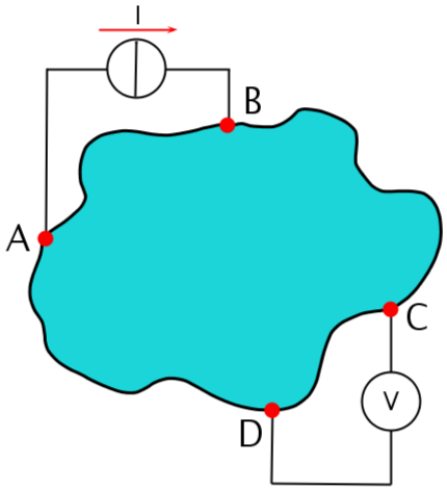

Figure 3.5: Schematic drawing of the measurement setup to obtain the specific resistivity by means of the Van der Pauw method: a sample of arbitrary shape including the contacts A and B to apply a constant current I while measuring the voltage drop V between the contacts C and D.

In principle this method requires the following conditions:

- ▷ contacts at circumference of sample
- ▷ contacts sufficiently small
- ▷ homogeneous sample thickness
- ▷ no islands within the sample

According to Van der Pauw the specific resistivity ρ results in

$$\rho = \frac{\pi\, d}{\ln(2)} \frac{R_{\mathrm{AB,CD}} + R_{\mathrm{BC,DA}}}{2} f\left(\frac{R_{\mathrm{AB,CD}}}{R_{\mathrm{BC,DA}}}\right) \tag{3.4}$$

whereby $R_{\mathrm{AB,CD}}$ and $R_{\mathrm{BC,DA}}$ respectively are the resistances calculated by means of Ohm's law by applying a current between contact A and B (B and C respectively) and measuring the voltage drop along contact C and D (D and A respectively). The correction factor f corresponding to the geometry of the contacts is quoted in [24] as a function of the ratio of the resistances.

The specific resistivity measurements are performed using a 225 Current Source and a 2000 Multimeter from Keithley Instruments Inc. (Cleveland, USA). Regarding the measurement

errors the manufacturer indicates an accuracy of:

225 current source (stability):	±(0.02 % of reading + 0.005 % of range)
2000 multimeter:	±(0.004 % of reading + 0.0035 % of full range)

The samples are mounted upon a conductor plate contacted via a 30 µm thick gold wire with conductive gold at the sample and conductive silver at the conductor plate pad respectively. The whole setup is shown at Fig. 3.6.

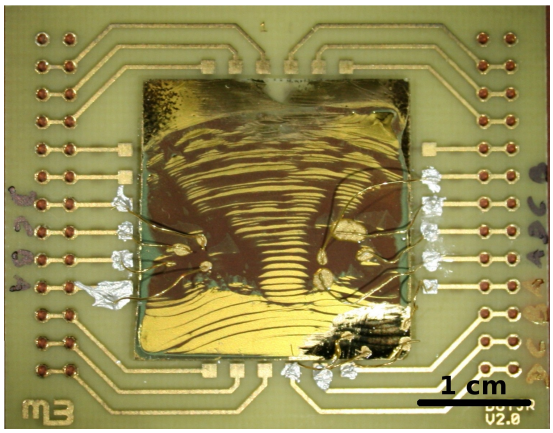

Figure 3.6: Setup for the 4 point probe measurement

3.2 Fabrication Methods

The fabrication of metallic hole structures is obtained via nanosphere lithography. The wide size range of available colloidal particles (30 nm to 250 µm in sphere diameter) enables a large variety of possible structures.

On one hand nanosphere lithography facilitates different nanoparticle structural motifs, an overview is given by [25], on the other one can also obtain periodically patterned thin films, especially metallic thin films - the aim of this thesis.

Starting with the self-assembly of colloidal particles in monolayer regions on a substrate as template, reactive ion etching (RIE) is followed to reduce the particle sizes. The remained structure serves as mask for the coating procedure. The metallic hole array is achieved by a lift-off process of the reduced particles covered with metal.

In this section the necessary steps to obtain a patterned thin metal film are explained in detail using polystyrene spheres as colloidal particles. Schematic drawings of the main fabrication steps are depicted at Fig. 3.7.

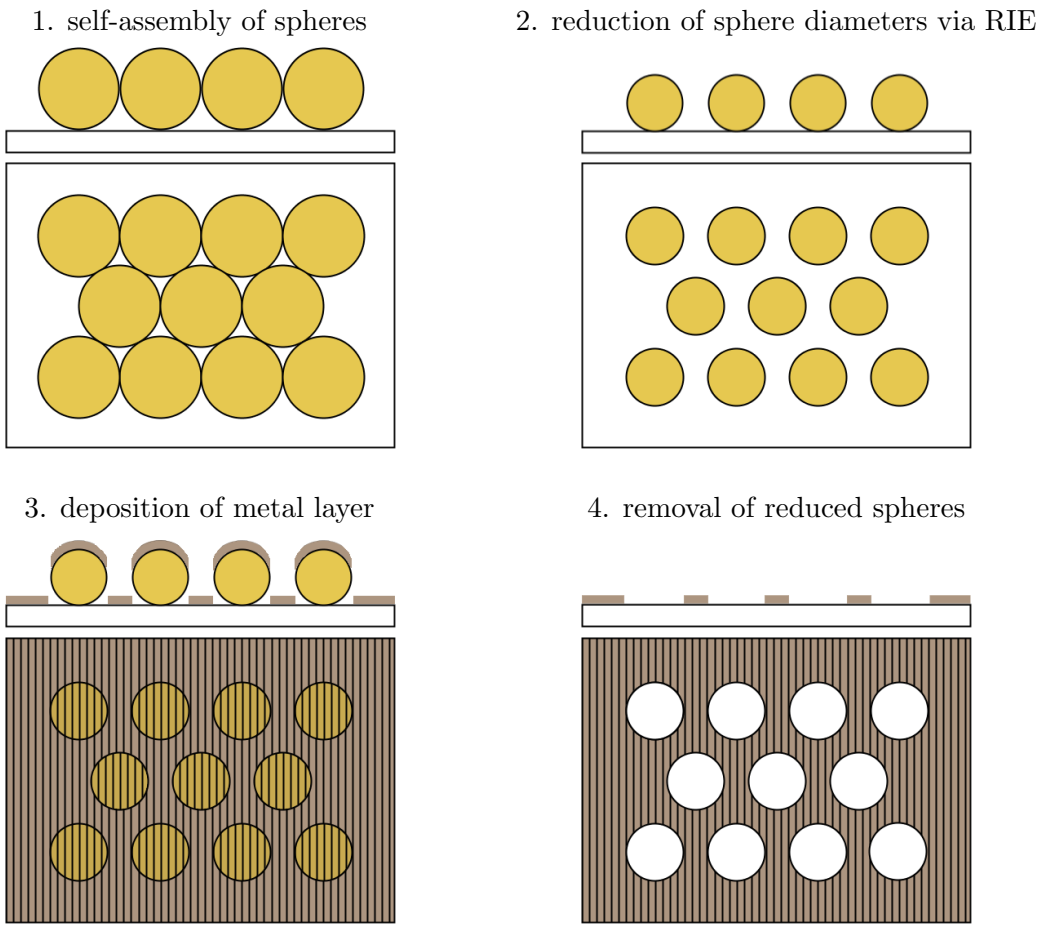

Figure 3.7: Schematic drawings of the respective fabrication steps, top view and side view

3.2.1 Self-Assembly of Polystyrene Spheres

Since the early 1980's colloidal particles are used in the fabrication of periodical sub-micrometer structures. Two review articles, one from Xia et al. [26] the other from Burmeister et al. [27], provide an insight into the extensive field of self-assembly of colloidal spheres and their potential applications. As the self-assembly of polystyrene (PS) spheres serves as template for the further process the remainder of this section is focused only on the self-assembly in two dimensions, i.e. in monolayer regions.

Xia et al. [26] summarizes the research activities in the field of monodispersed colloidal spheres, i.e. production, organization of colloidal spheres into two- or three-dimensionally ordered lattices and applications. Concerning the organization of the spheres in a close-packed two-dimensional manner, different experimental approaches are possible:

a) arrangement at an air-liquid interface via long-range attractive interactions,
b) arrangement on the surface of a solid electrode via electrophoretic deposition and
c) arrangement in a thin liquid film on a solid substrate via attractive capillary forces.

According to Burmeister et al. [27] the most promising fabrication methods concerning the assembly via attractive capillary forces are spin coating, drop casting and dip coating.

All these methods start with a monodispersed PS suspension, mainly 10 % solids, which are commercially available ranging from 30 nm to 250 µm in sphere diameter - suppliers amongst others are: Thermo Fisher Scientific Inc. (Waltham, USA) or microParticles GmbH (Berlin, Germany).

The self-assembly of spheres results in a variety of different arrangements: randomly or close-packed, close-packed in monolayers or multilayers. This work is aimed at producing large areas of close-packed PS spheres in monolayers. Burmeister et al. [27] report area sizes in the range of cm^2. These areas exhibit a multicrystalline structure with defect-free, monocrystalline domains from 10 to 100 μm^2 in size.

The process of self-assembling implies a series of arrangement defects like point defects (missing spheres) and line defects (slip dislocations). Another crucial requirement of close-packed assembly represents the monodispersity of the sphere properties, i.e. diameter, surface shape and internal structure. The size dispersion of the PS spheres in the suspension is indicated as coefficient of variation (c.v.) defined as the standard deviation related to the mean sphere diameter. For sphere diameters between 200 nm and 1 µm the suppliers quote a c.v. $\leq 3\,\%$. As will be demonstrated later, this size dispersion essentially limits the area of defect-free domains.

Nevertheless the nanosphere lithography provides a simple, inexpensive and potential fabrication technique of area sizes in the range of cm^2 with sub-micrometer periodicities.

3.2.1.1 Number of Particles per Area / per Volume

Based on hexagonally close-packed spheres (Fig. 3.8) one can obtain the area which one sphere occupies. The red rhombus shows the unit cell of this 2-dimensional crystal structure containing only one sphere.

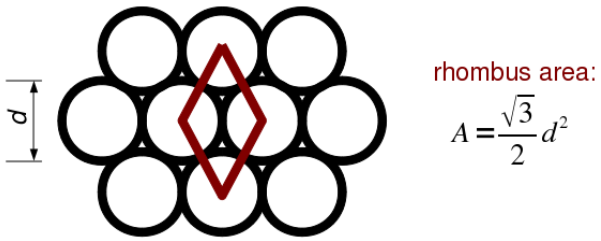

Figure 3.8: Hexagonally close-packed, 2-dimensional sphere arrangement including the unit cell

The number of particles per milliliter n_{ml} is determined by the suspension parameters following this equation (from Thermo Fisher Scientific Inc.[2])

$$n_{\mathrm{ml}} = \frac{6\rho_{\mathrm{w}}}{d^3\pi\left(\rho_{\mathrm{w}} + \frac{\rho_{\mathrm{p}}}{C} - \rho_{\mathrm{p}}\right)} \tag{3.5}$$

$C \ldots$ particle concentration of polystyrene in suspension (% solid per weight)
$\rho_{\mathrm{w}} \ldots$ density of water in g/cm^3
$\rho_{\mathrm{p}} \ldots$ density of suspension in g/cm^3
$d \ldots$ diameter of polystyrene spheres in cm

As example for a 500 nm diameter PS suspension (10 % solids)

$$d = 5 \cdot 10^{-5}\,\mathrm{cm},\ C = 0.1,\ \rho_{\mathrm{w}} = 1.00\,\mathrm{g/cm^3},\ \rho_{\mathrm{p}} = 1.05\,\mathrm{g/cm^3}$$

the number of particles per milliliter n_{ml} and per microliter $n_{\mu\mathrm{l}}$ respectively results in

$$n_{\mathrm{ml}} = 1.46 \cdot 10^{12}$$
$$n_{\mu\mathrm{l}} = 1.46 \cdot 10^{9}$$

so that 1 µl of a 500 nm PS suspension (10 % solids) would yield to a close-packed monolayer area of (Fig. 3.8 evinces the sphere arrangement including the unit cell)

$$A_{2\mathrm{d}} = n_{\mu\mathrm{l}}\, A$$
$$= 3.17\,\mathrm{cm}^2$$

[2]Technical note TN-017.04 'Derivation of Count per Milliliter from Percentage of Solids'

3.2.1.2 Fabrication Method Drop Casting

A suspension of PS spheres is spread onto a horizontal, flat, clean and wettable substrate. The substrate area determines the amount of suspension so that the whole substrate is covered. As the suppliers only provide suspensions with a fixed concentration, mostly 10 % solids, the dilution of the suspension has to be adapted to the substrate size. The starting point of the dilution ratio represents the number of particles per area / per volume (section 3.2.1.1). Large monolayer areas are achieved by a 2 up to 5 times lower dilution ratio as theoretically necessary.

The ordering process starts as the liquid layer thickness approaches the diameter of the spheres. Few spheres organize themselves to a small nucleus (sphere cluster) due to surface tension effects that pull the spheres together. As the evaporation process continues attractive capillary forces (small menisci formed between the nucleus and surrounding spheres) lead to a convective transport of further spheres towards the nucleus and agglomeration at the sphere cluster. Thus in general the spheres arrange themselves in a hexagonally close-packed manner [28].

Computer simulations (molecular dynamics) of a spring-block stick-slip model successfully reproduce the experimentally observed sphere arrangements and the dynamics of the ordering process [29]. The uncontrollable and thus non-homogeneous nanosphere density on the substrate leads to different patterns, e.g. hexagonally structures or square lattices, as well as dislocation lines and crystallization defects on the same sample.

Producing highly ordered monolayer regions of PS spheres requires the control of the influencing parameters on the evaporation process of the liquid part of the suspension, i.e. the vapor pressure and the temperature. By encapsulating the whole system (substrate holder and substrate) in a small volume which prevents from the external air turbulences too, the ambient conditions are kept fairly constant. Nevertheless the evaporation process by itself, i.e. the evaporation rate, is not accessible. Schematic drawings of different phases of the evaporation process on a horizontal substrate depicts Fig. 4.11: the evaporation starts at the corners and proceeds towards the center.

High quality ordering as well as large domain sizes are favored by a flat, clean and chemically homogeneous surface of the substrate as well as by the ability of the spheres to slide (migrate) on the substrate before drying.

An additional tilting of the substrate by a small angle enables a more defined rate of evaporation starting from the upper edge of the substrate [30]. The tilting angle strongly influences the speed of the evaporation and the arrangement of the PS spheres in monolayer or multilayers. The larger the tilting angle the less substrate area is covered with spheres after evaporation.

In general the advantage of this method is its simplicity and the non-requirement of any special apparatus. Once the dilution ratio is adopted to the substrate size one is able to reproduce the PS sphere arrangement if one maintains the ambient conditions fairly constant.

3.2.1.3 Fabrication Method Dip Coating

A flat, clean and wettable substrate is vertically dipped into a PS suspension and in a next step slowly withdrawn at a constant velocity. This method again requires the control of the ambient conditions, i.e. vapor pressure and temperature.

The ordering process as well as the method considered by itself was extensively investigated by Dimitrov et al. [31]. The wettability of the substrate favors to form a wetting film (meniscus) upwards the substrate. The water evaporation at substrate-air-suspension contact line leads to a continuous convective transfer of spheres towards the wetting film. As the film thickness approaches the sphere diameter small menisci (sphere clusters) are formed and with continuing evaporation capillary forces between the sphere clusters and single spheres in the immediate vicinity leads to an enlargement of the clusters in terms of a close-packed arrangement. In the stationary state the PS spheres start to organize themselves in monolayers and successive multilayers from the top of the meniscus down to the bulk suspension. The arrangement only in monolayers can be achieved if the withdrawing rate equals the monolayer formation rate.

As opposed to drop casting this method enables a direct control of the evaporation rate. Due to the different color impressions of layers illuminated with white light, each layer exhibit another coloring, one could in principle adjust the withdrawing rate to the ambient conditions, i.e. concentration of spheres in the suspension, vapor pressure and temperature to achieve large-area sized monolayer regions.

According to [31] array formation requires

- ▷ wettability of substrate by the suspension
- ▷ ability of the spheres to slide (migrate) on the substrate before drying
- ▷ a stable suspension - negligible sinking of spheres (relevant for diameters above $\approx 1\,\mu m$)
- ▷ high vapor pressure to prevent aggregation of spheres at the suspension surface
- ▷ slow evaporation of liquid component of suspension at the meniscus

For this thesis the NANO DIP ND-0407 from SDI Company Ltd. (Kyoto, Japan) is used as dip coater. The processing speed can be varied from 0.01 - 2000 µm/s and an effective stroke of 50 mm is possible.

The tower consisting of the stepper motor and the substrate holder is encapsulated in a perspex box to ensure constant ambient conditions and prevention of external air flow during the withdrawing process. The whole setup is depicted at Fig. 3.9. Furthermore the humidity inside the box is managed by depositing plastic boxes containing water - a tissue dipped in the water increases its surface. On top of the tower temperature and humidity are measured. The stepper motor is connected via wire to the control unit outside of the perspex box.

The tower is placed on top of a stiff table frame horizontally aligned to prevent the coupling of external vibrations.

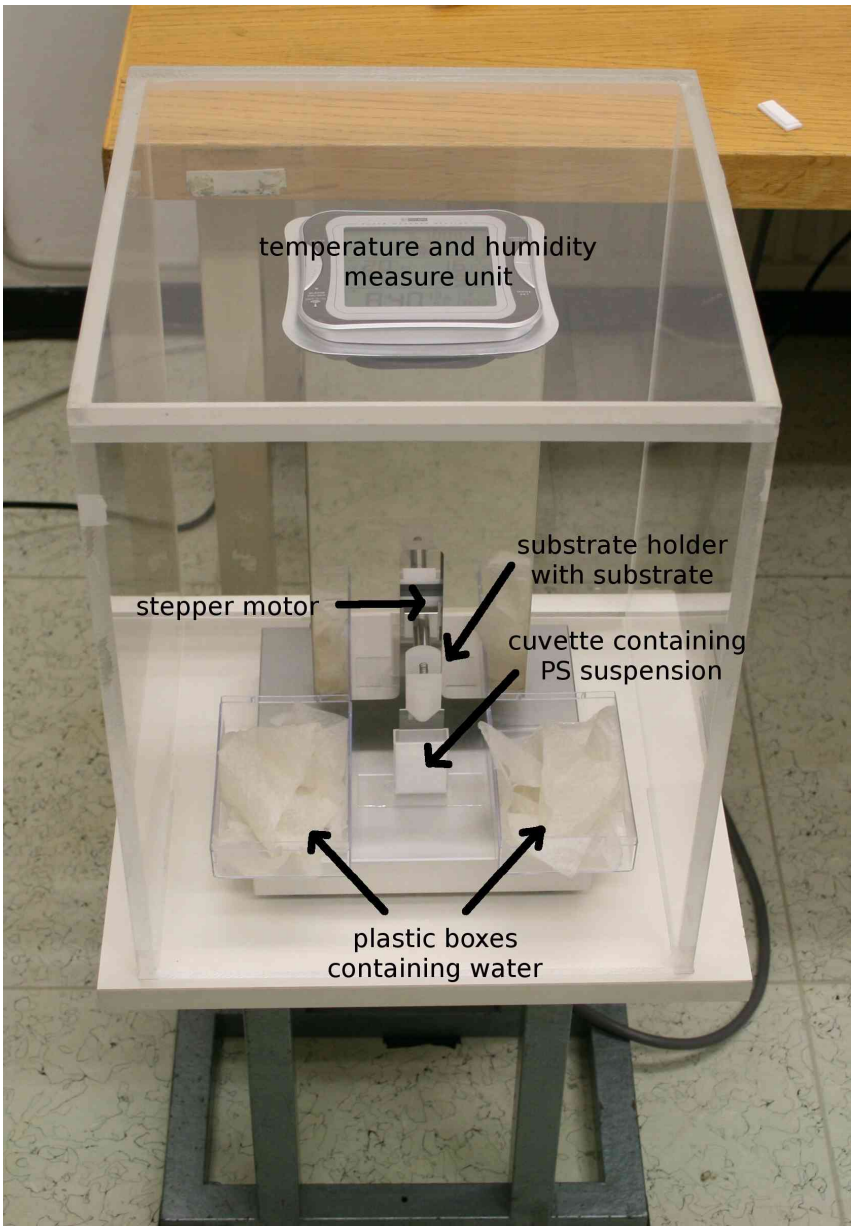

Figure 3.9: Setup of the used NANO DIP ND-0407 dip coater encapsulated in a perspex box. The dipcoater is controlled by a control unit (not visible at this picture) connected to the tower via wire.

3.2.2 Reactive Ion Etching

Reactive Ion Etching (RIE) [32] as plasma-based dry etching technique combines physical sputtering with the chemical reactivity of the used etching gas.

The etching gas, e.g. argon, oxygen or tetrafluoromethane, is injected into the evacuated etching chamber. A strong electromagnetic field (RF, frequency 13.56 MHz) induces an ionization of the gas molecules. After ignition of the plasma a self bias between the two electrodes forms due to the higher mobility of electrons in contrast to ions. Depending on the RF power and the process pressure this self bias leads to a drift of reactive iones towards the negatively charged substrate electrode. The material removal of the sample placed on this electrode occurs on one hand due to the ion bombardment of the sample at the electrode on the other hand due to the chemical reaction of the ions with the sample surface. A schematic drawing of a RIE chamber is depicted at Fig. 3.10.

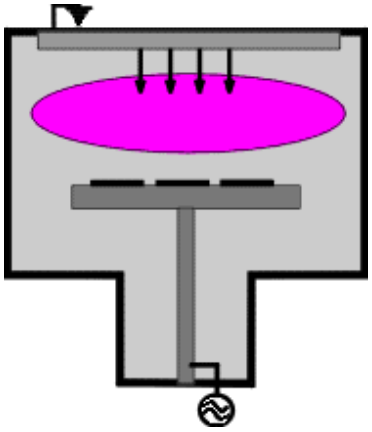

Figure 3.10: RIE chamber[3] - gas injected through gas inlets in top electrode, RF field leads to negative self bias on lower electrode which serves as substrate holder too

Applying this technique Haginoya et al. [33] reduced the PS sphere diameters using oxygen as reactive gas - different sphere diameters were achieved by varying the etching time while keeping the other process parameter, i.e. pressure, RF power and gas flux, constant.

The etching procedure for this work is performed using the Plasmalab 80plus from Oxford Instruments Plasma Technology Ltd. (Bristol, UK) with the following parameters:

gas:	oxygen
pressure:	100 mTorr
RF power:	100 W
O_2-flux:	30 cm^3/s

Varying the etching time enables to tune the PS sphere diameter but the period of the obtained structure is determined by the initial sphere diameter used for the monolayer arrangement. SEM images on Fig. 3.11 and 3.12 demonstrate the reduction in PS sphere diameters.

[3] picture taken from the homepage of Oxford Instruments GmbH (Wiesbaden, Germany) on January 12, 2010

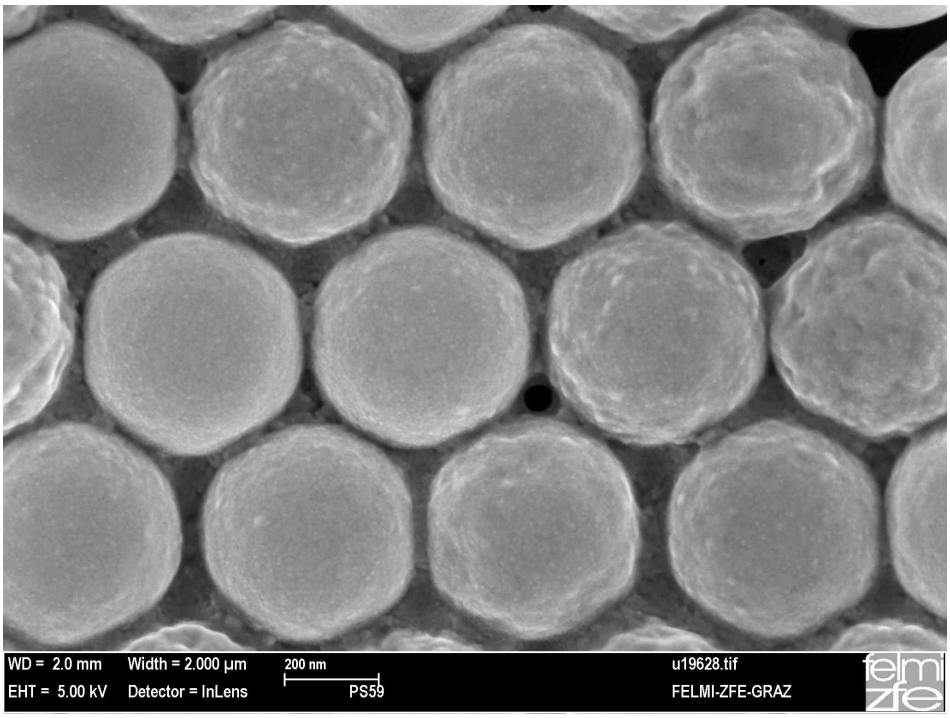

Figure 3.11: SEM image showing a close-packed monolayer of PS spheres (diameter: 500 nm) before the reactive ion etching procedure

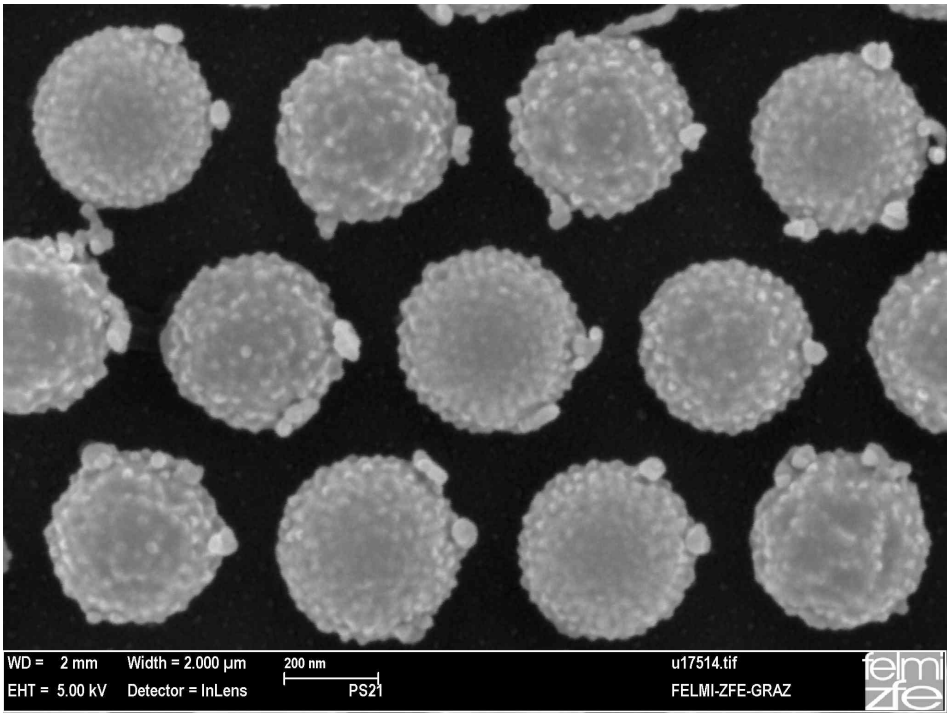

Figure 3.12: SEM image showing a close-packed monolayer of PS spheres (diameter: 500 nm) after the reactive ion etching procedure

3.2.3 Coating Procedures

In principle all kinds of thin metal film deposition techniques could be applied. In this thesis the metal layers are prepared by means of sputter deposition and thermal evaporation due to their availability in the laboratory.

3.2.3.1 Sputter Deposition I

The metals of interest such as platinum and palladium both have a melting point above 1500 °C, therefore the deposition technique of choice is sputtering.

For this work the DC magnetron sputtering device of the laboratory (Fig. 3.13) is used:

device name:	MED 010
manufacturer:	Balzers Union, Liechtenstein
target materials:	platinum (Pt), $\rho = 21.45\,\mathrm{g/cm^3}$
	palladium (Pd), $\rho = 12.023\,\mathrm{g/cm^3}$
thickness monitoring:	quartz crystal microbalance with frequency meter

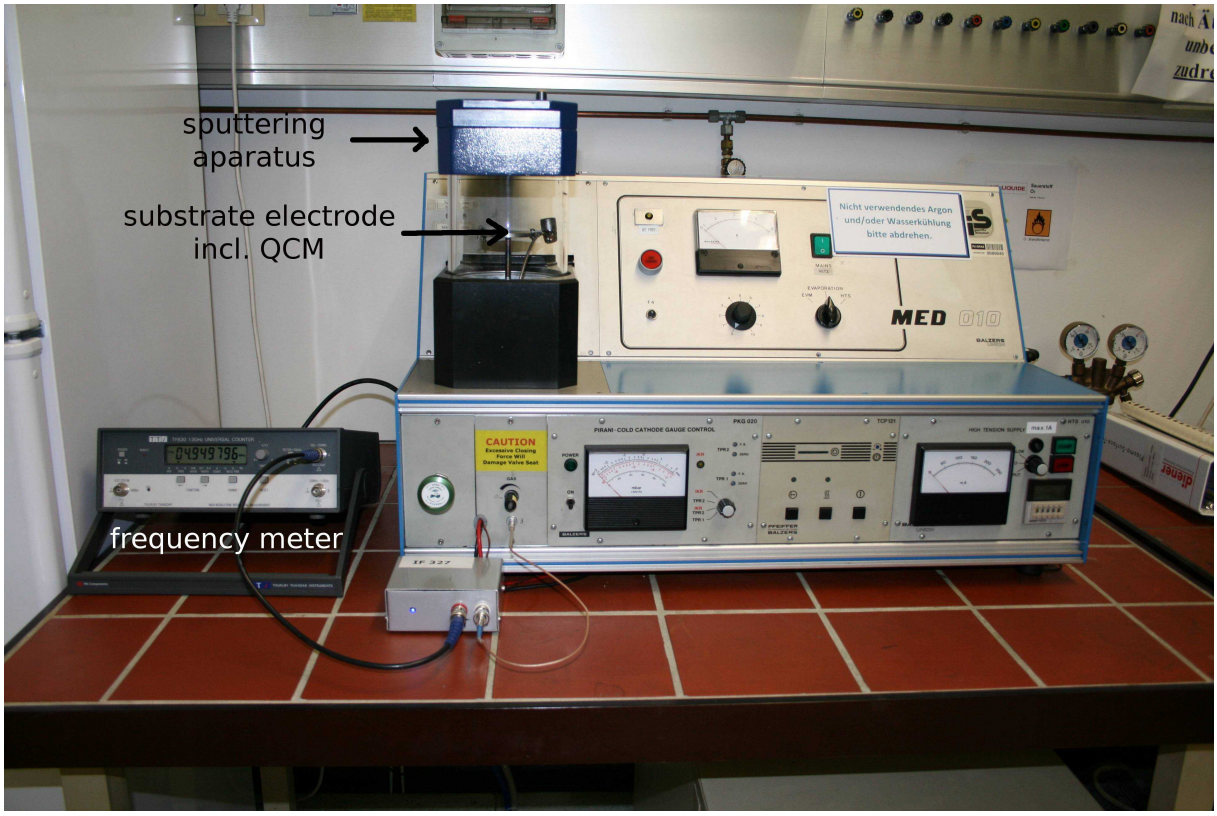

Figure 3.13: DC magnetron sputtering device of laboratory

After evacuating the working chamber of the DC magnetron sputtering device and subsequent flushing with an inert gas, e.g. argon, a glow discharge plasma is introduced by applying a high DC voltage between the two electrodes, one being the substrate holder the other one the target plate. The acceleration of positively charged inert gas ions towards the target plate induce the ejection of target atoms by momentum transfer. These mainly neutral target atoms proceed in the direction of the substrate. The presence of an additional magnetic field near the target plate (due to a magnet placed behind it that leads to a magnetic field perpenticular to the electric field near the target) enables a much higher plasma density and consequential a higher deposition rate. Furthermore the deposition can be performed at a lower pressure.

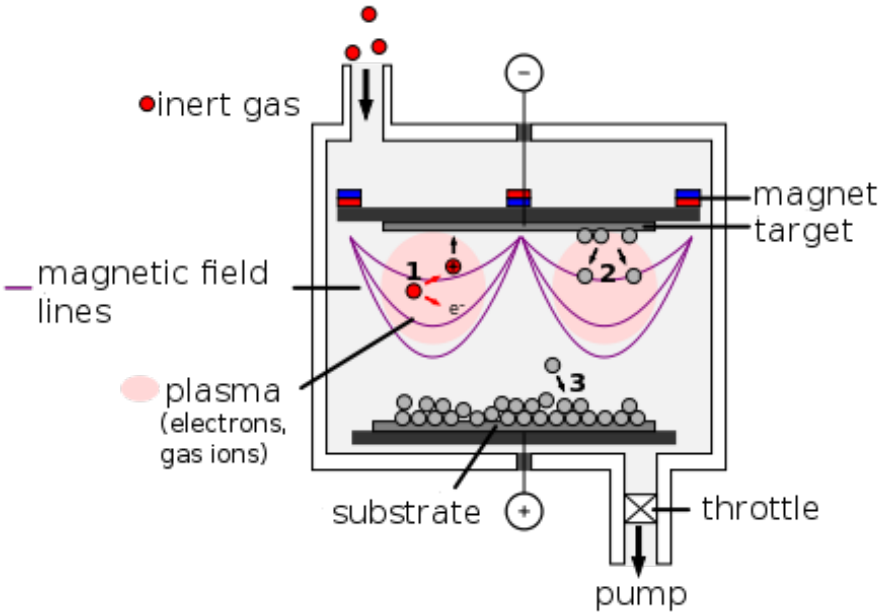

Figure 3.14: Schematic drawing[4] of DC magnetron sputtering:
1 glow discharge due to high electric field
2 ejection of target atoms by inert gas ions
3 deposition of target atoms at substrate

Following this procedure thin metal films with the DC magnetron sputtering device from the laboratory are fabricated:

1. place target
2. flush tube with argon (Ar)
3. put cleaned substrate in working chamber
4. evacuate (rotary vane pump and turbomolecular pump) until pressure $p_{\text{end}} = 10^{-5}\,\text{mbar}$ is reached (duration: $\approx 2\,\text{h}$)
5. reduce rotation speed of turbomolecular pump to $\frac{2}{3}$ of original value

[4]modified picture from de.wikipedia.org/wiki/Sputtern on January 19, 2010

6. note frequency of quartz crystal microbalance
7. pre-sputtering (closed target panel) to clean target for 1 min at 20 mA
8. open target panel and sputter at constant current of 20 mA
9. observe reduction of frequency
10. close target panel when desired frequency change is reached
11. ventilate working chamber

3.2.3.2 Sputter Deposition II

The deposition of AuPd is performed by the Institute for Electron Microscopy of the TU Graz using a GEA05 sputter device with these parameters:

working distance:	5 cm
voltage:	1.8 kV
discharge current:	5 mA
thickness monitoring:	quartz crystal microbalance

3.2.3.3 Thermal Evaporation

Another technique to obtain thin metal films on a substrate is thermal evaporation. For this purpose the high vacuum coating plant from the laboratory is used. This coating plant depicted in Fig. 3.15 enables to evaporate two different materials in one step of procedure. Due to the size of the cross vacuum chamber the large working distance between source and sample of about 20 cm leads to an approximately parallel vapor flux at the sample.

coating materials:	chromium (Cr) 99.99 %, gran. 0.7 - 3.5 mm from Balzers AG (Balzers, Liechtenstein)
	gold (Au) 99.999 % wire, 30 µm diameter from Ögussa GmbH (Wien, Austria)
thickness monitoring:	quartz crystal microbalance with frequency meter

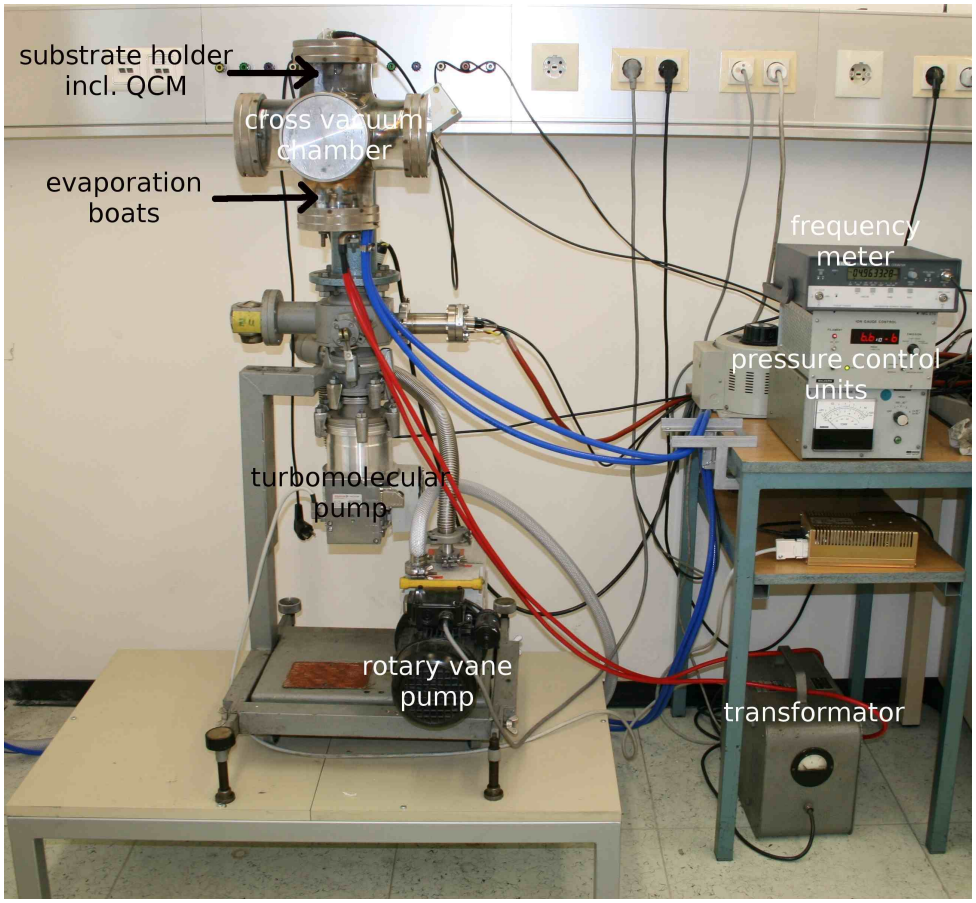

Figure 3.15: High vacuum coating plant of the laboratory

At the beginning the substrate as well as the coating materials deposited in the evaporation boats are placed inside a vacuum chamber. Once the required pressure (in the order of a few 10^{-6} mbar) is reached the evaporation boat is heated via a high current flow which is controlled by a transformer varying the voltage across the evaporation boat. This heating leads firstly to

a transformation from the solid into the liquid phase and subsequently to a transformation into the vapor phase. For a few materials like chromium a direct transformation from the solid into the vapor phase known as sublimation takes place.

As the vapor propagates it condensates everywhere inside the chamber due to its lower temperature and hence also at the substrate. A quartz crystal microbalance combined with a frequency meter and placed in the close vicinity of the substrate serves to monitor the thickness of the evaporated film.

Improving the adhesion of gold on a glass substrate a thin (2-3 nm) layer of chromium (Cr) is applied before the deposition of gold (Au). The thin metal films of Cr and Au are prepared following this procedure:

1. place cleaned substrate in vacuum chamber
2. evacuate (rotary vane pump and turbomolecular pump) until pressure of a few 10^{-6} mbar is reached (duration: ≈ 3 h)
3. start water cooling of evaporation boat mounting
4. note frequency of quartz crystal microbalance
5. heat evaporation boat with Cr inside until desired frequency change at microbalance is reached - output voltage of transformer: 70 V ($\rightarrow$ current ≈ 3 A)
6. heat evaporation boat with Au inside until desired frequency change at microbalance is reached - output voltage of transformer: 60 V ($\rightarrow$ current ≈ 3 A)
7. ventilate working chamber

3.2.4 Removal of the Size Reduced Spheres

Two different approaches to remove the size reduced spheres are applied: dissolving them in a solvent (for polystyrene one uses acetone or toluene) or withdrawal by using an adhesion tape and benefiting from the better adhesion of the metal to the substrate compared of that from the size reduced spheres to the substrate.

A combination of both leads to the best results: remove the reduced spheres with a Scotch® adhesion tape followed by sonication in toluene for 20 min.

4 Fabrication of Sphere Monolayers

The arrangement of monodispersed spheres in hexagonally close-packed monolayers of large areas (best in the cm^2-range) is crucial for the further fabrication process of metallic hole arrays and coated monolayers respectively - the larger the area the easier the handling as regards their characterization by optical transmission and conductivity measurements.

This chapter summarizes the learning steps of the applied deposition methods - drop casting and dip coating - in a chronological order to manage the arrangement of the spheres in hexagonally close-packed manner. The description of the fabrication steps of each method is organized in generations indicating different accesses and main improvements.

Microscope slides (cut edges, pre-cleaned, 76 × 26 mm, thickness: 1 mm) from Menzel GmbH & Co KG (Braunschweig, Germany) serve as substrate for the sphere deposition both by means of drop casting and dip coating.

Polystyrene (PS) microsphere suspensions are purchased from Thermo Fisher Scientific Inc. (Waltham, USA) owing the following properties:

- ▷ aqueous suspension packaged in 15 ml quantities
- ▷ 10 % solids by weight
- ▷ density of 1.05 g/cm^3
- ▷ mean diameter: 300 nm, 500 nm
- ▷ size uniformity (c.v.): $\leq 3\,\%$
- ▷ refractive index: 1.59 @ 589 nm (25°C)

For all cleaning processes (ultrasonication) and storing of the substrates as well as for the dilution procedures of the suspensions only ultrapure water is used fabricated by a Simplicity® 185 ultrapure water system from Millipore Corporation (Billerica, USA).

As regards the quality of the fabricated samples, the optical microscope serves as a first characterization tool to get information about the arrangement of the PS spheres whereas monolayer regions (close-packed or loosely packed), multilayer regions, islands on monolayer regions, point defects, slip dislocations etc. are already detectable. Furthermore one can distinguish the different monocrystalline domains of monolayer regions. The optical micrographs depicted in this chapter are all taken in reflectance.

Obtaining an even deeper insight into the different assemblies, investigations of selective samples are carried out by means of scanning electron microscopy.

4.1 Drop Casting

This section contains the fabrication steps of PS spheres deposition on a glass substrate using the drop casting method summarized in different generations (chronological order).

The microscope slides are cutted into 3 pieces of approximately 25 × 26 mm^2 in size. The deposition of the liquids (suspension, diluted suspension or water) is performed using a 100 µl pipette from Eppendorf AG (Hamburg, Germany).

Providing the necessary diluted suspension, 500 µl of ultra-pure water (0.2 µm filtered) is mixed with the appropriate amount of the original suspension in a sample bottle followed by 1 min of ultrasonication.

4.1.1 Generation 1

In this first generation both suspensions are used to get an insight into the PS sphere arrangement of different sphere diameters: 300 nm and 500 nm.

The fabrication steps in detail are:

- ▷ chemical treatment of substrate to render its surface hydrophilic
  1. mechanical cleaning with isopropanol
  2. drying with compressed air
  3. ultrasonication in isopropanol for 30 min
  4. drying with CO_2
  5. ultrasonication in ultra-pure water (0.45 µm filtered) for 30 min
  6. drying with CO_2
  7. immersion in chromosulfuric acid for 10 min
  8. cleaning with ultra-pure water
  9. drying with CO_2
- ▷ deposition of suspension in the laminar flowbox, the substrate is placed on top of an o-ring seal
  1. deposition of 100 µl ultra-pure water (0.2 µm filtered) across the substrate (homogeneous film)
  2. deposition of 5 µl and 2 µl respectively of the original suspension onto the water film
  3. dispersion of the suspension with the pipette and slightly rotation of the substrate to achieve a nearly even concentration of the suspension across the film
- ▷ evaporation of water in laminar flowbox, duration about 30 min

Figure 4.1 evinces two digital photographs of the PS spheres arrangement with different sphere diameters on a microscope slide after the evaporation of water. One can already identify regions of different colors originating of different sphere arrangements: close-packed or loosely packed, or rather monolayers, bilayers and multilayer regions.

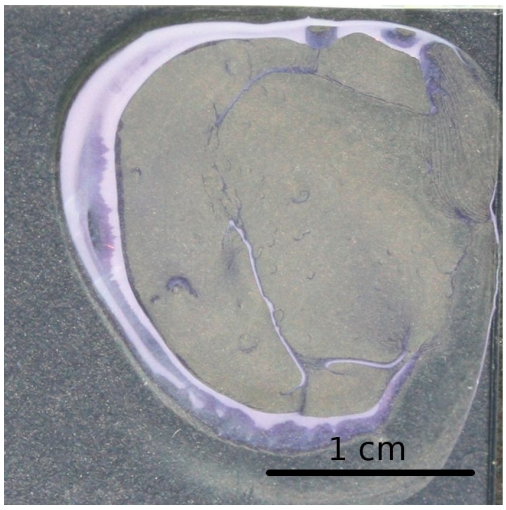

sphere diameter: 300 nm,
digital photo taken in reflectance

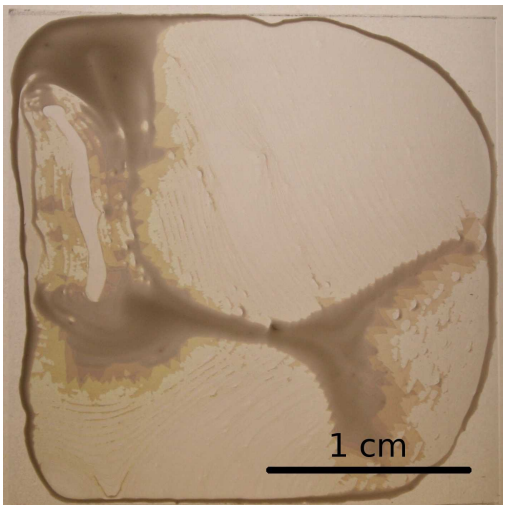

sphere diameter: 500 nm,
digital photo taken in transmission

Figure 4.1: Digital photographs of arranged PS spheres of different diameters on a glass substrate

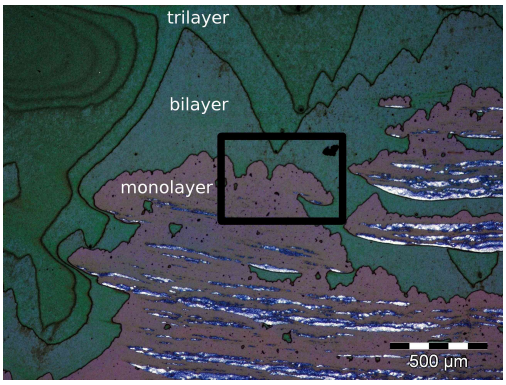

(a) magnification: 50 ×

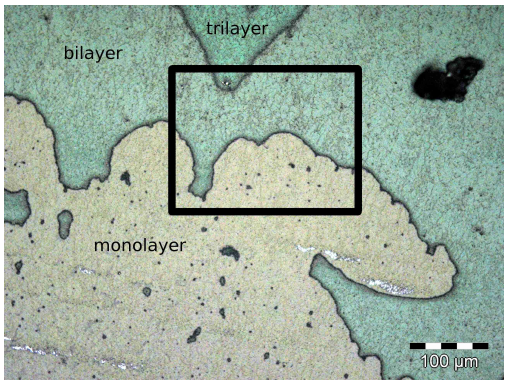

(b) magnification: 200 ×

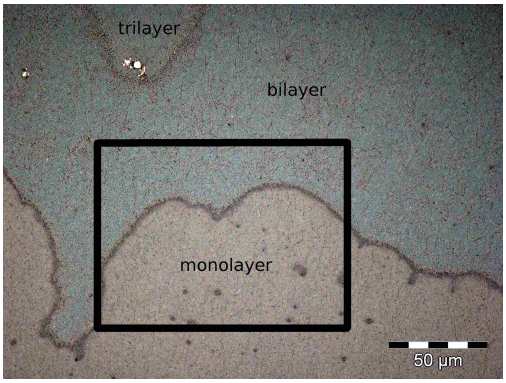

(c) magnification: 500 ×

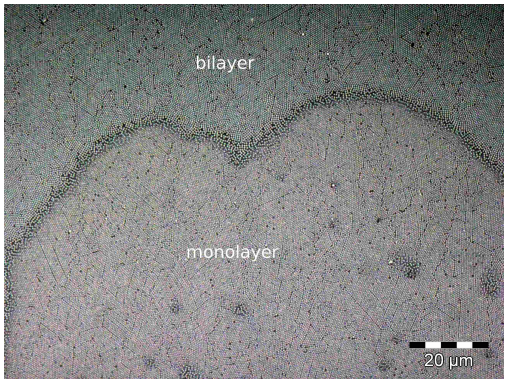

(d) magnification: 1000 ×

Figure 4.2: Optical micrographs of arranged 500-nm PS spheres coated with 18 nm AuPd - transition of multilayer to monolayer (lower part of particular photo).
The rectangle indicates the image section of the following micrograph.

Further investigation with the optical microscope provides a deeper insight into the variety of possible arrangements. Figure 4.2 of 500-nm PS spheres depicts a sequence of images of increasing magnification - from an overview picture to a detailed view detecting already single spheres. The multilayer formation leads to terraces onto monolayer regions. The different sphere arrangements yield a periodic modulation of the refractive index illustrated by their characterizing color impression.

Figures 4.3 and 4.4 show representative SEM images of monolayer and bilayer regions of PS spheres with diameters of 300 nm and 500 nm respectively. Monocrystalline domains of monolayer regions separated by grain boundaries cover at most an area of about 10×10 hexagonally closed-packed spheres. The largest multicrystalline monolayer region occupies an area of about $250 \times 1500\,\mu m^2$.

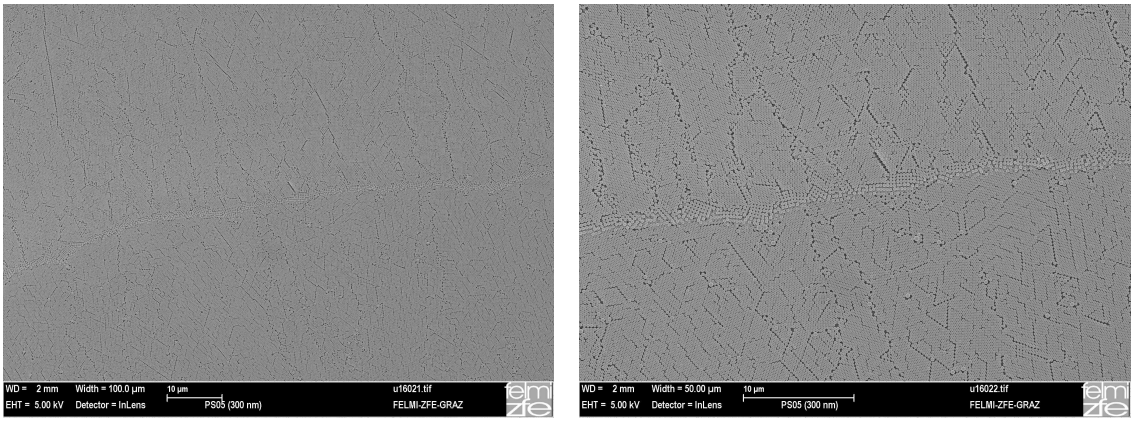

Figure 4.3: SEM images of the boundary between a bilayer (upper part of the particular image) and a monolayer (lower part) at different magnifications
PS sphere diameter: 300 nm

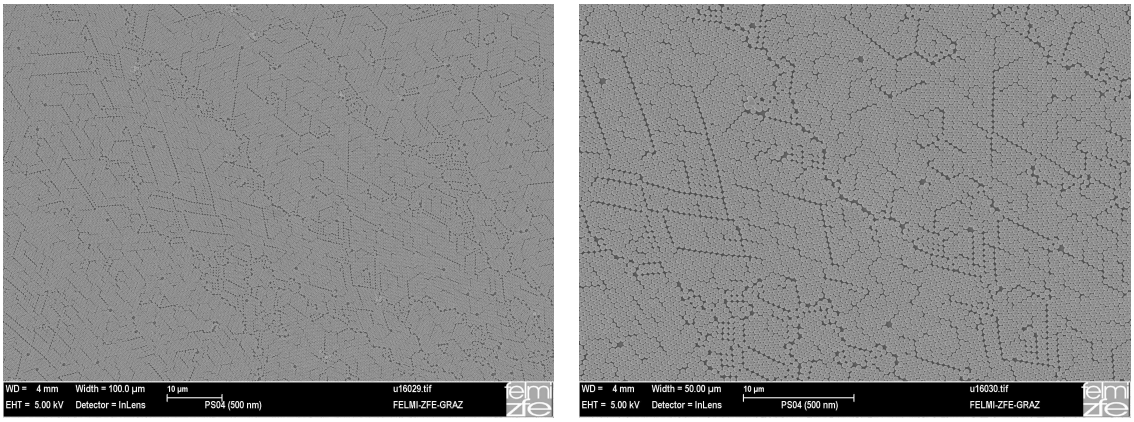

Figure 4.4: SEM images of a monolayer region of different magnifications
PS sphere diameter: 500 nm

The quality of the assembly in monolayers can be examined by means of a fast Fourier transformation (FFT) of the SEM image. Fig. 4.5 depicts on the one hand a representative SEM image of a monolayer region featuring arrangement defects like line defects and missing spheres and

on the other its FFT transformed counterpart indicating the sixfold symmetry of the triangular (hexagonal) lattice.

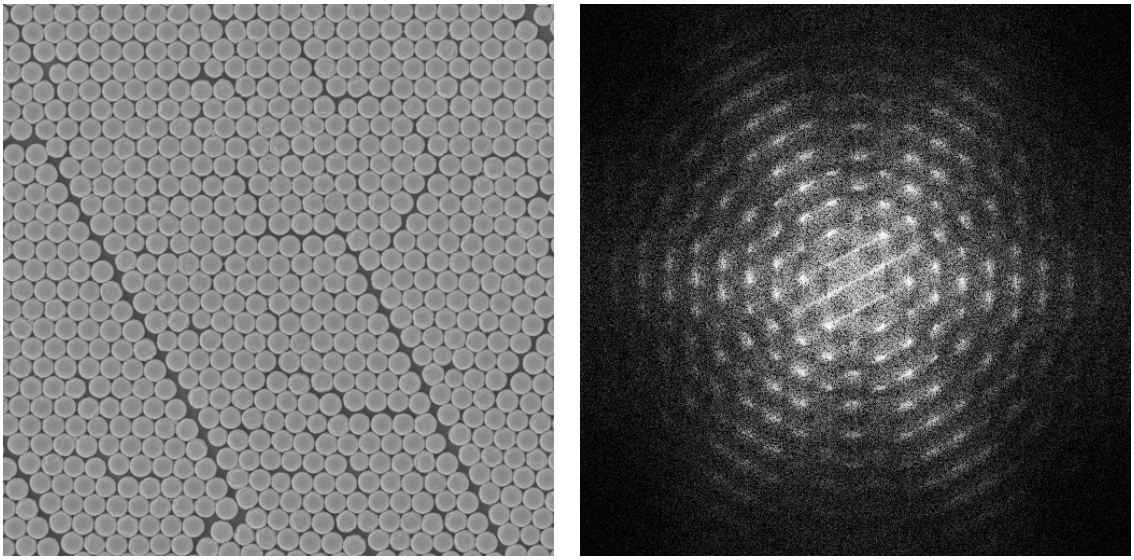

Typical assembly structure of a monolayer FFT transformed image

Figure 4.5: FFT analysis of a scanning electron micrograph from a monolayer region
PS sphere diameter: 500 nm
area size: 12.5 × 12.5 μm^2 (25 close-packed spheres in horizontal direction)

4.1.2 Generation 2

In generation 2 the main focus is to understand the influence of different substrate holders as well as of confining the environment of the substrate during the evaporation process to different volumes on the arrangement quality as regards the area of the monolayer regions and the area of monocrystalline domains. Furthermore the substrates are immersed in a chromosulfuric acid to improve the wettability of the suspension. In this generation only the PS suspension with sphere diameter of 500 nm is used.

As substrate holders serve:

- ▷ stiff optical sample holder
- ▷ converted loudspeaker: glass substrate ($50 \times 50\,mm^2$) fixed at diaphragm

The fabrication steps in details are:

- ▷ chemical treatment of substrate to render its surface hydrophilic
  1. mechanical cleaning with isopropanol
  2. drying with CO_2
  3. immersion in chromosulfuric acid for 10 min

4. cleaning with ultra-pure water
5. storage in ultra-pure water
6. ultrasonication in ultra-pure water for 10 min
7. ultrasonication in ultra-pure water (0.45 µm filtered) for 10 min
8. storage in ultra-pure water (0.45 µm filtered) until use

▷ deposition of suspension in laminar flowbox

1. leveling out of the respective substrate holder to achieve a horizontal substrate area
2. drying substrate with CO_2
3. deposition of suspension
   a) distribution of 100 µl of diluted suspension (ratios: 1:10, 1:17, 1:20, 1:25, 1:50) homogeneously across substrate
   b) distribution of 100 µl of ultra-pure water (0.2 µm filtered) homogeneous across substrate and consequent deposition a drop of the suspension (amount: 2 or 4 µl) onto the water film

▷ evaporation of water

a) uncovered
b) enclosed in a small plastic box
c) covered with a glass cylinder (diameter: 15 cm)

Oscillations originating from the laboratory environment (i.e. pump of flowbox) couple into the substrate holders and influence the arrangement process of the PS spheres. Hence an oscillator system (loudspeaker and optical substrate holder including an oscillator) with the possibility to adjust the frequency is chosen as substrate holder.

Improvements of this fabrication routine compared to the first one:

- ▷ reduced contact time of the substrates with air, especially after the immersion in chromo-sulfuric acid
- ▷ a more defined evaporation process: smaller volume, no external air flow
- ▷ loudspeaker as substrate holder is an oscillating system, maybe better distribution of PS spheres across substrate
- ▷ loudspeaker enables to couple user-defined frequencies

From experiments with specified external frequencies (100 Hz, 2 kHz, 4 kHz, 6 kHz, 8 kHz) arises that the coupling of the substrate to an oscillating system doesn't show any significant influence on the sphere arrangement. The best results with respect to reproducibility are obtained with the converted loudspeaker as substrate holder enclosed in the small plastic box. The pump of the flowbox is switched off during the evaporation process. Summing up, larger monolayer areas are obtained the lower the vibrations during the evaporation process both due to user-defined frequencies as well as due to vibrations caused by the laboratory environment.

An overview digital photo of a whole sample is depicted in Fig. 4.6 including 2 optical micrographs which display enlarged the drawn black rectangles. A close-packed monolayer of 500-nm PS spheres exhibits a yellow color due to its two-dimensional periodic modulation of the re-

fractive index, a close-packed bilayer of the same spheres shows a purple color induced by its three-dimensional periodicity. Compared to the sizes of the monolayer areas of generation 1 (details in Fig. 4.2) a significant enlargement can be stated: the largest multicrystalline monolayer occupy an area of about $2\,\mathrm{mm}^2$.

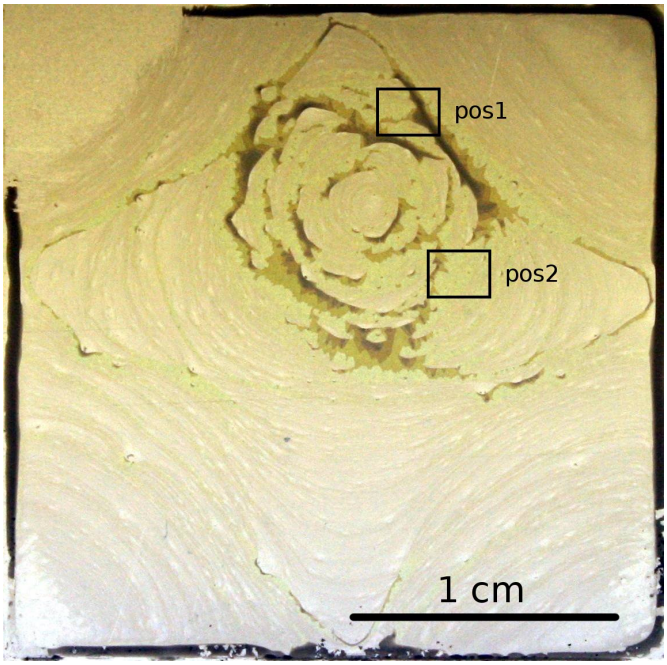

overview image

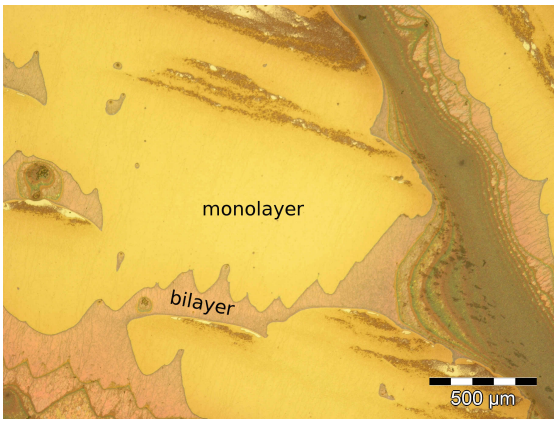

pos1

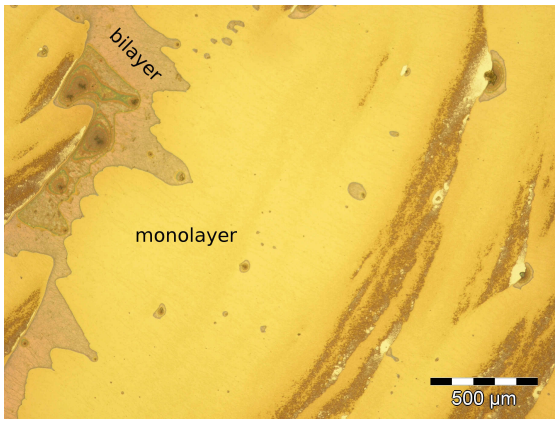

pos2

Figure 4.6: Images of generation 2: an digital overview picture taken in transmission and the respective optical micrographs recorded at 2 different positions

SEM images of samples fabricated according to this generation demonstrate a sphere arrangement like depicted in Fig. 4.7. An analysis by means of FFT is performed, the results are shown in Fig. 4.8 evincing the sixfold symmetry of the triangular (hexagonal) lattice. The quality of the monocrystalline domains which have an average of approximately $25 \times 25\,\mu\mathrm{m}^2$ in area is influenced by the size dispersion of the spheres (c.v. $= 3\,\%$, indicated by the supplier).

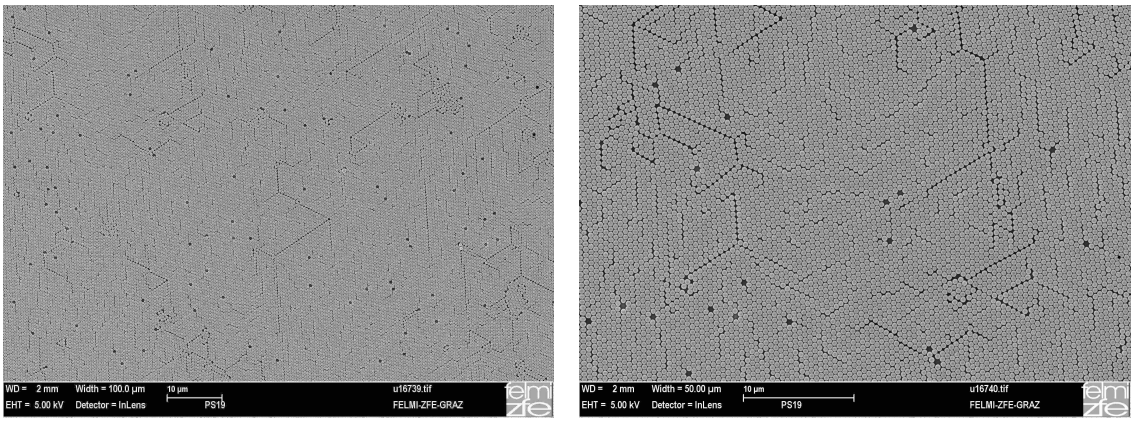

Figure 4.7: SEM images of a monolayer region of different magnifications
PS sphere diameter: 500 nm

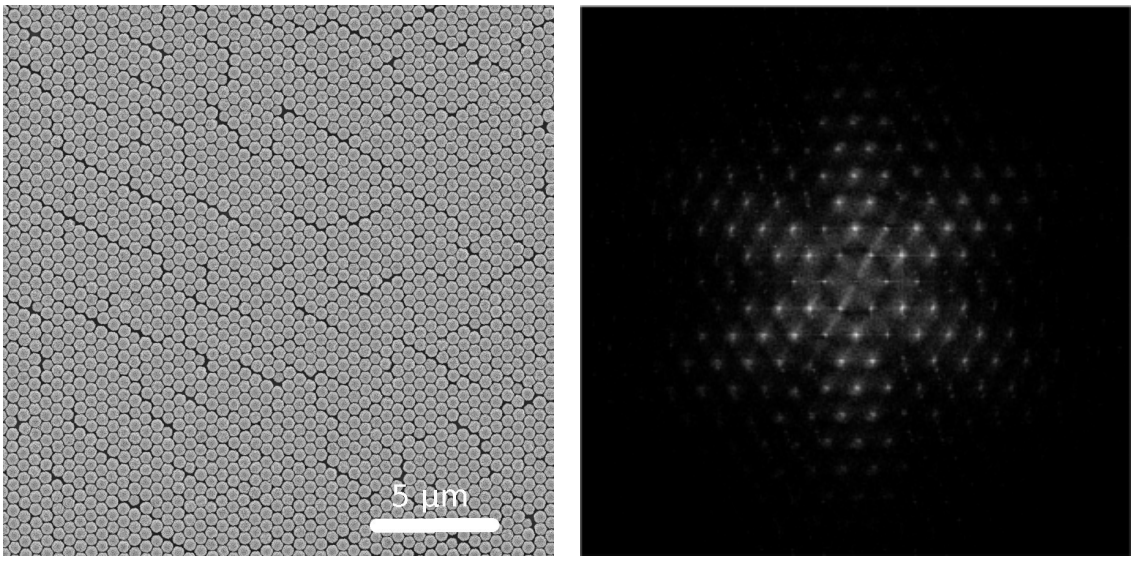

Typical assembly structure of a monolayer FFT transformed image

Figure 4.8: FFT analysis of a scanning electron micrograph from a monolayer region
PS sphere diameter: 500 nm)

4.1.3 Generation 3

The main conclusions of the results of generation 2: the less vibrations the larger the monolayer areas and diluting the suspension before deposition leads to larger monolayer areas. Thus a stiff optical sample holder is placed on an approximately vibration-free table. Hereupon the substrate is positioned horizontally on an o-ring seal.

Although the immersion of the microscope slides introduced in the previous generation yields a significant improved wettability of the suspension, a complete wetting of the substrate could not be achieved. After spreading the suspension across the substrate little support with the pipette is needed. It seems that the contact between the tweezer and chromosulfuric acid during the lift-out of the substrates has an influence on the wettability. Thus the chromosulfuric acid is exhausted before the microscope slides are cleaned with ultra-pure water.

Within this generation only the 500-nm PS suspension is used.

The fabrication steps in detail:

- ▷ chemical treatment of substrate to render its surface hydrophilic
  1. mechanical cleaning with isopropanol
  2. drying with CO_2
  3. immersion in chromosulfuric acid for 10 min
  4. exhausting chromosulfuric acid
  5. cleaning with ultra-pure water
  6. storage in ultra-pure water
  7. ultrasonication in ultra-pure water for 10 min
  8. ultrasonication in ultra-pure water (0.45 µm filtered) for 10 min
  9. storage in ultra-pure water (0.45 µm filtered) until use
- ▷ deposition of suspension
  1. level out substrate holder to achieve a horizontal substrate surface
  2. drying substrate with CO_2
  3. deposition of 100 µl diluted suspension (ratio: 1:10) homogeneously across substrate
- ▷ evaporation of water in a small plastic box (volume $\approx$ 2.5 liter) enclosing the whole setup (substrate holder and substrate)

Fig. 4.9 evinces a digital overview photograph of the whole sample including 2 optical micrographs of selected positions indicated by the black rectangles. The different colors of the digital photo taken in transmission are due to the periodical arrangement of the PS spheres: monolayers - light-yellow, bilayers - yellow. This color impression changes at the optical micrographs because of the observation in reflectance: monolayers - yellow, bilayers - purple.

Within this generation the dimensions of the multicrystalline monolayer regions could be further enlarged compared to the previous one (depicted at Fig. 4.6). The size of some regions exceeds 10 mm^2.

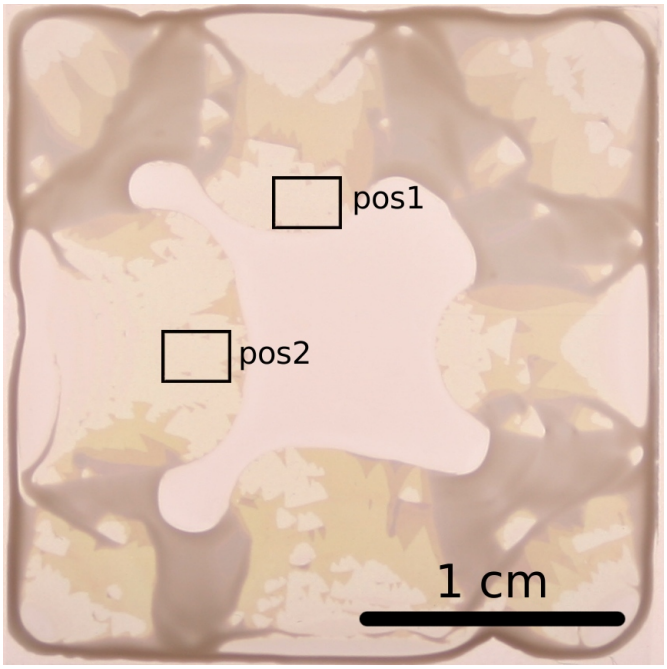

overview image

pos1

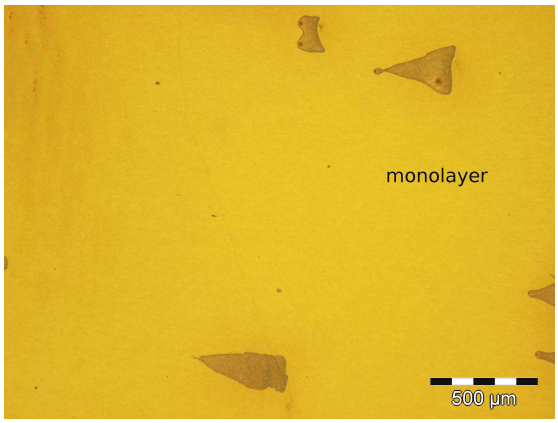

pos2

Figure 4.9: Images of generation 3: an digital overview picture taken in transmission and the respective optical micrographs recorded at 2 different positions

As the samples of this generation serve as template for hole arrays the size of the spheres is reduced by means of the reactive ion etching procedure. Characteristical SEM micrographs are depicted at Fig. 4.10 exhibiting an approximately similar PS sphere arrangement as in the previous generation (Fig. 4.7). One can conclude, that the size of a monocrystalline domain keeps fairly constant compared to generation 2. The characteristics of this generation seem to be more missing spheres in a monocrystalline domain.

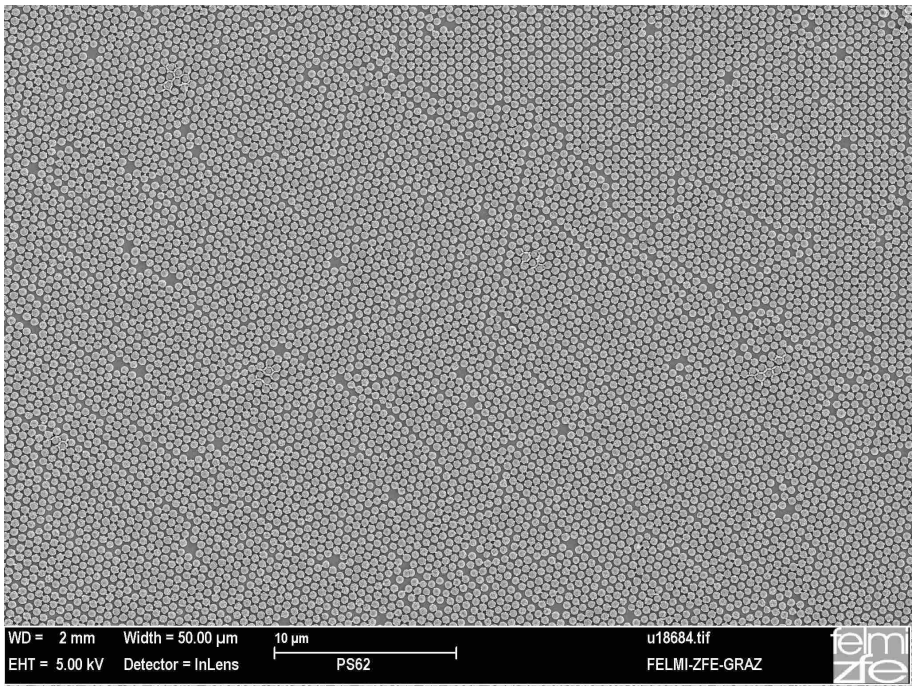

mean PS sphere diameter: $408 \pm 13\,\mathrm{nm}$

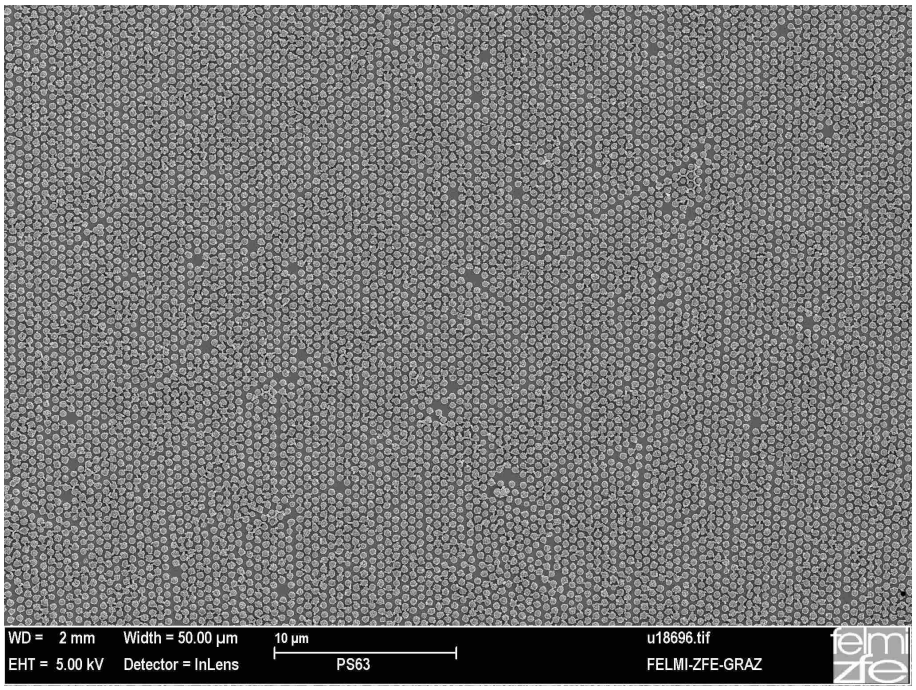

mean PS sphere diameter: $365 \pm 10\,\mathrm{nm}$

Figure 4.10: SEM micrograph of a monolayer region of generation 3
The reduced PS sphere diameter originates from the reactive ion etching

4.1.4 Generation 4

Motivated by the dip coating procedure, tilting of the substrate by a small angle (between 1 - 3 °) leads to a more defined and continuous evaporation line (contact line of liquid suspension, glass substrate and air). Within the previously mentioned generations one cannot control the evaporation directly, it starts somewhere at the substrate where the liquid layer approaches the sphere diameters. In the case of a vibration-free environment the evaporation begins at the corners and proceeds towards the center. Schematic drawings of the evaporation process depicts Fig. 4.11. This evaporation process can be identified in the final PS sphere arrangements too, e.g. as illustrated at the digital photos at Fig. 4.6 and Fig. 4.9.

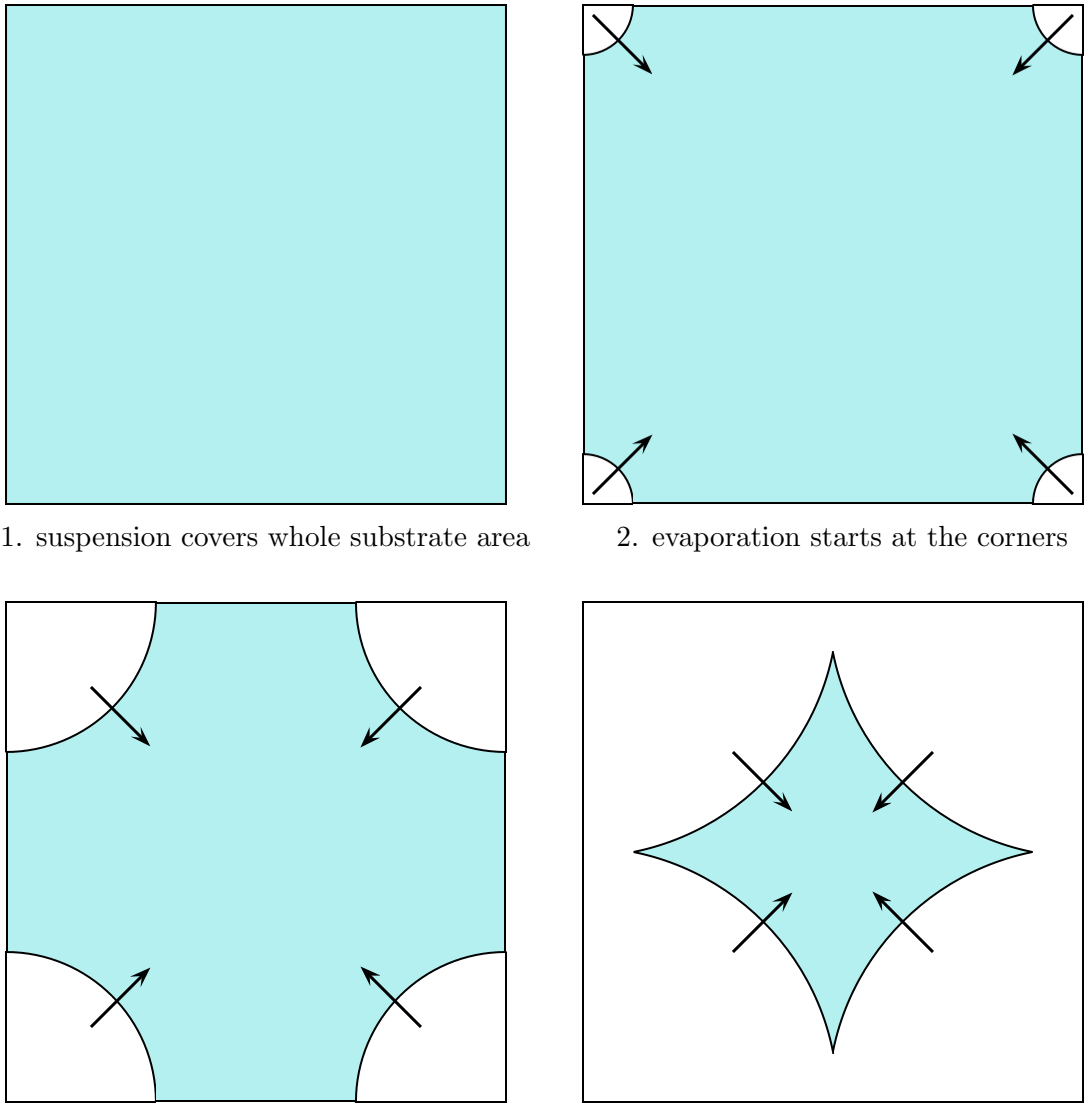

1. suspension covers whole substrate area
2. evaporation starts at the corners
3. evaporation continues towards center
4. evaporation at the center

Figure 4.11: Evaporation process of a liquid suspension spread across a horizontal glass substrate in the case of a vibration-free environment, the evaporation starts at the corners and proceeds towards the center

Within this generation only the 500-nm PS suspension is used.

The fabrication steps in detail:

- ▷ chemical treatment of substrate to render its surface hydrophilic
  1. mechanical cleaning with isopropanol
  2. drying with CO_2
  3. immersion in chromosulfuric acid for 10 min
  4. exhausting chromosulfuric acid
  5. cleaning with ultra-pure water
  6. storage in ultra-pure water
  7. ultrasonication in ultra-pure water for 10 min
  8. ultrasonication in ultra-pure water (0.45 µm filtered) for 10 min
  9. storage in ultra-pure water (0.45 µm filtered) until use
- ▷ deposition of suspension
  1. level out substrate holder to achieve a horizontal substrate surface
  2. drying substrate with CO_2
  3. deposition of 100 µl diluted suspension (ratios: 1:19, 1:20, 1:21) homogeneously across substrate
  4. tilting sample by a small angle (1-3 °)
- ▷ evaporation of water in a small plastic box (volume $\approx$ 2.5 liter) enclosing the whole setup (substrate holder and substrate)

The optical micrographs (Fig. 4.12) of a representative monolayer region demonstrate the quality of the fabricated monolayers as regards area size and monocrystalline domain size. The upper image exhibits two different colors originating from differently orientated domains.

The tilted drop casting method enables to produce monolayer regions of more than 5×5 mm^2 in size. The monocrystalline domains clearly identifiable at the SEM micrographs but by means of optical microscopy too, cover an area of approximately 40×40 µm^2 only disturbed by the size dispersion of the spheres as can be obviously seen in SEM micrograph at Fig. 4.13. This change in diameter of one PS sphere leads to a misfit in its immediate vicinity.

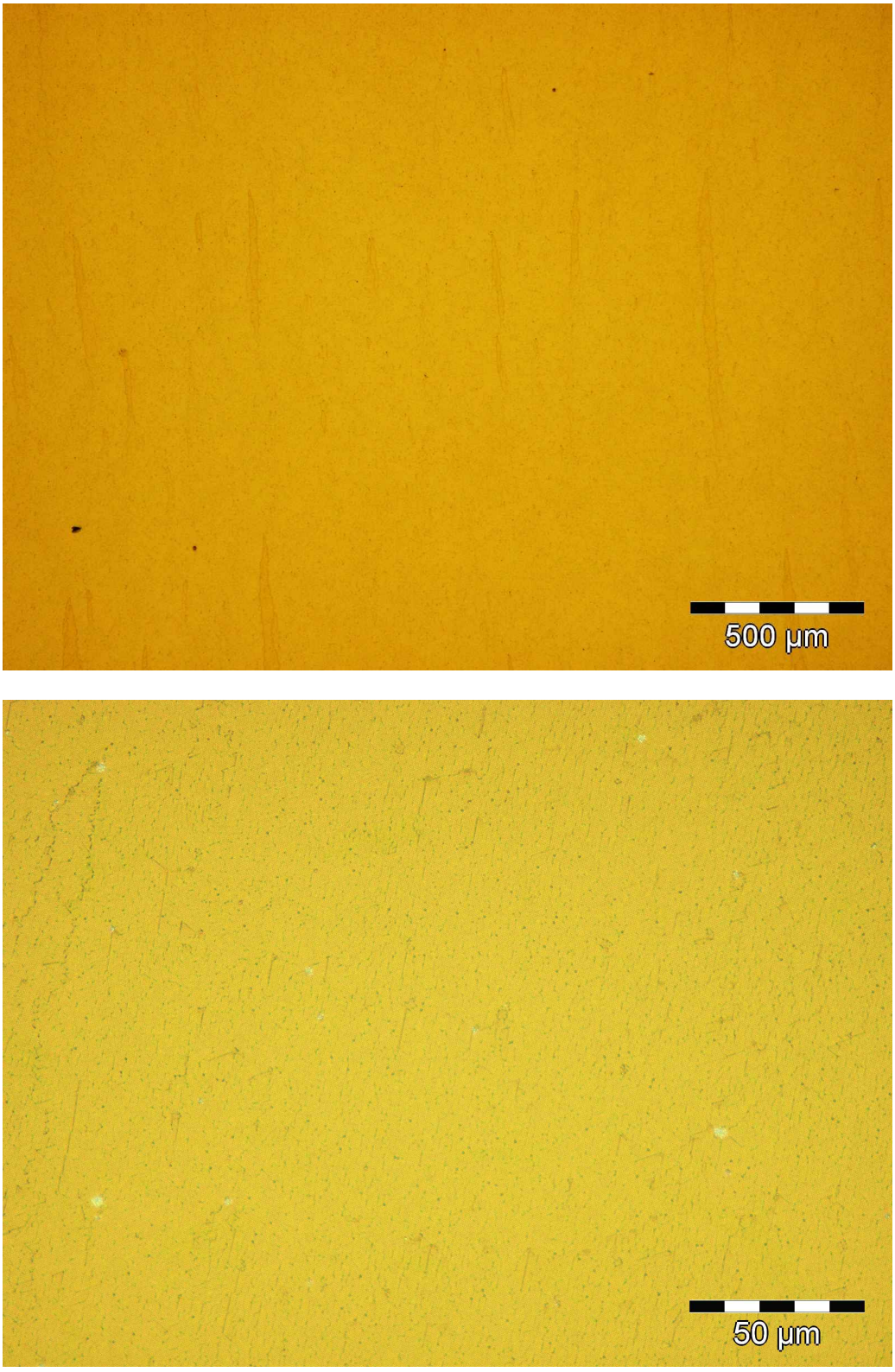

Figure 4.12: Optical micrographs at 2 different magnifications of a monolayer region of close-packed PS spheres arranged according to generation 4
PS sphere diameter: 500 nm

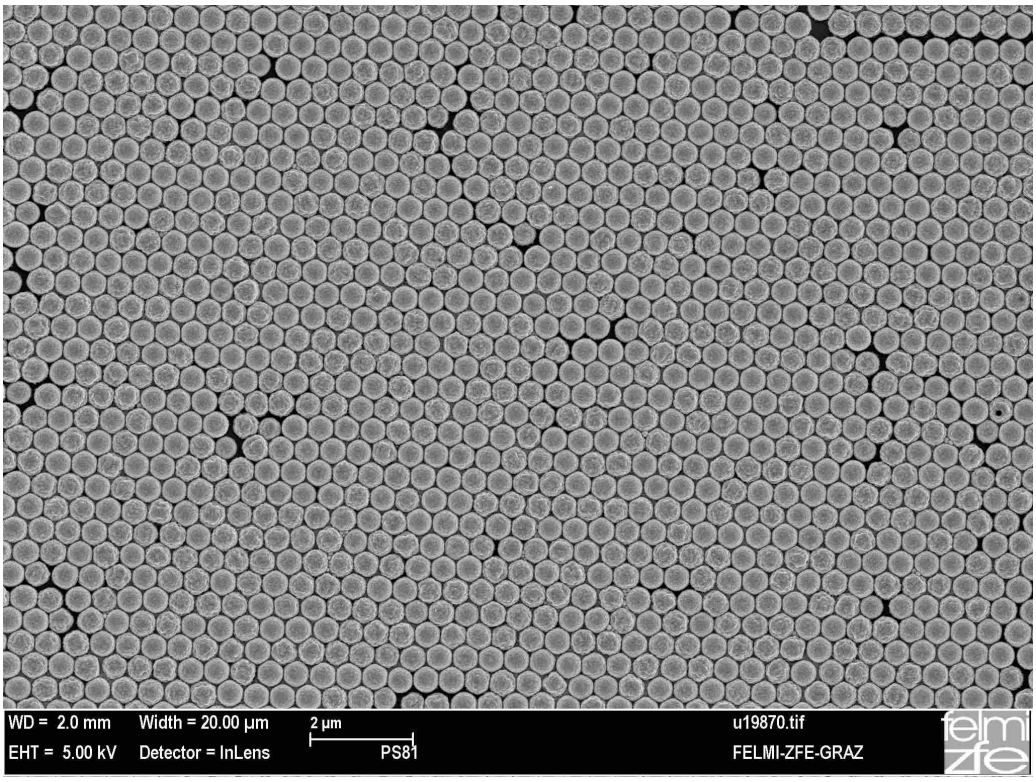

Figure 4.13: SEM micrograph of a monolayer region of generation 4
PS sphere diameter: 500 nm

4.2 Dip Coating

This section describes the experimental details to fabricate large PS monolayer areas by means of dip coating. As substrate serves a microscope slide cutted into a piece of approximately $50 \times 26\,\mathrm{mm}^2$ in size. Within this fabrication method only the 500-nm PS suspension is used.

Larger amounts ($\approx 15\,\mathrm{ml}$) of differently diluted suspensions (ratios - 1:10, 1:15 and 1:20) are prepared once and utilized for several withdrawing experiments. Stored in glass sample bottles, they are ultrasonicated for 10 s before decanting in the glass cuvette with a 20-ml single-use syringe.

The fabrication steps in detail:

- ▷ chemical treatment of substrate to render its surface hydrophilic
  1. mechanical cleaning with isopropanol
  2. drying with CO_2
  3. immersion in chromosulfuric acid for 10 min
  4. exhausting chromosulfuric acid
  5. cleaning with ultra-pure water
  6. storage in ultra-pure water
  7. ultrasonication in ultra-pure water for 10 min
  8. ultrasonication in ultra-pure water (0.45 µm filtered) for 10 min
  9. storage in ultra-pure water (0.45 µm filtered) until use
- ▷ deposition of 10 ml diluted suspension (ratios - 1:10, 1:15, 1:20) in a 12 ml glass cuvette
- ▷ drying of substrate with CO_2
- ▷ mounting substrate vertically at the substrate holder
- ▷ dipping the substrate into the filled glass cuvette at the desired starting point by means of the control unit
- ▷ (optional) placing of 2 plastic boxes each filled with 50 ml distilled water and a tissue enlarging the effective water-air contact surface to increase the humidity during the withdrawing process
- ▷ positioning of the temperature and humidity measurement unit on top of the tower
- ▷ covering whole setup with the perspex box
- ▷ withdrawing the substrate at constant speed (200 nm/s, 400 nm/s, 500 nm/s, 1000 nm/s)

Producing monolayer regions of large area sizes by means of dip coating is strongly influenced by different parameters: dilution of the suspension, withdrawing speed, humidity and temperature. The difficulty is that one ensures to keep all these parameters constant at a certain value throughout the withdrawing procedure which takes depending on the withdrawing speed between 42 h and 8 h for an effective stroke of 30 mm. Assuming that the withdrawing speed and the temperature remain constant, the dilution of the suspension and the humidity may change dramatically.

Regarding the dilution of the suspension, i.e. the concentration of spheres, a significant change can occur during the fabrication process due to

- sinking of the spheres which isn't anymore negligible for long-term withdrawing procedures,
- evaporation of the liquid part of the suspension during the dip coating process and
- deposition of spheres at the substrate especially by unindented large scale multilayer formations.

Maintaining a constant concentration of spheres in the suspension, represents the key for success in fabricating large area monolayers in a reproducible manner beside the control of the humidity.

The dip coating setup (Fig. 3.9) in its current configuration doesn't enable to manage the humidity at a defined, constant (high) level both

- to slow down the evaporation process and consequently keeping the concentration of the spheres in the suspension constant and
- to prevent the aggregation of spheres on the suspension surface.

Placing filled plastic boxes including a tissue to enlarge the effective water-air contact surface inside the perspex box yields to a significant increase of the humidity to about 70 - 90 % and preserves approximately constant during the withdrawing procedure but a clearly defined, adjustable humidity can not be achieved.

The optical micrographs (Fig. 4.14) already indicate the achievable dimensions of the monolayers by means of dip coating. Various samples produced by this fabrication technique cover a multicrystalline area in the range of cm^2. The multicrystalline structure can be identified on a closer inspection in the different colors in the upper image of this figure. The size of monocrystalline monolayers is comparable to generation 3 and 4 of the drop casting method but disturbed due to missing spheres and due to variations of the sphere diameters. Fig. 4.15 evinces two characteristical SEM micrographs, the spheres have already been reduced by means of reactive ion etching, furthermore parts of the size reduced spheres have been removed.

Summing up, the dip coating procedure has a high potential regarding the fabrication of large monolayers of close-packed PS spheres. The reproducibility of fabricated structures is influenced by the change of sphere concentration and the difficult control of the humidity as previously discussed. At the moment dip coating procedures at equal conditions with the exception of the humidity result in different PS sphere arrangements: close-packed monolayers or close-packed monolayers with stripes of bilayers, and close-packed monolayes or islands of close-packed monolayers.

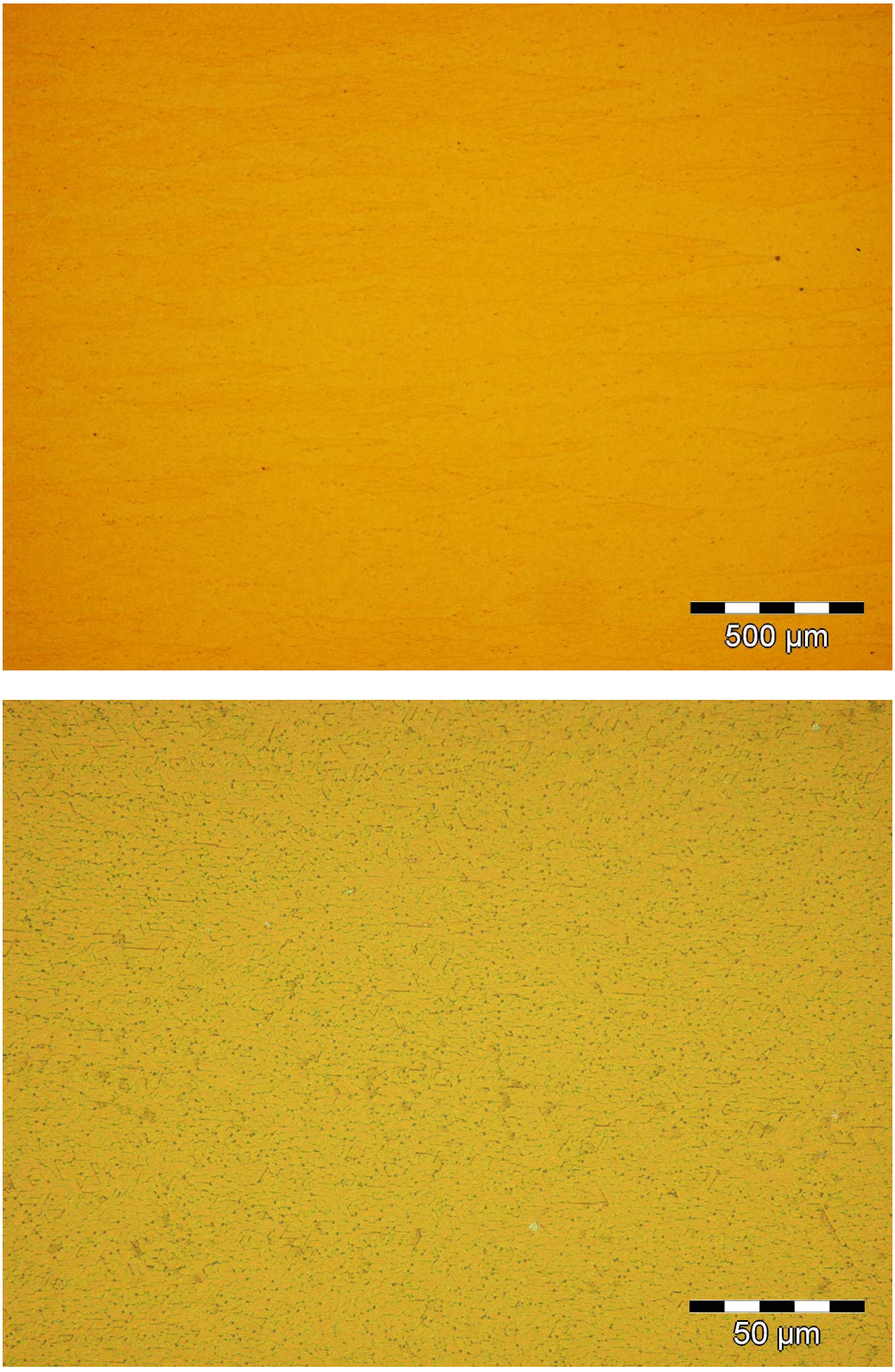

Figure 4.14: Optical micrographs at 2 different magnifications of a monolayer regions of close-packed PS spheres arranged according to the dip coating procedure
PS sphere diameter: 500 nm

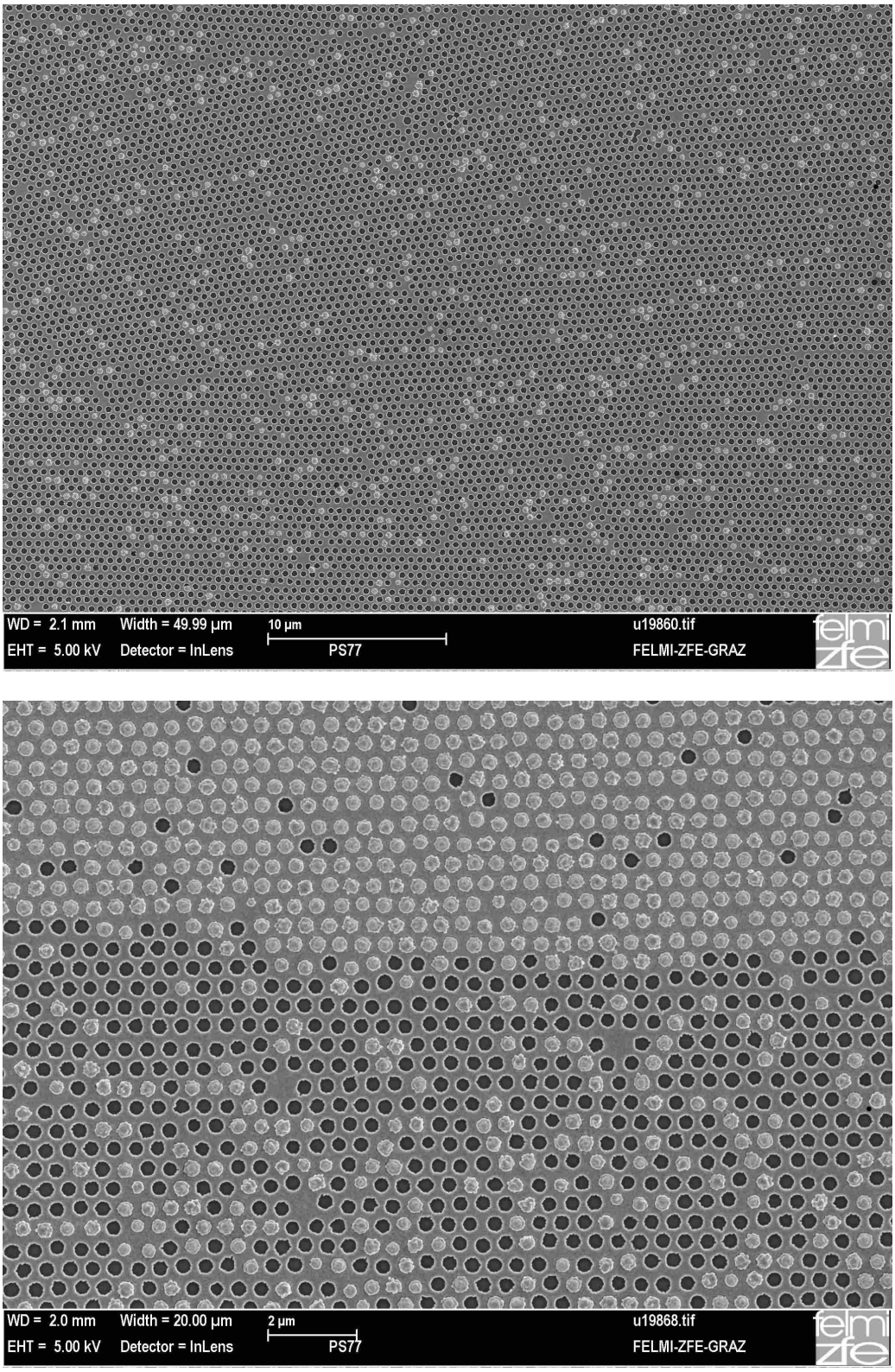

Figure 4.15: SEM micrographs at 2 different magnifications of a monolayer regions fabricated by means of dip coating
White points ... size reduced spheres, black points ... holes
PS sphere diameter: 500 nm

5 Fabrication of Metallic Hole Arrays

Subsequent to the fabrication of hexagonally close-packed PS spheres in monolayers of appropriate area size ($> 5 \times 5\,\mathrm{mm}^2$) by means of drop casting or dip coating, the reactive ion etching step whose details are described in section 3.2.2 is followed to reduce the diameters of the PS spheres while keeping the periodicity constant. The size reduced structure serves as template for the coating procedures performed by means of sputter deposition and thermal evaporation. The metallic hole array is achieved by a lift-off process of the size reduced spheres.

This chapter starts with the thickness calibration of unstructured metal layers, followed by a short treatment of the layer homogeneity on different substrates and finally deals with the removal of the size reduced spheres and the hole diameters of the patterned metal layers.

5.1 Calibration of Film Thickness

During the coating procedures (sputtering and thermal evaporation) a frequency meter monitors the change in frequency of the quartz crystal microbalance that is mounted on a level with the substrate. Hence the thickness t of the deposited film corresponds to a frequency shift Δf. The relation between them is established from thickness measurements at the profilometer and by means of x-ray reflectivity. Once the frequency shift is linked to a film thickness one can fabricate further films with a defined thickness by observing the change in frequency of the quartz crystal microbalance.

5.1.1 Sputter Deposition

As already mentioned in the experimental section palladium (Pd) and platinum (Pt) are deposited using the DC magnetron sputter device from the laboratory. Prior to the sputter deposition two cutted microscope slides of different size from Menzel GmbH & Co KG, Braunschweig (Germany) - identical to the substrates used for the sphere arrangements - are mounted laterally displaced on a Si(111) wafer[1]. This setup, evinced on Fig. 5.1, produces the necessary step profile at the Si(111) wafer for the thickness measurements at the profilometer and enables transmission measurements at the coated glass substrate too.

The first measurements at the profilometer were not satisfying because the step profile extends a large transition area of about 2 mm in direction perpenticular to the step originating from the screening of the microscope slide covering during the sputter process. Therefore the necessary

[1] supplier: Silchem Handelsgesellschaft mbh (Freiberg, Germany), orientation: (111) 4° off, thickness: 525 µm

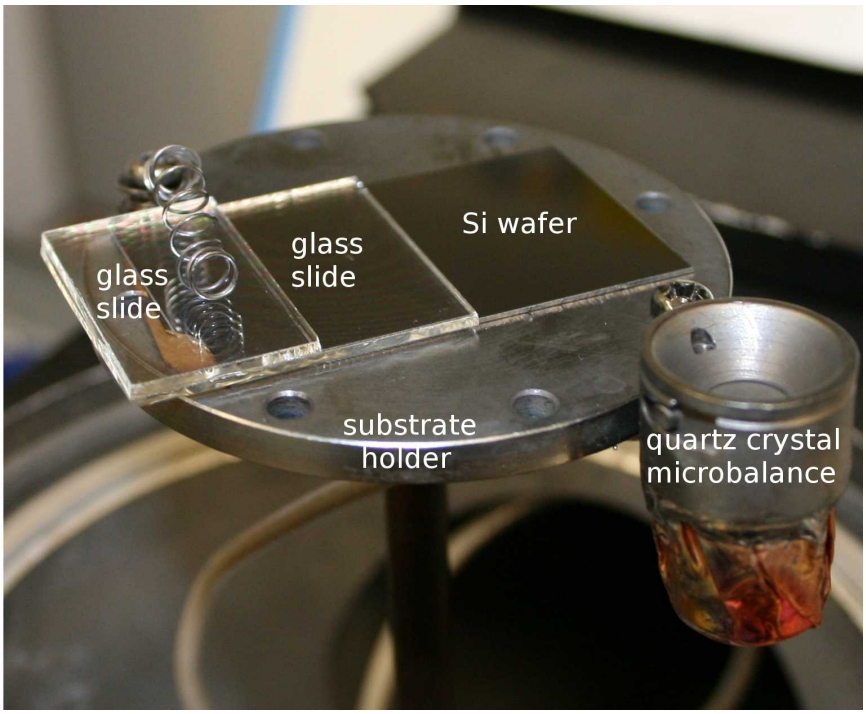

Figure 5.1: Substrate holder of the DC magnetron sputter device including the setup for thickness and transmission measurements

step profile is generated by a linear scratch with a pure organic and flat platelet ranging from the center of the substrate to the edge as shown in Fig. 5.2.

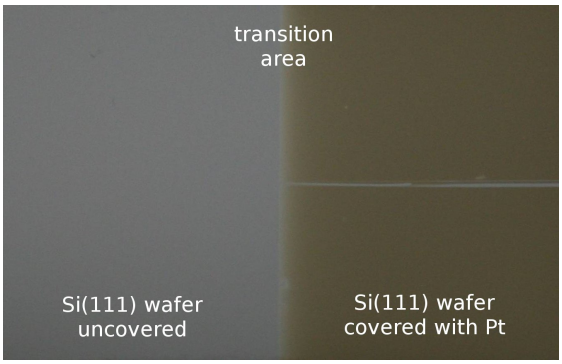

Figure 5.2: Si(111) wafer half covered with Pt, the horizontal scratch serves for the profilometer measurements

The results from the thickness measurements of palladium films as well as the transmission measurements with the spectrophotometer are summarized in Tab. 5.1.

A graphical plot (Fig. 5.3) shows the data of the thickness measurements including the uncertainties. The relation between the mean film thickness t and the frequency shift Δf is achieved by a Least-Square-Approximation [34] and yields a best-fit line

$$t[\mathrm{nm}] = (108.2 \pm 2.1)\,\Delta f[\mathrm{kHz}] \tag{5.1}$$

Table 5.1: Thickness and transmission measurements of **palladium** sputtered films

wd	working distance
st	sputter time
Δf	frequency change
T	relative transmission through substrate and film
t	measured mean film thickness

sample	pd3	pd5	pd6	pd7	pd8	pd9
substrate	glass	Si wafer	glass	Si wafer	Si wafer	Si wafer
wd [cm]	8	8	8	8	11	8
st [min]	3	5	9	20	12	10
Δf [Hz]	168	285	500	1060	198	703
T [%] @ 450 nm	38.7	21.2	9.8	1.6	35.1	6.6
T [%] @ 550 nm	41.6	24.6	12.8	3.4	39.1	10.8
t_{profil} [nm]	20 ± 5	33 ± 3	69 ± 4	118 ± 4	29 ± 3	67 ± 4
$t_{\text{x-ray}}$ [nm]					22 ± 1	65 ± 3

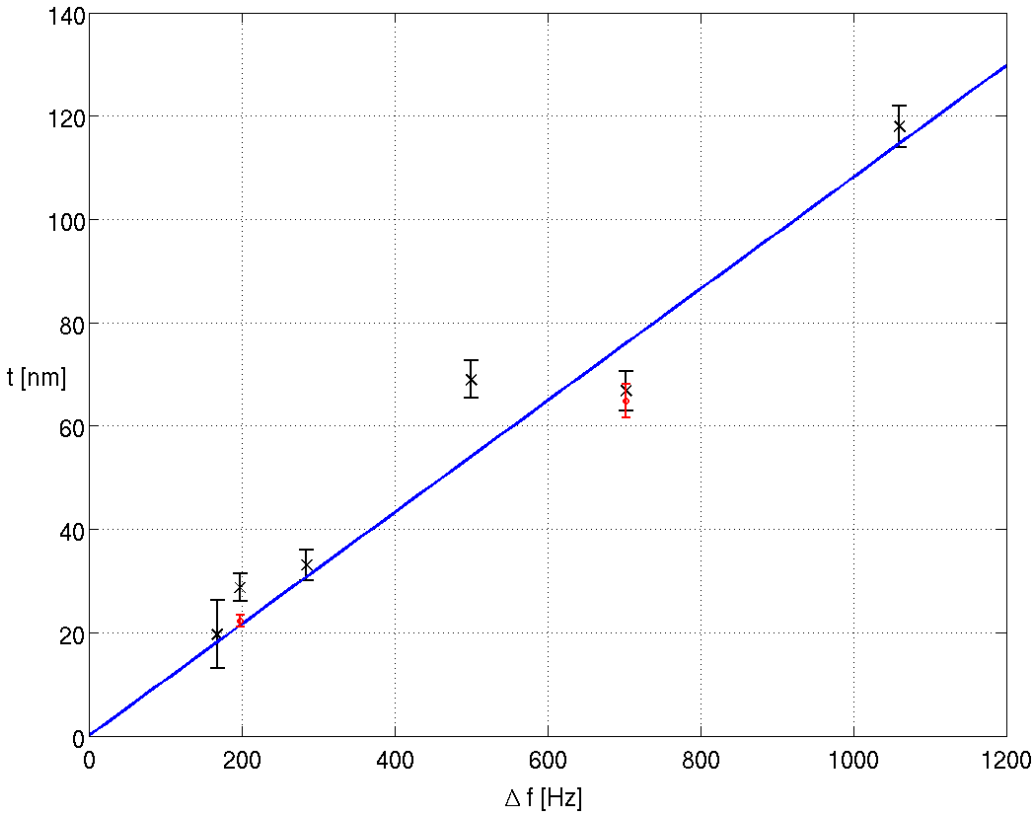

Figure 5.3: Thickness t of palladium thin films related to the frequency shift Δf including the best-fit line (Eq. 5.1)
x (black) ... measurements at the profilometer
o (red) ... measurements with x-ray reflectivity

The results from the thickness measurements of platinum films as well as the transmission measurements with the spectrophotometer are summarized in Tab. 5.2.

Table 5.2: Thicknesses of **platinum** sputtered films
wd working distance
st sputter time
Δf frequency change
T relative transmission through substrate and film
t measured mean film thickness

sample	pt10	pt11	pt12	pt13
substrate	Si wafer	Si wafer	Si wafer	Si wafer
wd [cm]	8	8	8	11
st [min]	5	9	15	12
Δf [Hz]	641	1156	1745	400
T [%] at 450 nm	23.0	9.2	3.8	35.2
T [%] at 550 nm	27.5	13.4	6.7	39.8
t_{profil} [nm]	46 ± 4	61 ± 5	83 ± 4	22 ± 3
$t_{\text{x-ray}}$ [nm]		60 ± 3	91 ± 5	20 ± 1

A graphical plot (Fig. 5.4) shows the data of the thickness measurements including the uncertainties. The relation between the mean film thickness t and the frequency shift Δf is achieved by a Least-Square-Approximation [34] and yields a best-fit line

$$t[\text{nm}] = (51.5 \pm 1.2)\,\Delta f[\text{kHz}] \tag{5.2}$$

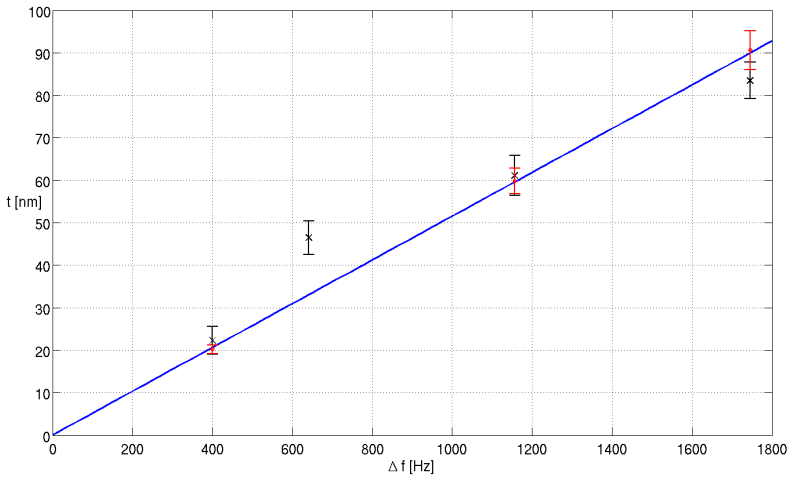

Figure 5.4: Thickness t of platinum thin films related to the frequency shift Δf including the best-fit line (Eq. 5.2)
x (black) ... measurements at the profilometer
o (red) ... measurements with x-ray reflectivity

5.1.2 Thermal Evaporation

Thin layers of gold (Au) are thermally evaporated on microscope slides identical to the substrates used for the sphere arrangement. Maintaining a better adhesion of Au on a glass slide, it's necessary to deposit a several nanometers thin layer of e.g. chromium (Cr) or titanium (Ti) prior to the Au evaporation. For this work a thin layer of Cr improves the adhesion of Au on the microscope slides.

The thickness measurements are performed at the profilometer and by means of x-ray reflectivity. The necessary step profile is obtained by the substrate mounting clip which prevents the deposition of material at the substrate underneath the clip.

The results from the thickness measurements of Cr films as well as the transmission measurements with the spectrophotometer are summarized in Tab. 5.3.

Table 5.3: Thicknesses of thermally evaporated **chromium** films

wd working distance
Δf frequency change
T relative transmission through substrate and film
t measured mean film thickness

sample	cr2	cr3	cr4
substrate	glass	glass	glass
wd [cm]	18	18	18
Δf [Hz]	683	102	70
T [%] at 450 nm	8.8	76.7	81.3
T [%] at 550 nm	9.4	81.7	83.7
d_{profil} [nm]	22 ± 4	6 ± 2	
$d_{\text{X-ray}}$ [nm]	21.8±1.1	5.2 ± 0.3	3.5 ± 0.2

A graphical plot (Fig. 5.5) shows the data of the thickness measurements including the uncertainties. The relation between the mean film thickness d and the frequency shift Δf is achieved by a Least-Square-Approximation [34] and yields a best-fit line

$$t[\text{nm}] = (39.4 \pm 1.1)\, \Delta f[\text{kHz}] \tag{5.3}$$

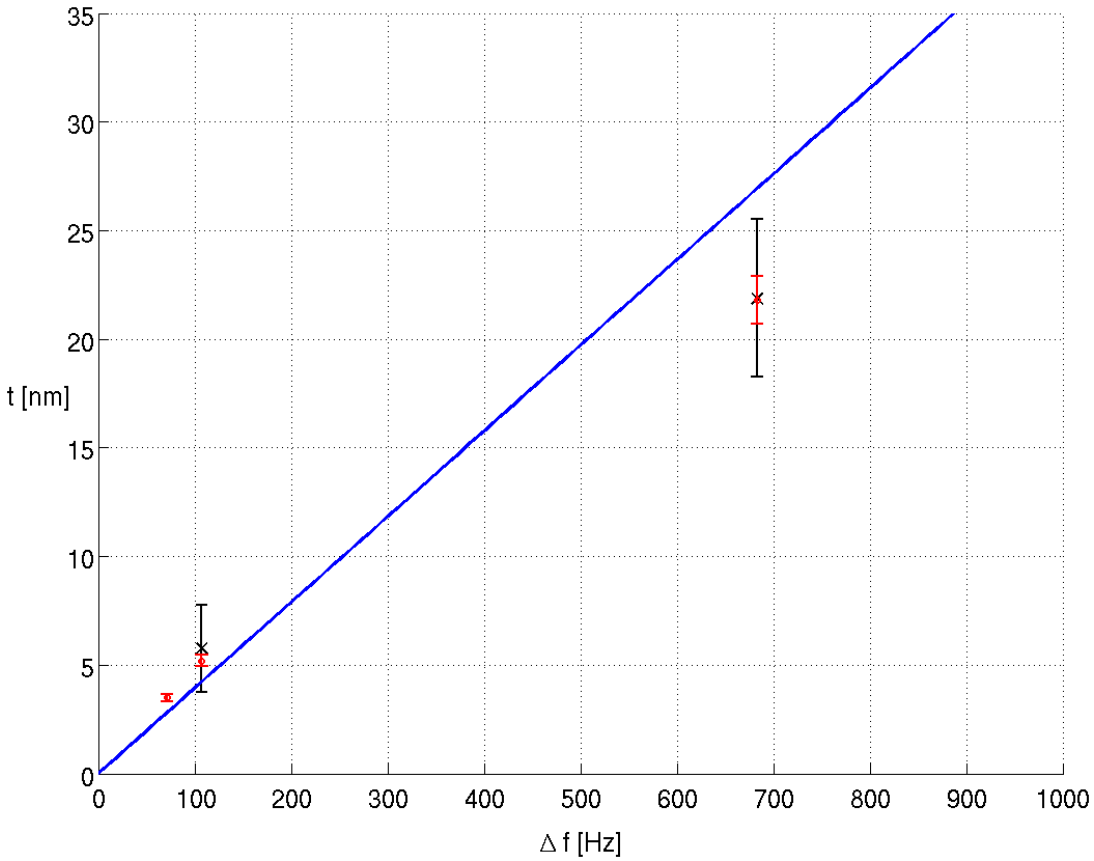

Figure 5.5: Thickness t of chromium thin films related to the frequency shift Δf including the best-fit line (Eq. 5.3)
x (black) ... measurements at the profilometer
o (red) ... measurements with x-ray reflectivity

The results from the thickness measurements of Au films as well as the transmission measurements with the spectrophotometer are summarized in Tab. 5.4.

A graphical plot (Fig. 5.6) shows the data of the thickness measurements deducting the thickness of the Cr adhesion layer. The relation between the mean film thickness t and Δf is achieved by a Least-Square-Approximation [34] and yields a best-fit line

$$t[\text{nm}] = (9.2 \pm 0.4)\, \Delta f[\text{kHz}] \tag{5.4}$$

Table 5.4: Thicknesses of thermally evaporated **gold** films

wd working distance
Δf frequency change
T relative transmission through substrate and film
t measured mean film thickness including a 3 nm Cr adhesion layer

sample	au2	au3	au4	au5
substrate	glass	glass	glass	glass
wd [cm]	18	18	18	18
Δf [Hz]	1015	1993	4496	7319
T [%] at 450 nm	46.8	28.8	9.6	2.5
T [%] at 550 nm	60.9	39.9	13.0	2.8
t_{profil} [nm]	10 ± 2	21 ± 3	44 ± 3	69 ± 3

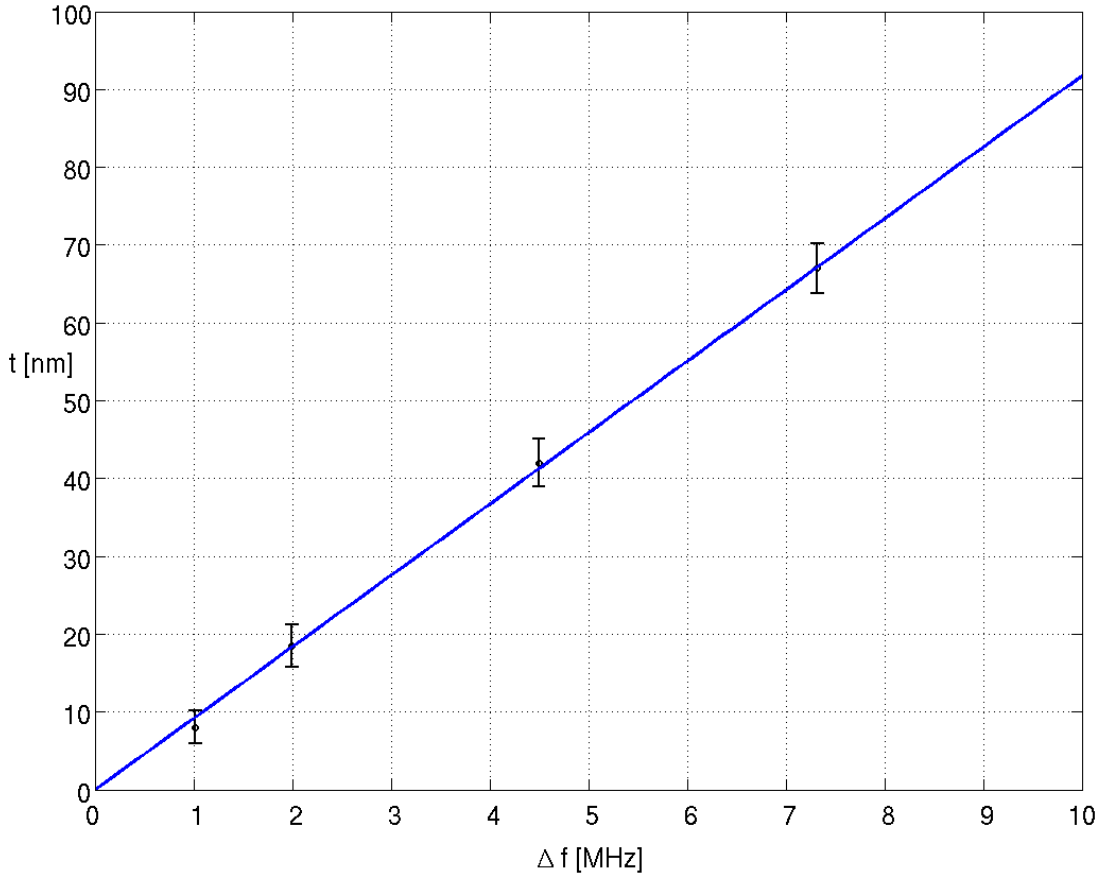

Figure 5.6: Thickness t of gold thin films deducting the Cr adhesion layer of 3 nm thickness related to the frequency shift Δf, including the best-fit line (Eq. 5.4)
o (black) ... measurements at the profilometer

5.2 Properties of the Deposited Films

The goal of this thesis is a periodical, sub-micrometer structure in a thin film of a metal with a high work function, e.g. palladium (Pd) and platinum (Pt), but the first investigations of coated monolayers of polystyrene (PS) spheres by scanning electron microscopy (SEM) have manifested that the fabricated thin films by means of sputter deposition contain lots of cracks independent of the substrate (microscope slide or Si(111) wafer[2]). The SEM images are depicted at Fig. 5.7 and Fig. 5.8.

SEM analyses require a conductive sample surface which in general is realized by depositing a thin gold-palladium (AuPd) alloy, at a ratio of 80:20, due to its smaller grain size compared to pure Au and pure Pd. Based on the missing cracks and the more homogeneous surface of AuPd coated monolayers of PS spheres, the further investigations are performed using thermally evaporated layers of pure Au motivated by its high work function too which is comparable to that of Pd or Pt. Achieving a better adhesion of Au on a glass slide, a 3 nm thin adhesion layer of Cr is evaporated prior to the Au deposition.

Fig. 5.9 shows the apparent improvement in film homogeneity of the Au layer compared to the Pd layer and Pt layer respectively.

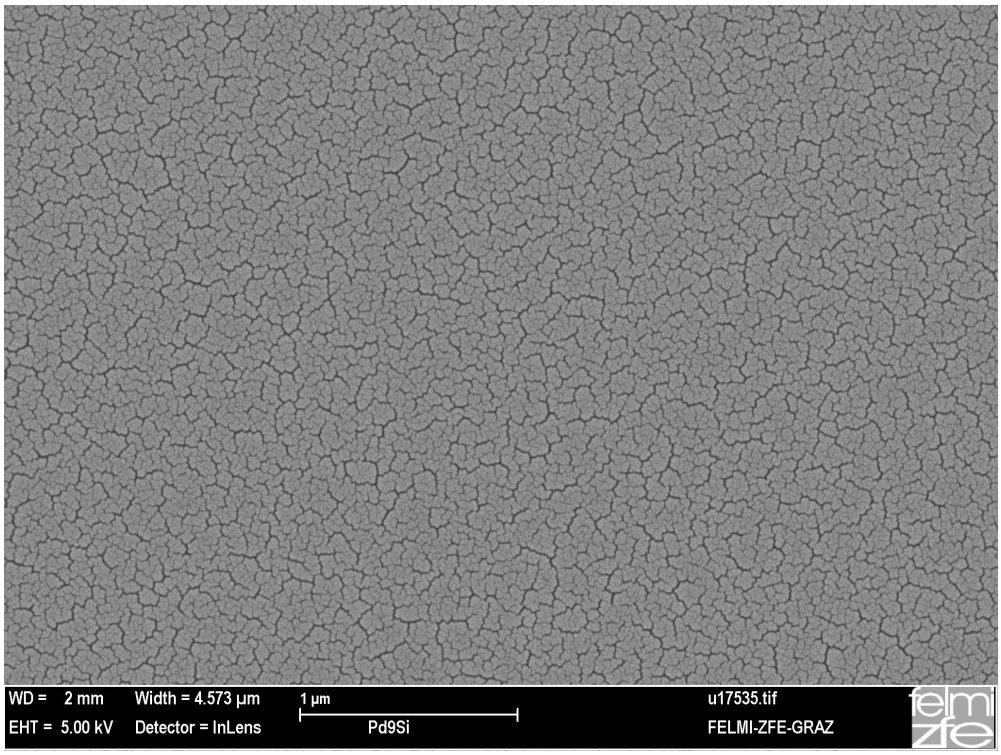

Figure 5.7: SEM images of a sputtered Pd film (thickness: 67 nm) on a Si(111) wafer

[2]supplier: Silchem Handelsgesellschaft mbh (Freiberg, Germany), orientation: (111) 4° off, thickness: 525 µm

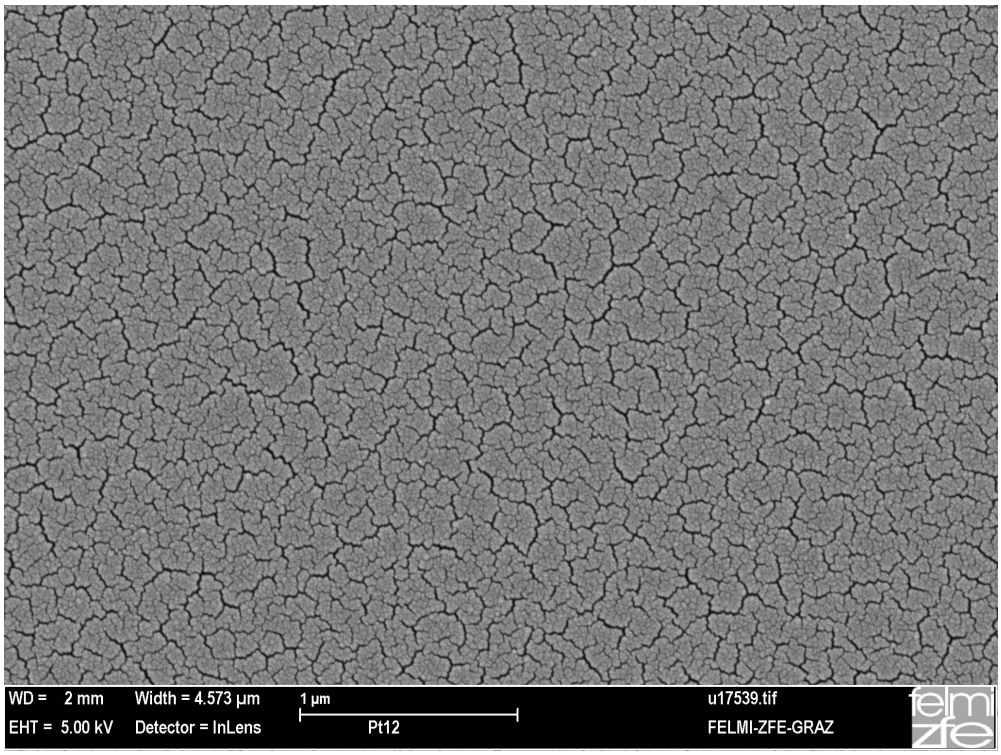

Figure 5.8: SEM images of a sputtered Pt film (thickness: 83 nm) on a Si wafer

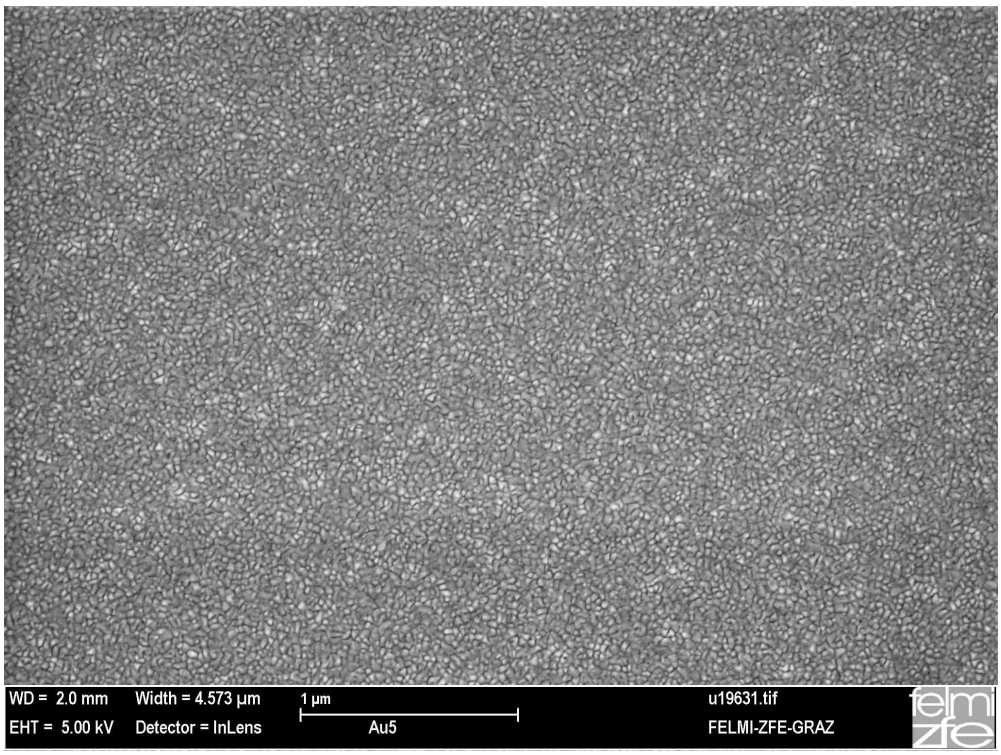

Figure 5.9: SEM images of a thermally evaporated Au film on top of a 3 nm thin Cr adhesion layer on a glass substrate (total thickness of both layers: 69 nm)

5.3 Au Hole Arrays

As already mentioned in detail a metallic hole array is obtained by means of reactive ion etching of a close-packed monolayer of PS spheres, subsequent deposition of the material of interest and the lift-off of the size-reduced spheres.

Based on the findings just described - the more homogeneous layer surface compared to that of Pt and Pd - Au hole arrays are fabricated with varying thickness according to the calibration (section 5.1.2). Different reactive ion etching times enable to tailor the hole diameters. The attainable hole diameters related to the etching time is treated in the next section.

Improving the adhesion of Au at the glass substrate, a 3 nm thin Cr film is deposited underneath the Au layer. Thus the lift-off of the size reduced PS spheres can be performed by a Scotch® adhesion tape enabling a quick and large-area removal with less residues. Cleaning the hole array and removing the remaining size reduced PS spheres, an ultrasonication in toluene or acetone for 20 min is followed. But this ultrasonication can lead to an exfoliation of the Au layer too, especially for large hole diameters.

If the Au layer becomes too thick the removal is complicated or even impossible because neither the solvent due to the lack of the PS contact surface nor the adhesion tape due to the extended and connected Au surface can remove the size reduced spheres anymore. Also worth mentioning is that some kind of passivation occurs if one waits too long to remove the size reduced spheres. Exemplarily depicted at Fig. 4.15: at the lower half of the SEM micrograph the spheres were removed by an adhesion tape, the upper half remained unaffected. One week later several attempts to remove the spheres of the upper half failed, only few spheres could be withdrawn.

Fig. 5.10 shows an optical micrograph of an extended monolayer of PS spheres. Serving as template for the etching and Au coating procedures, the subsequent removal of the size reduced spheres yields the structure illustrated at Fig. 5.11. Monolayer regions become Au hole arrays, bilayer regions become periodic particle arrays of Au. The color impression of the respective layer changes due to a change of the arrangement (from spheres to holes) on the one hand and on the other due to a change of the material (from polystyrene to gold) and consequently a change of the dielectric function.

The scanning electron micrographs depicted at Fig. 5.12 and Fig. 5.13 demonstrate the potential of the applied nanosphere lithography: large-area ($> \mathrm{cm}^2$) hole arrays with sub-micrometer periodicity, but exhibit the limitations too: multicrystalline areas due to disorder caused by the size dispersion of the used PS spheres and by point defects and slip dislocations caused by the evaporation process. Furthermore the lift-off process of the size reduced spheres becomes more difficult the smaller the structure dimensions with respect to the layer thickness as an example illustrates: at Fig. 5.13 a few remaining size reduced spheres are still present.

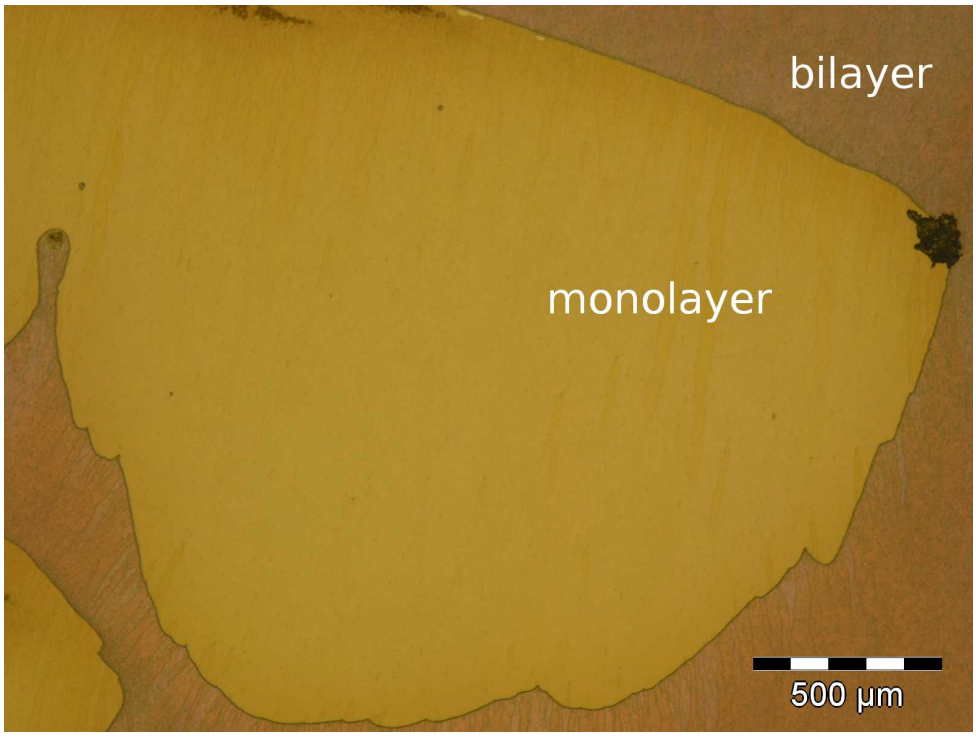

Figure 5.10: Optical micrograph of a close-packed monolayer region
PS sphere diameter: $d = 500\,\mathrm{nm}$

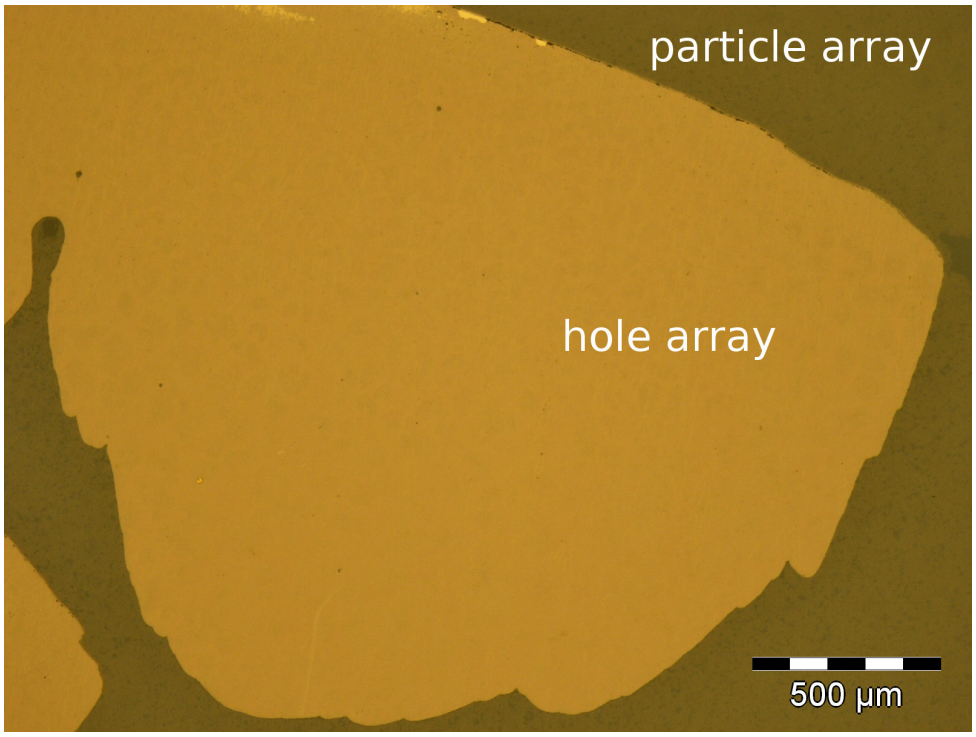

Figure 5.11: Optical micrograph of a Au hole array: $t = 50\,\mathrm{nm}$, $P = 500\,\mathrm{nm}$, $d_{\mathrm{hole}} = 320\,\mathrm{nm}$

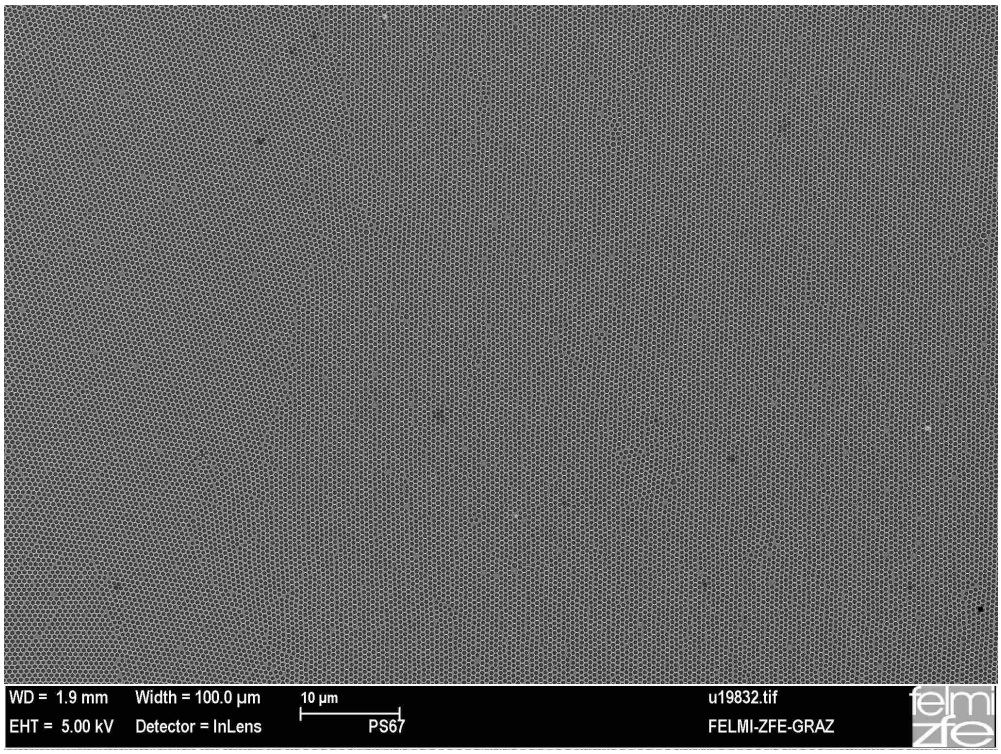

Figure 5.12: SEM micrograph of a Au hole array: $t = 90\,\text{nm}$, $P = 500\,\text{nm}$, $d_{\text{hole}} = 450\,\text{nm}$

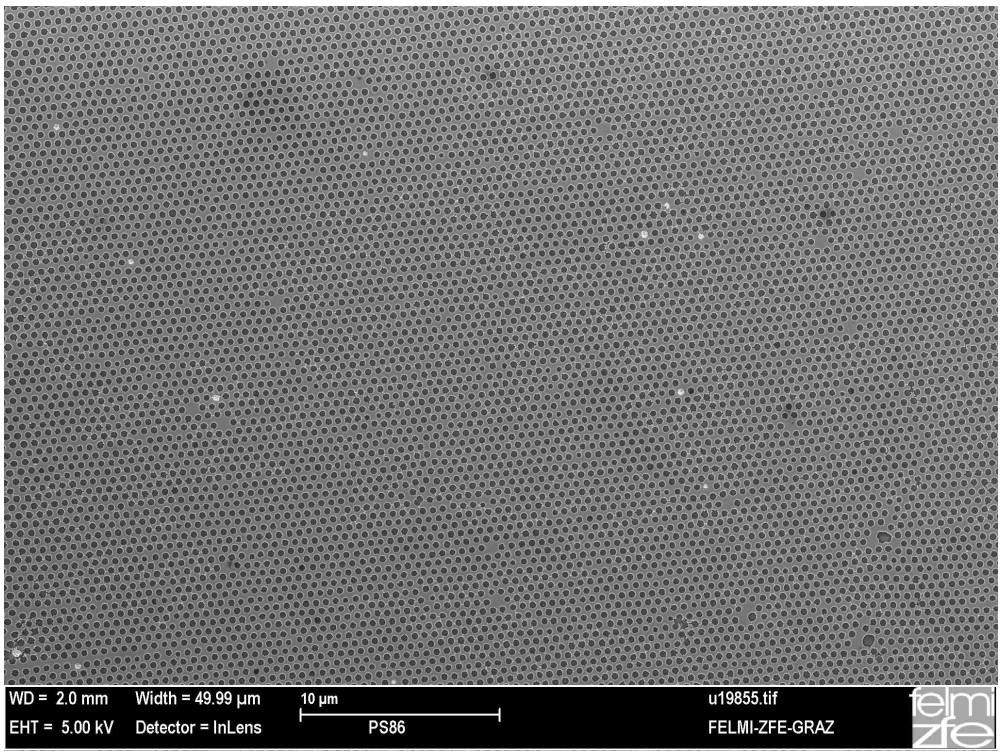

Figure 5.13: SEM micrograph of a Au hole array: $t = 50\,\text{nm}$, $P = 500\,\text{nm}$, $d_{\text{hole}} = 320\,\text{nm}$

5.4 Fill Factor / Hole Diameter

According to section 3.2.1.1 the unit cell area of a close-packed sphere arrangement (hexagonal lattice) with sphere diameter d results in $A_{\text{unit}} = \frac{\sqrt{3}}{2}d^2$. The packing density η is

$$\eta = \frac{A_{\text{sphere}}}{A_{\text{unit}}} = \frac{\pi}{2\sqrt{3}} \approx 0.91\,.$$

As regards metallic hole arrays with hole diameter d_{hole} one considers the respective fill factor ζ of the unit cell with metal:

$$\zeta = 1 - \eta \cdot \left(\frac{d_{\text{hole}}}{d}\right)^2 \tag{5.5}$$

The fill factors of a hole array with period $d = 500\,\text{nm}$ (original sphere diameter) are calculated with respect to the hole diameters:

d_{hole} [nm]	450	400	350	300
ζ	0.27	0.42	0.56	0.67

The impact of the ion etching procedure on a close-packed 500-nm PS sphere arrangement is demonstrated at Fig. 5.15 for different etching times $t = 50\,\text{s}$ up to $t = 300\,\text{s}$. Both the obtained size reduced sphere diameters and the hole diameters of the Au hole arrays are related to the etching time and are plotted at Fig. 5.14.

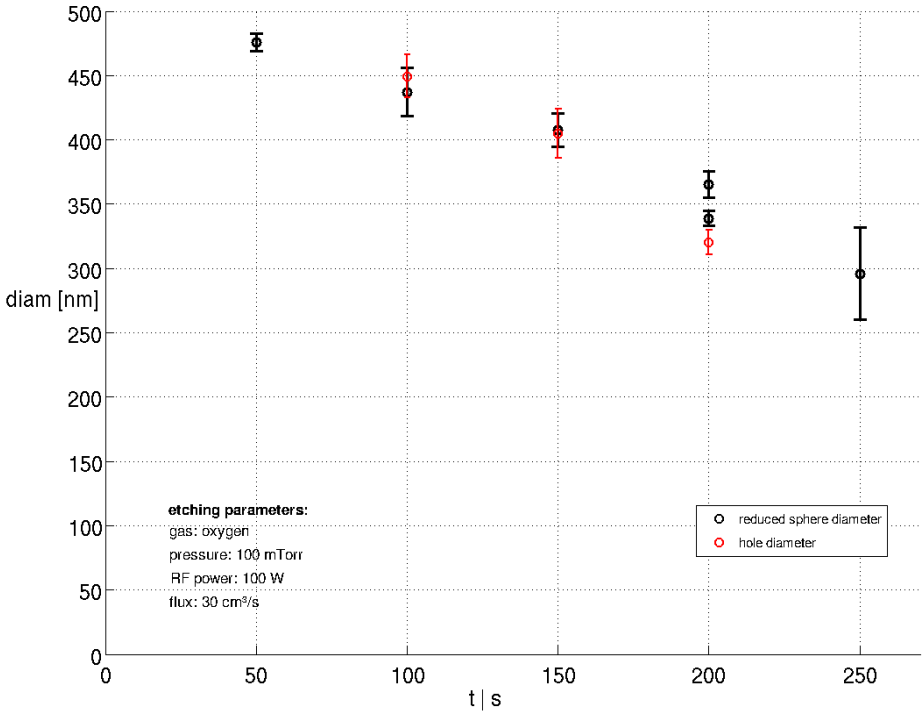

Figure 5.14: Reduced sphere diameter after reactive ion etching (black) and hole diameter of the metallic hole array respectively (red) as function of the etching time t

The etching parameters are indicated inside the figure. Practical etching times for a PS sphere arrangement (diameter: $d = 500\,\text{nm}$) range up to 250 - 300 s resulting in sphere diameters of 300 - 250 nm. Extending this etching time, the PS spheres decompose into smaller particles as the image of the longest etching time $t = 300\,\text{s}$ demonstrates.

The hole diameters at a particular etching time correspond almost exactly to the reduced sphere diameters (Fig. 5.14) indicating on the one hand an approximately parallel Au deposition and on the other a reduced spheres removal without taking off parts of the Au layer deposited on top of a Cr adhesion layer on a glass substrate.

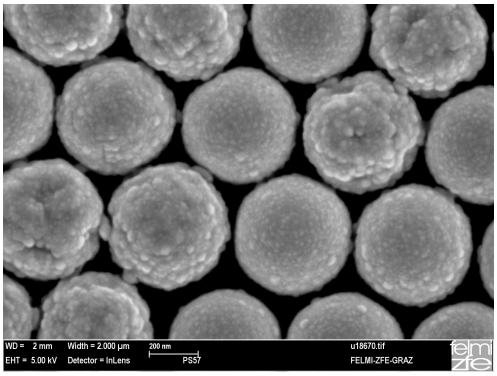

etching time: $t = 50\,\text{s}$

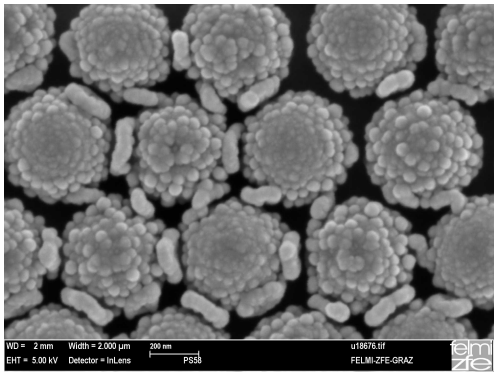

etching time: $t = 100\,\text{s}$

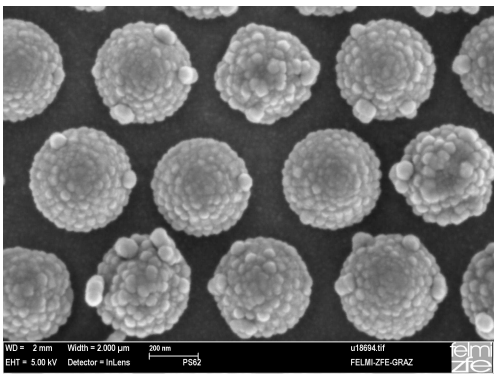

etching time: $t = 150\,\text{s}$

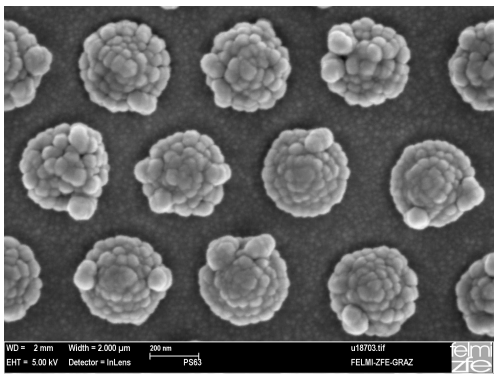

etching time: $t = 200\,\text{s}$

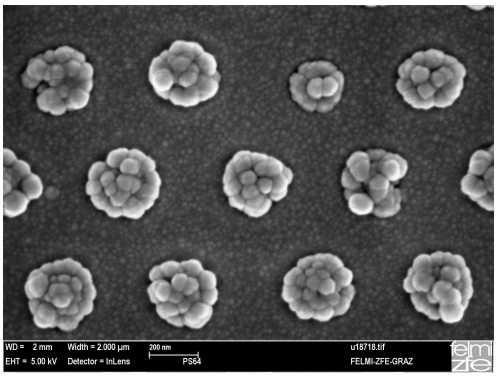

etching time: $t = 250\,\text{s}$

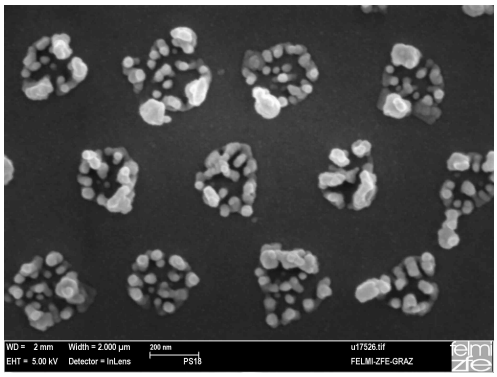

etching time: $t = 300\,\text{s}$

Figure 5.15: SEM images of 500-nm PS monolayer regions after reactive ion etching with different etching times

6 Results

This chapter deals with the dielectric and electrical properties of the fabricated structures: patterned metal layers (coated monolayers, hole arrays), unstructured metal films and layers of close-packed PS spheres. They are characterized by means of transmission measurements, specific resistivity measurements and spectroscopic ellipsometry.

Based on this characterization the influences of layer thickness, periodicity and structure sizes on the dielectric and electrical properties of the patterned thin metal films are figured out.

6.1 Transmission Spectra

Transmission spectra are recorded of

- ⇒ close-packed PS sphere layers with diameter $d = 500\,\text{nm}$,
- ⇒ close-packed PS sphere monolayers ($d = 300\,\text{nm}$ and $d = 500\,\text{nm}$) coated with AuPd (80:20), Pd and Au,
- ⇒ Au hole arrays (hexagonal lattice, period $P = 500\,\text{nm}$) with different hole diameters.

The metal layers whether patterned or not are fabricated with thicknesses ranging from 18 nm to 130 nm figuring out its influence on the transmission spectra. Facilitating statements about the quality of the fabricated structures, the transmission spectra are measured at different positions by means of a fiber optics attached to a CCD spectrometer (effective measurement area: $\approx 0.1\,\text{mm}^2$) and if the area sizes are large enough by means of a photospectrometer too (effective measurement area: $\approx 20\,\text{mm}^2$).

As references serve either the transmission spectra through the glass substrate or the transmission spectra through the unstructured metal layer and the glass substrate.

6.1.1 Layers of Close-Packed Polystyrene Spheres

Periodically arranged PS spheres exhibit a distinctive color impression according to the respective sphere assembly in monolayers or multilayers when illuminated with white light. This photonic behavior caused by the sub-micrometer periodicity of the refractive index is demonstrated by digital photographs and optical micrographs taken in reflectance and in transmission of the fabricated structures evinced in chapter *Fabrication of Sphere Monolayers*.

Measured by means of the Ocean Optics CCD spectrometer, the relative transmission spectra of the PS sphere layers with diameter $d = 500\,\text{nm}$ are depicted in Fig. 6.1. All three spectra show a main dip at $\lambda \approx 630\,\text{nm}$ corresponding to $\lambda \approx 1.26\,d$. The figure reveals: the more layers the more pronounced the transmission spectra with respect to the number of relative maxima and relative minima, and the more layers the less the direct transmission.

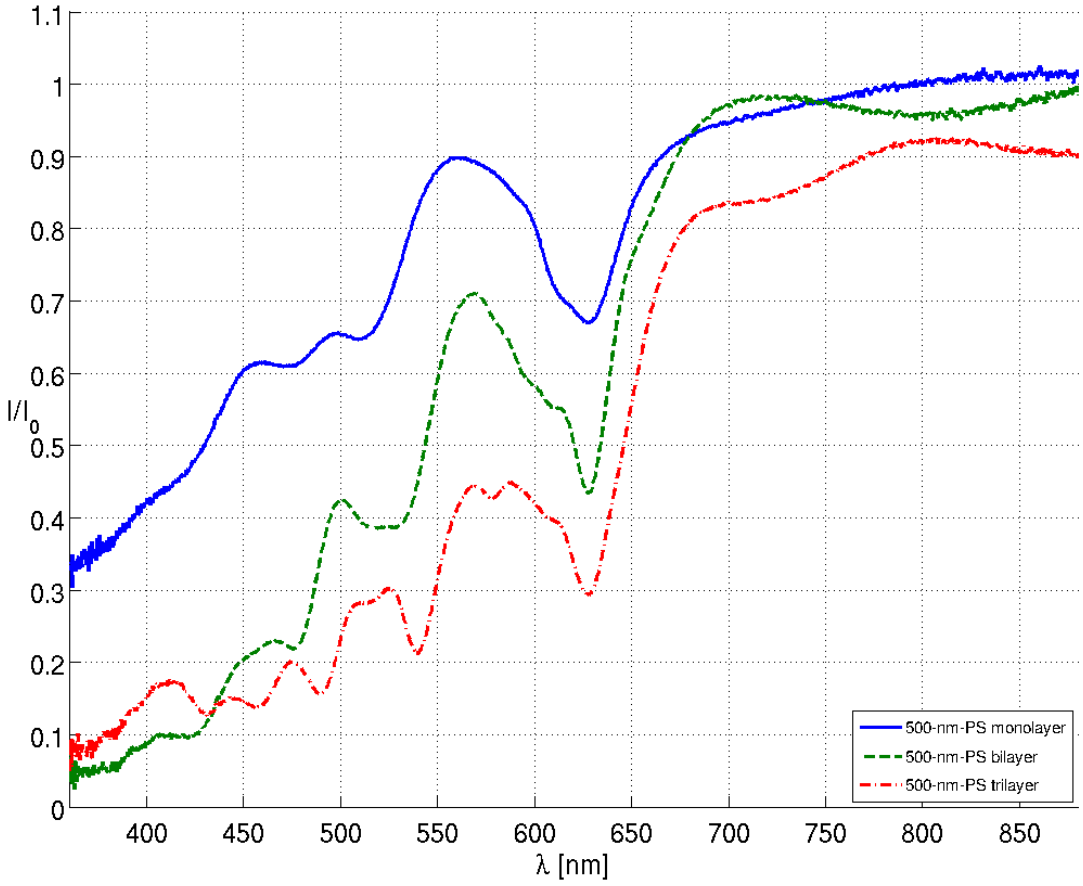

Figure 6.1: Relative transmission through different close-packed PS sphere layers
PS sphere diameter: 500 nm
Reference (I_0): transmission through glass substrate

6.1.2 Metal Coated Monolayers of Closed-Packed Polystyrene Spheres

The transmission of light through periodically sub-micrometer patterned metal layers is influenced by the excitation of surface plasmons right at the interface between a dielectric and a metal as described in section 2.4.1. Thus an enhanced transmission can be expected for metal coated monolayers of close-packed PS spheres too, as e.g. reported in [35] and [36] dealing with silica and PS spheres.

For this work PS spheres with diameters of $d = 300\,\text{nm}$ and $d = 500\,\text{nm}$ respectively are used. As coating materials serve gold-palladium (AuPd) - ratio 80:20, palladium (Pd) and gold (Au).

6.1.2.1 AuPd Coating - Different Sphere Diameters

Investigating the first fabricated PS sphere monolayers by SEM, a conductive surface of the specimen is required. For this purpose the samples are coated with a 18 nm thin AuPd layer.

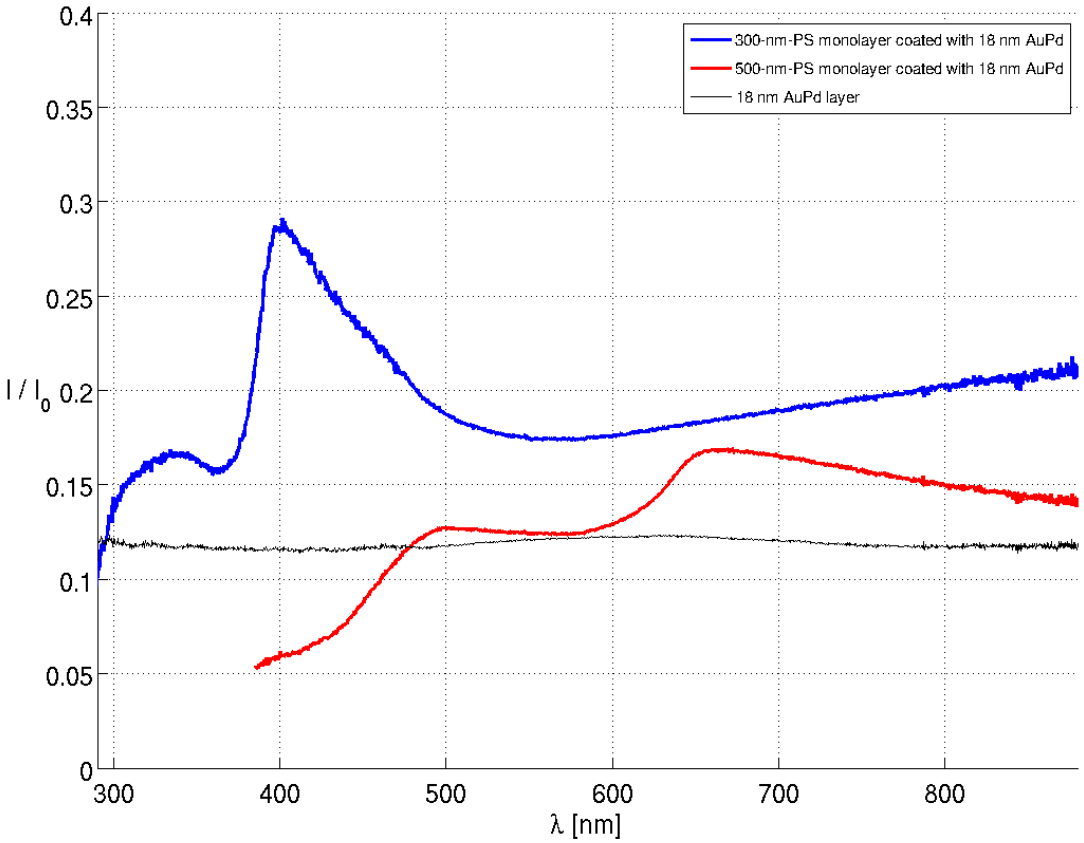

Figure 6.2: Relative transmission spectra of hexagonally close-packed PS sphere monolayers of different diameters coated with 18 nm of AuPd as well as the relative transmission spectrum of the AuPd layer alone (black).
Reference (I_0): transmission through glass substrate

The transmission spectra are recorded by the Ocean Optics CCD spectrometer. Dealing with monolayers of PS spheres with diameter $d = 300\,\text{nm}$ the transmission is measured additionally with the Deuterium light source to extend the wavelength range down to UV. The respective relative transmission spectra are depicted in Fig. 6.2 and in Fig. 6.3.

In the UV-A/visible spectral range two maxima occur in each spectra of the coated monolayers whereby the main peak at $\lambda \approx 400\,\text{nm}$ and at $\lambda \approx 670\,\text{nm}$ respectively is in both cases related to $1.34\,d$. The second peak at shorter wavelengths corresponds exactly to the PS sphere diameter in the case of $d = 500\,\text{nm}$ and approximately ($\lambda \approx 335\,\text{nm}$) in the case of $d = 300\,\text{nm}$.
These transmission maxima seem to correspond to transmission resonances mediated by surface plasmon (SP) excitations (Eq. 2.34) with the shortest reciprocal lattice vector ($n_1 = 1$ or $n_2 = 1$) of the respective interface: metal - polystyrene and metal - air. Thus the peak at the larger wavelength can be assigned to the metal - polystyrene interface due to the higher dielectric constant of PS ($\varepsilon_\text{d} \approx 1.59$) compared to that of air ($\varepsilon_\text{d} \approx 1$).

Fig. 6.3 shows the same transmission spectra as in the previous figure but choosing as reference the transmission through the coated glass substrate. As a result the enhanced transmission through a periodically patterned metallic layer at least at wavelengths larger than the periodicity (300 nm and 500 nm respectively) becomes apparent.

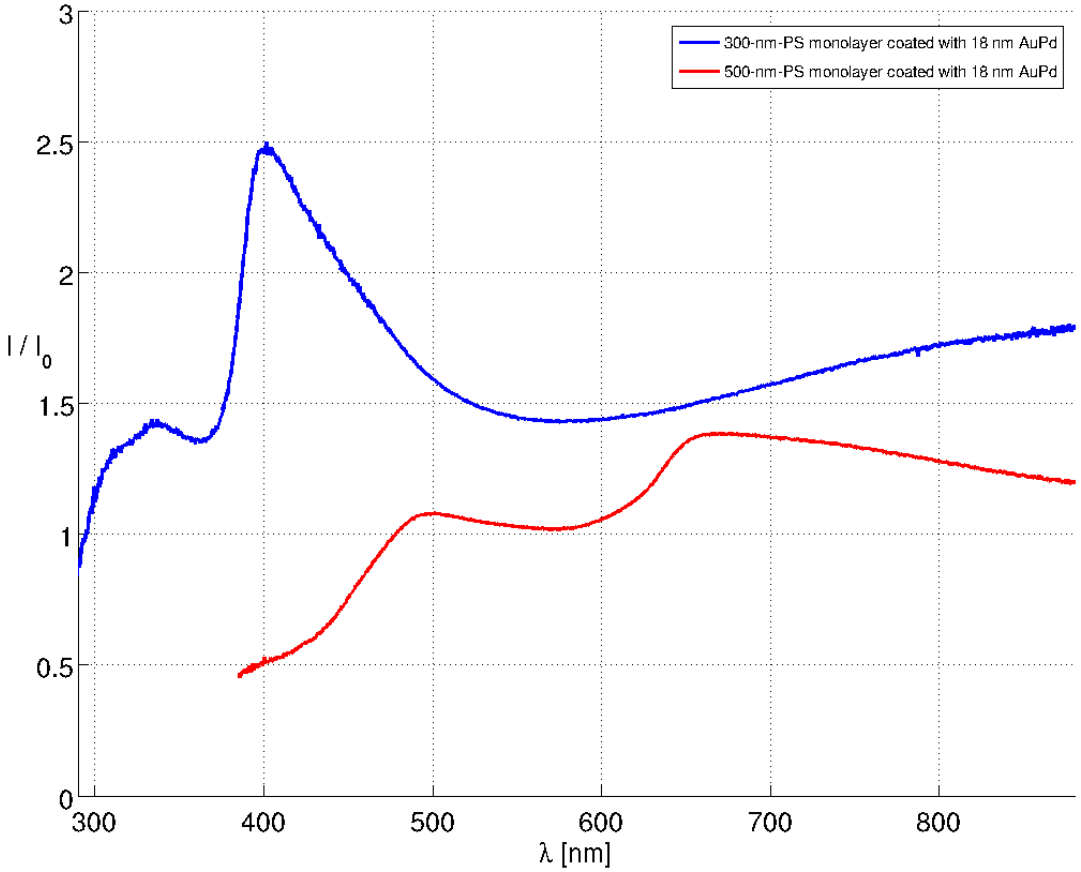

Figure 6.3: Relative transmission spectra of hexagonally close-packed PS sphere monolayers of different diameters, both coated with 18 nm of AuPd
Reference (I_0): transmission through the glass substrate covered with 18 nm AuPd

6.1.2.2 Pd Coating - Different Layer Thicknesses

Hexagonally close-packed PS sphere monolayers with diameters of $d = 500\,\text{nm}$ are coated with Pd of thickness $t = 30\,\text{nm}$, $t = 80\,\text{nm}$ and $t = 130\,\text{nm}$. Although the deposited Pd layers contain lots of cracks (see 5.2 for details) transmission resonances can still be observed. The transmission spectra are recorded by the Ocean Optics CCD spectrometer and related to transmission through the glass substrate depicted in Fig. 6.4 and to the transmission through the glass substrate coated with the respective unstructured Pd layer depicted in Fig. 6.5.

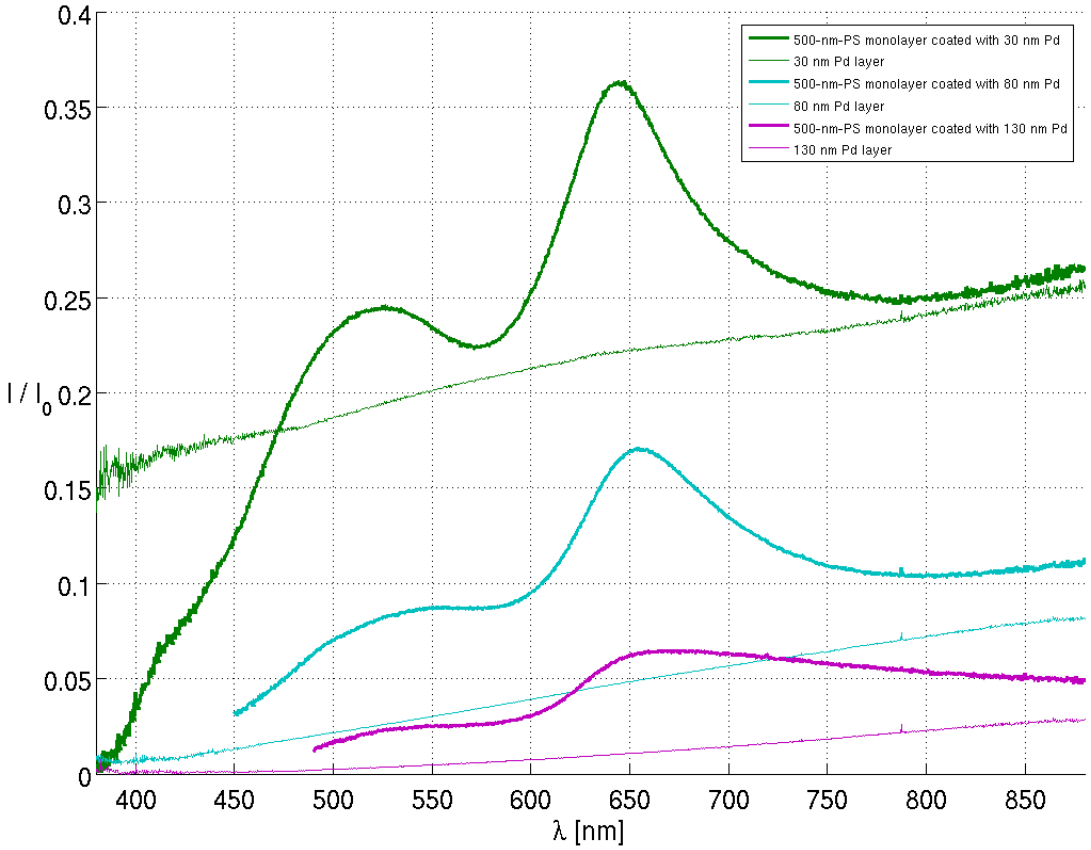

Figure 6.4: Relative transmission spectra of hexagonally close-packed PS sphere monolayers coated with different thicknesses of Pd as well as the associated relative transmission spectra of the unstructured Pd layers.
Reference (I_0): transmission through glass substrate

The transmission spectra of monolayers coated with different thicknesses of Pd all exhibit two maxima like the monolayers coated with AuPd of the previous section originating from excitations of surface plasmons (SP) by the incident light on both sides of the metal.
The peak at $\lambda \approx 650\,\text{nm}$ ($\lambda \approx 1.3\,d$) is well pronounced in both figures while the peak at $\lambda \approx 500\,\text{nm}$ ($\lambda \approx d$) emerges clearer in the spectra related to the unstructured Pd layer. As in the case of the PS sphere monolayers coated with AuPd, the peaks seem to correspond to transmission resonances mediated by SP excitations (Eq. 2.34) at both metal interfaces: the longer wavelength peak to the metal - polystyrene interface, the shorter wavelength peak to the metal - air interface. Their positions are independent of the layer thickness but become shal-

lower as the layer thickness is increased. Generally speaking the topology of the coated Pd layers caused by the PS sphere monolayer leads to a transmission enhancement throughout the recorded spectral range except for the thinnest layer ($t = 30\,\mathrm{nm}$) at $\lambda < 470\,\mathrm{nm}$.

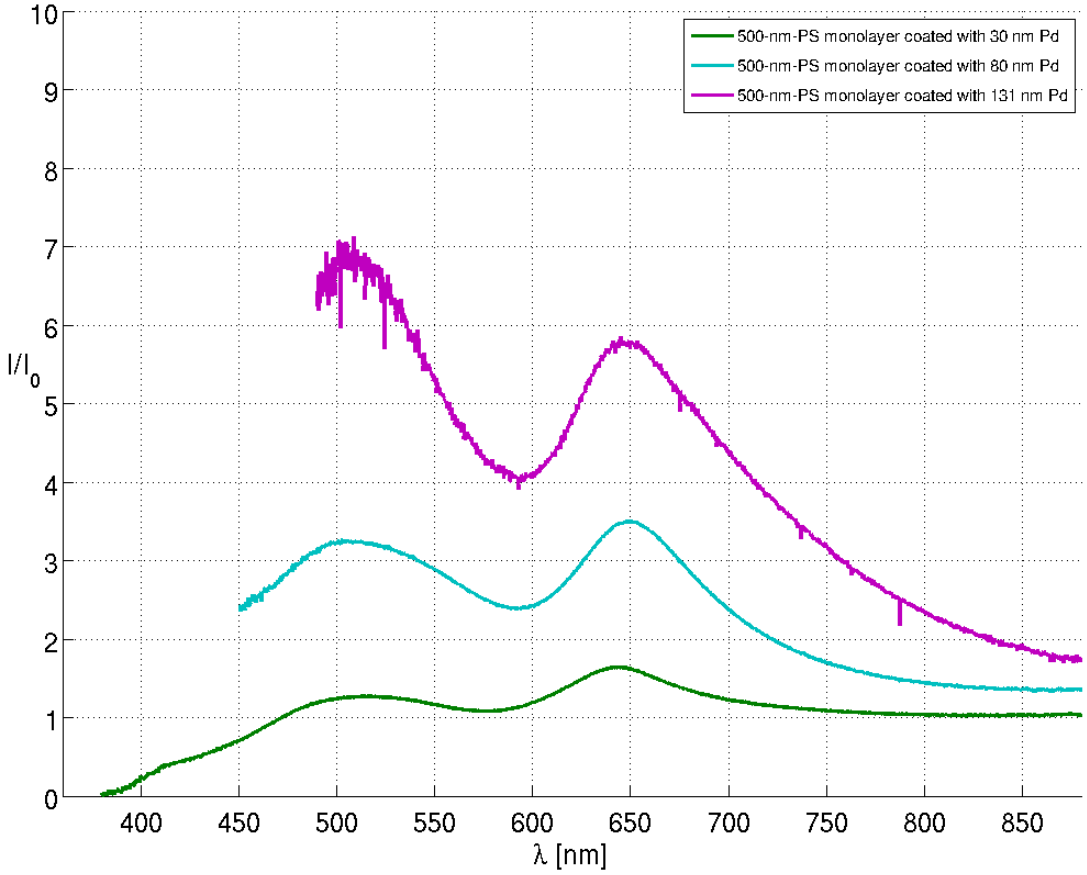

Figure 6.5: Relative transmission spectra of hexagonally close-packed PS sphere monolayers coated with different thicknesses of Pd.
Reference (I_0): transmission through the respective unstructured Pd layer

The transmission enhancement related to the transmission through the unstructured layer (depicted in Fig. 6.5) seems to be thickness dependent: the thicker the film the more enhanced the transmission. In the case of the thinnest layer ($t = 30\,\mathrm{nm}$) the maximum enhancement occurs at the longer wavelength peak ($\lambda \approx 650\,\mathrm{nm}$), the 80 nm thick layer shows approximately the same enhancement for both peaks and in the case of the thickest layer ($t = 130\,\mathrm{nm}$) the maximum enhancement appears at the shorter wavelength peak ($\lambda \approx 500\,\mathrm{nm}$). Considering the transmission of light through a periodically patterned metal layer mediated by SP resonances, one may argue that the thicker the film the more difficult to excite SP at the metal - polystyrene interface and thus the position of the maximum enhancement shifts to the shorter wavelength peak assigned to the SP excitation at the metal - air interface.

6.1.2.3 Au Coating - Different Layer Thicknesses

Hexagonally close-packed monolayers of PS spheres with diameter of $d = 500\,\text{nm}$ are coated with Au of thickness $t = 58\,\text{nm}$, $t = 66\,\text{nm}$ and $t = 91\,\text{nm}$. Fabricating metal layers comparable to the Au hole arrays discussed below, an adhesion layer of 3 nm Cr is deposited underneath the Au coatings.

The transmission spectra are recorded by means of the Oriel CCD spectrometer and additionally by means of the Lambda 9 spectrophotometer due to large monolayer areas originating from the fabrication processes described in the sections *Drop Casting, Generation 4* and *Dip Coating*. The spectra are related to the spectra through the glass substrate (Fig. 6.6 and Fig. 6.7) as well as to the spectra through the coated glass substrate (Fig. 6.8).

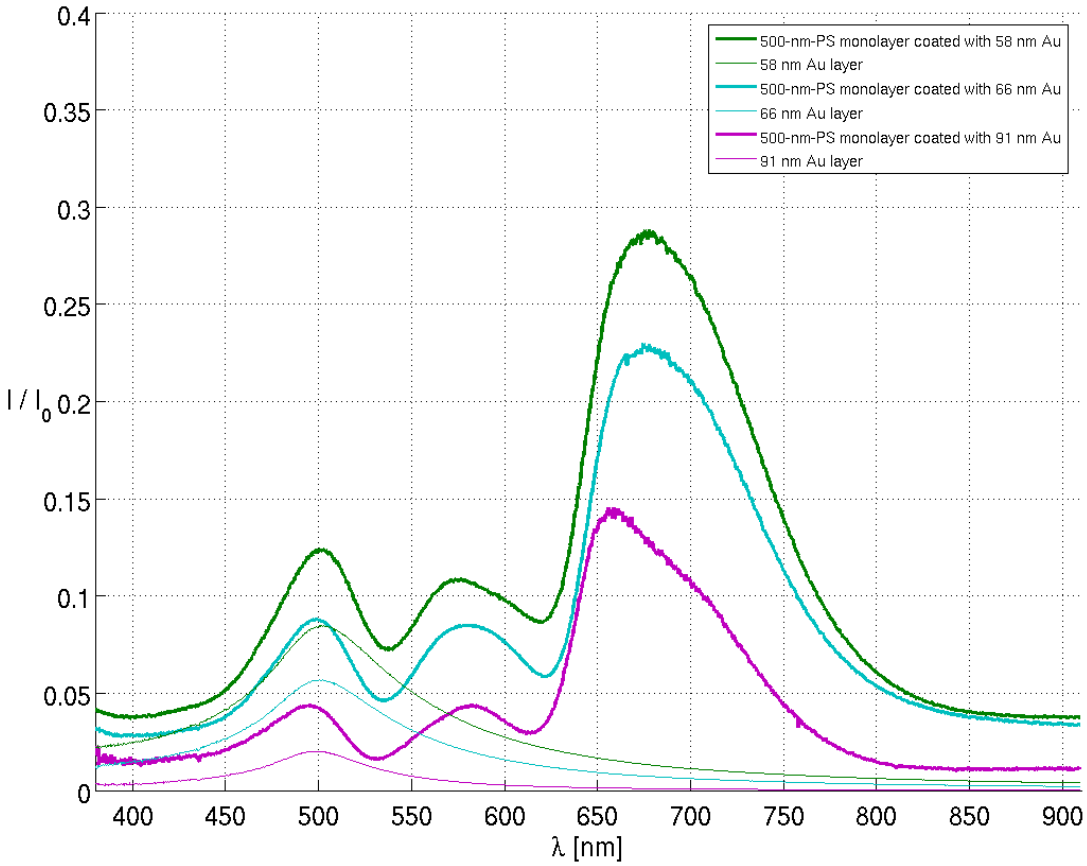

Figure 6.6: Relative transmission spectra of hexagonally close-packed PS sphere monolayers on a glass substrate coated with different thicknesses of Au as well as the associated relative transmission spectra of the unstructured Au layers.
Reference (I_0): transmission through glass substrate

The transmission spectra related to the transmission through the glass substrate (Fig. 6.6) show three resonances in the visible spectral range. Extending the spectral range to the near infrared (Fig. 6.7), a fourth, broader peak reveals at $\lambda \approx 1100\,\text{nm}$.
The peak at $\lambda \approx 500\,\text{nm}$ corresponds to the well known plasma resonance of Au manifested

by the respective, associated relative transmission spectra of the unstructured Au layer. As already mentioned in the previous sections the two remaining peaks in the visible wavelength range seem to correspond to transmission resonances mediated by SP excitations of the incident light at both metal interfaces: the longer wavelength peak to the metal - polystyrene interface, the shorter wavelength peak to the metal - air interface. Their positions depends slightly on the film thickness due to the spectral feature of the respective unstructured Au layers.

The quality and area size of the monolayer regions illustrate a comparison of the transmission spectra depicted in both figures: while the fiber optic attached to the CCD spectrometer exhibits an effective measurement area of $0.1\,\mathrm{mm}^2$, the spectrophotometer collects light of an area of $20\,\mathrm{mm}^2$. The transmission spectra coincide almost precisely as regards the peak position as well as the peak intensity.

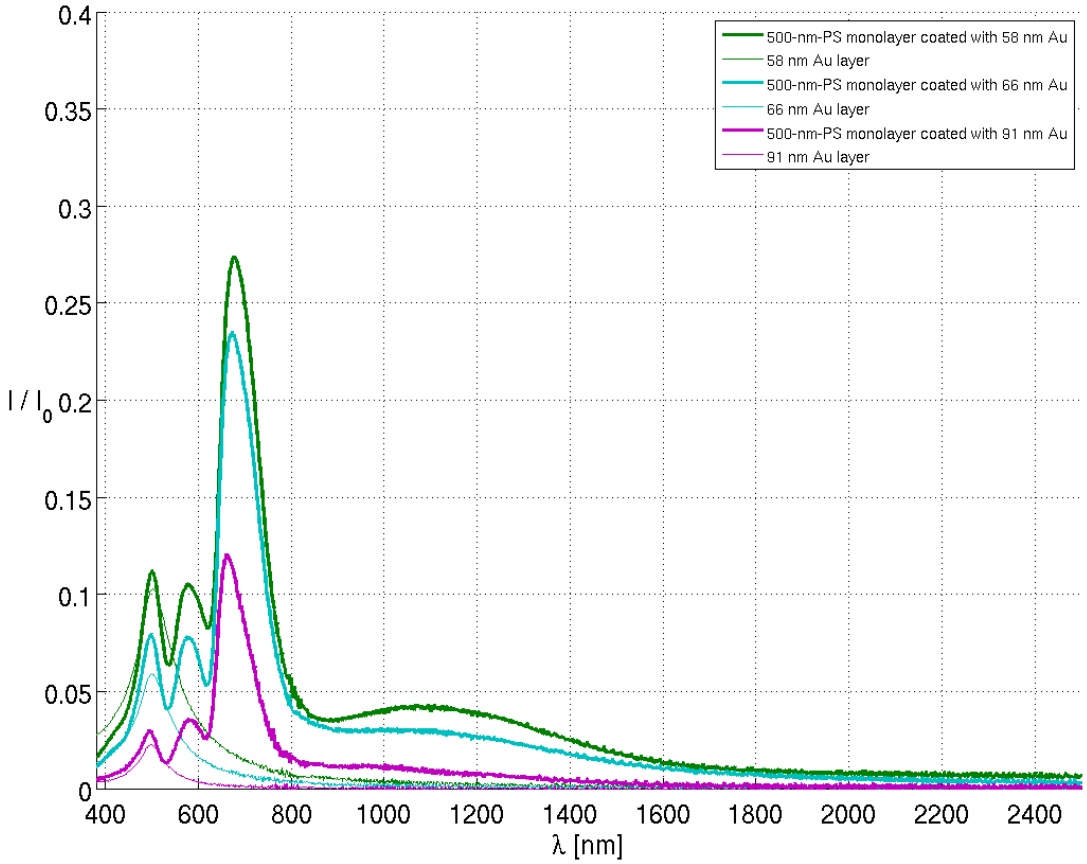

Figure 6.7: Relative transmission spectra of hexagonally close-packed PS sphere monolayers on a glass substrate coated with different thicknesses of Au and the associated relative transmission spectra of the unstructured Au layers.
Reference (I_0): transmission through glass substrate

Related to the transmission through the respective coated glass substrate (depicted in Fig. 6.8) the main peak position keeps constant at $\lambda \approx 700\,\mathrm{nm}$ ($\lambda \approx 1.4d$). The second peak is less pronounced and slightly thickness dependent: $\lambda \approx 590\,\mathrm{nm}$ ($\lambda \approx 1.18d$) at the 91 nm thick layer and $\lambda \approx 600\,\mathrm{nm}$ ($\lambda \approx 1.2d$) at the 66 nm thick one, the peak at the 58 nm thick layer is unidentifiable.

The transmission of the structured layers compared to the respective unstructured Au layer is enhanced at all 3 layers throughout the visible wavelength range. The thickest structured layer shows an enhancement of approximately 140 compared to the unstructured layer. The thickness dependence of the transmission enhancement is comparable to that of the structured Pd layers: the thicker the film the more enhanced the transmission.

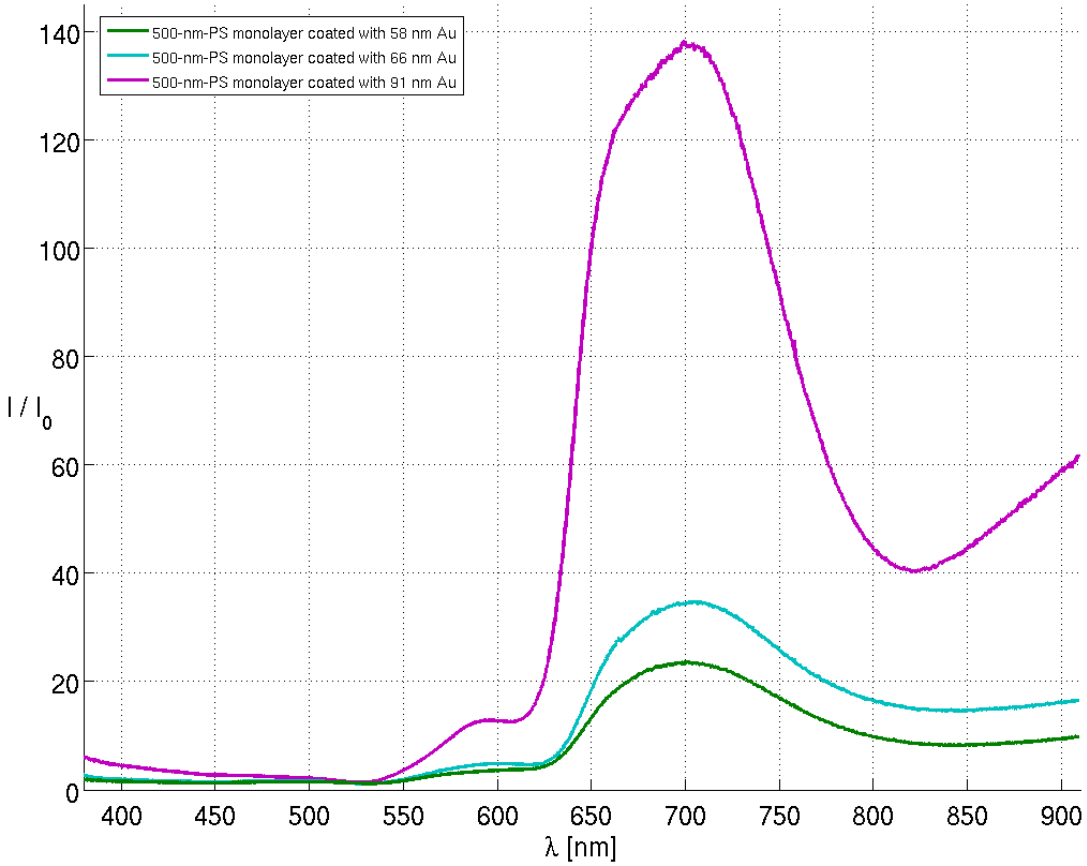

Figure 6.8: Relative transmission spectra of hexagonally close-packed PS sphere monolayers on a glass substrate coated with different thicknesses of Au.
Reference (I_0): transmission through the respective unstructured Au layer

6.1.3 Au Hole Arrays

The transmission spectra are recording using the Oriel CCD spectrometer as well as the Lambda 9 spectrophotometer due to the large monolayer areas produced according to the fabrication process described in the sections *Drop Casting, Generation 4* and *Dip Coating*. Improving the adhesion of Au on a glass substrate, a 3 nm thick Cr layer is deposited underneath all Au layers.

Fig. 6.9 depicts the relative transmission spectra in the visible wavelength range of Au hole arrays with different hole diameters while the layer thickness $t = 90\,\text{nm}$ and their periodicity $P = 500\,\text{nm}$ are kept constant. The same spectra but extended to the near infrared wavelength region is plotted in Fig. 6.10 which includes the relative transmission through a coated monolayer of the same thickness for comparison too. Both figures contain the relative transmission through the unstructured Au layer of the same thickness as well.

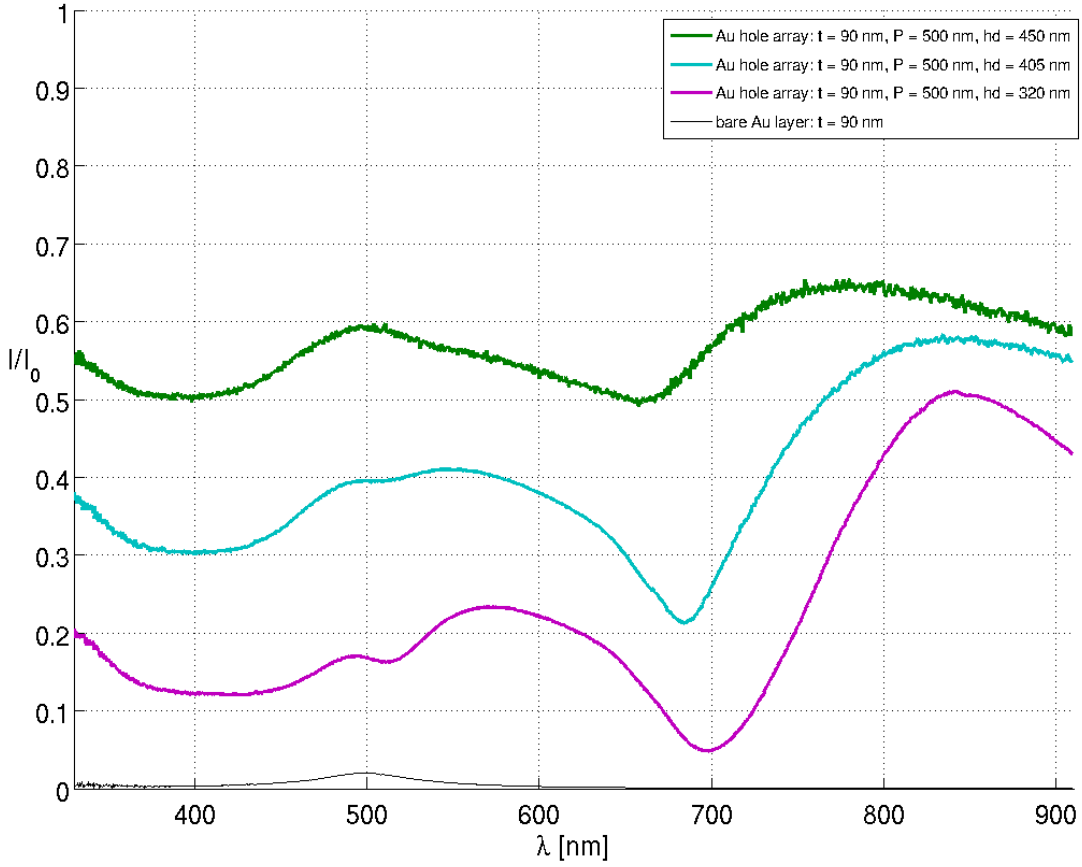

Figure 6.9: Relative transmission spectra of Au hole arrays (thickness $t = 90\,\text{nm}$) with varying hole diameters d_{hole}.
Reference (I_0): transmission through glass substrate

The relative transmission spectrum of the Au hole array with $d_{\text{hole}} = 320\,\text{nm}$ shows three well pronounced peaks at $\lambda \approx 500\,\text{nm}$, $\lambda \approx 570\,\text{nm}$ and $\lambda \approx 830\,\text{nm}$. The first peak matches with the plasma resonance of Au manifested in the transmission spectra of the unstructured Au layer.

The remaining two peaks seem to correspond to transmission resonances mediated by surface plasmons (SP) excitations (Eq. 2.34) with the shortest reciprocal lattice vector ($n_1 = 1$ or $n_2 = 1$) at the air - gold interface ($\lambda \approx 570\,\text{nm}$) and at the substrate - (chromium) - gold interface ($\lambda \approx 830\,\text{nm}$). This assumption is supported by a comparison to the relative transmission spectra of the PS sphere monolayer coated with the same thicknesses of Cr and Au: the peaks assignable to SP excitations at the air - gold interface arise approximately at the same wavelength while the position of the peak originating from SP excitations at the substrate -(chromium) -gold interface and the polystyrene -(chromium) -gold interface respectively differ significantly.

The longest wavelength peak of the all Au hole arrays exhibit a long extension into the infrared spectral region representing the exponential decay of the non-resonant (direct) distribution of the transmission process.

With increasing hole diameter the two SP resonant transmission peaks shift towards smaller wavelengths. In the case of the Au hole array with $d_{\text{hole}} = 450\,\text{nm}$ the SP resonance peak originating from the air - gold interface and the peak of the Au plasma resonance coincide.

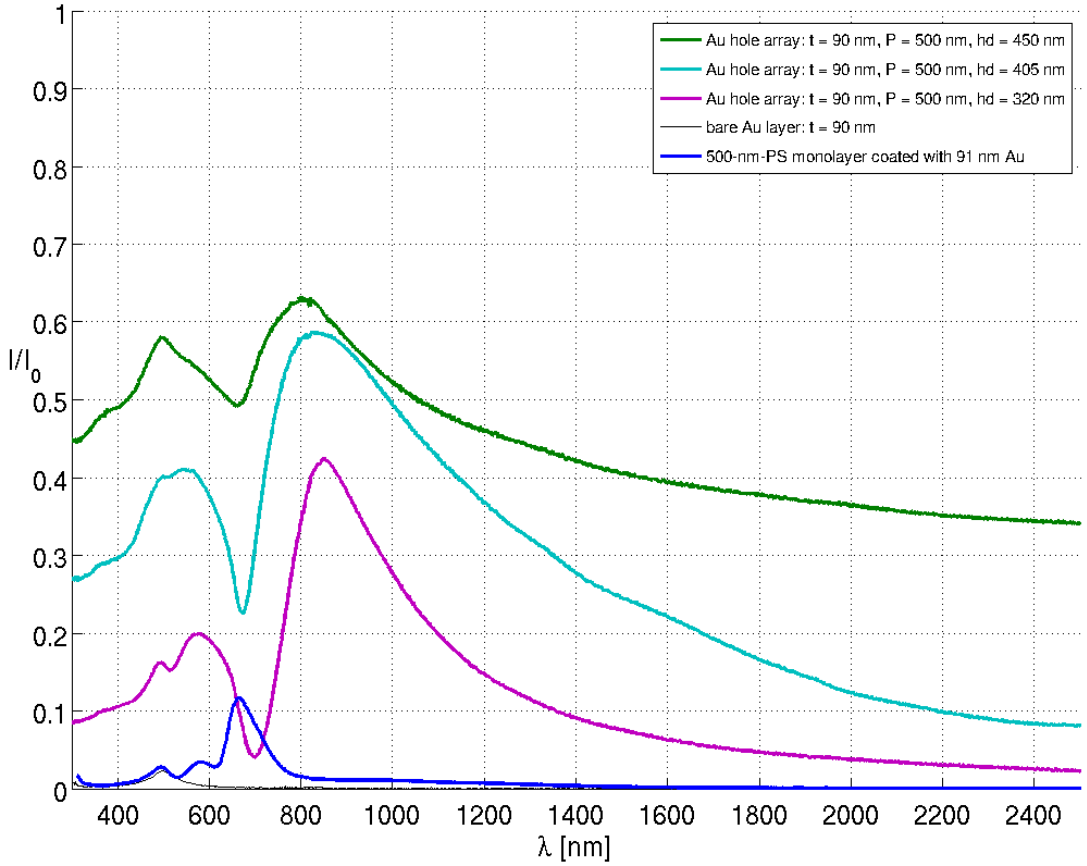

Figure 6.10: Relative transmission spectra in the visible and near IR wavelength range of a Au hole array (thickness $t = 90\,\text{nm}$) with varying hole diameters d_{hole}.
Reference (I_0): transmission through glass substrate

Fig. 6.11 and Fig. 6.12 depict the dependence of the relative transmission spectra through a Au hole array with $d_{\text{hole}} = 450\,\text{nm}$ and $d_{\text{hole}} = 320\,\text{nm}$ respectively on different layer thicknesses. Again both figures contain the relative transmission through the associated unstructured Au layer of the same thickness. The transmission spectra are recorded at different positions of the respective sample indicated by the same color of the graphs. These graphs match each other pretty well implicating an approximately identical hole arrangement throughout a sample.

As already mentioned above, the spectra of the Au hole arrays with periodicity $P = 500\,\text{nm}$ exhibit two transmission resonances originating probably from excitation of surface plasmons of the incident light at the substrate-(chromium)-gold interface and at the air-gold interface respectively. The latter partly coincide with the Au plasmon resonance at $\lambda \approx 500\,\text{nm}$.

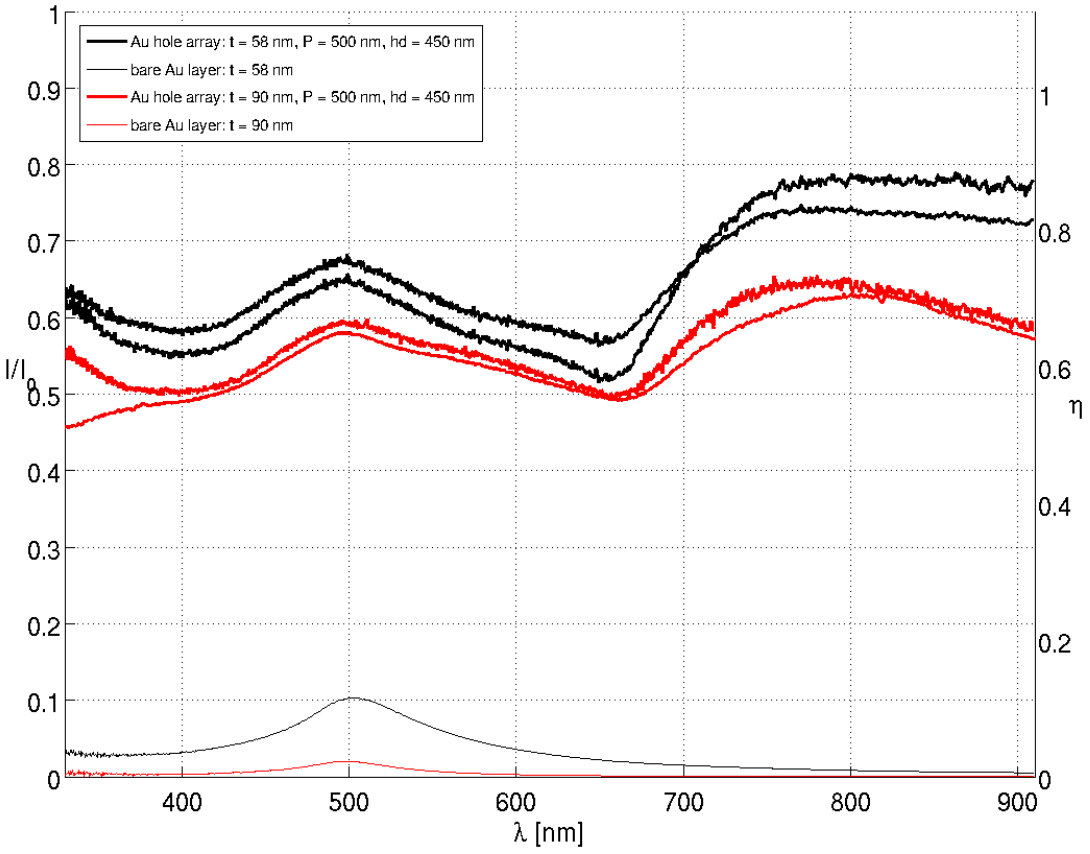

Figure 6.11: Relative transmission spectra of a Au hole array (hole diameter $d_{\text{hole}} = 450\,\text{nm}$) with varying layer thicknesses t.
Reference (I_0): transmission through glass substrate

The right hand side axes of both figures indicate the relative transmission normalized to the hole area stated as η. In the case of the hole array with hole diameter $d_{\text{hole}} = 450\,\text{nm}$ (Fig. 6.11) none of the graphs exceeds $\eta = 1$. In contrast to that the hole arrays with hole diameter $d_{\text{hole}} = 320\,\text{nm}$ (Fig. 6.12) both display enhanced transmission, i.e. $\eta > 1$, for the longer wavelength peak meaning that more light is transmitted through the holes as compared to the light incident on the area occupied by the holes. This enhancement is more pronounced at the hole array with thickness $t = 50\,\text{nm}$ but one has to care about the direct transmission of 2 % at

$\lambda = 900\,\text{nm}$ through the Au regions as well.

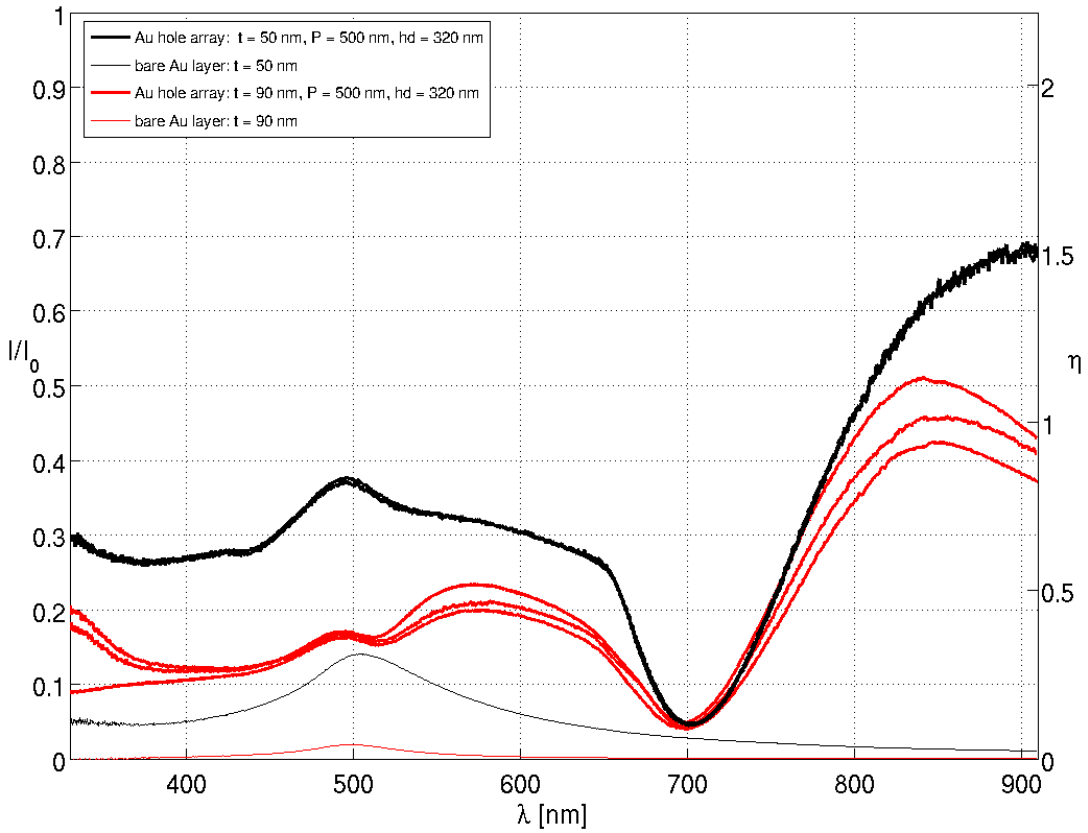

Figure 6.12: Relative transmission spectra of a Au hole array (hole diameter $d_{\text{hole}} = 320\,\text{nm}$) with varying layer thicknesses t.
Reference (I_0): transmission through glass substrate

Independent of the layer thickness the Au hole array with $d_{\text{hole}} = 320\,\text{nm}$ exhibits a well pronounced dip at $\lambda \approx 700\,\text{nm}$ with a strong transmission suppression. The relative transmission at this wavelength is less than 5 %.

6.2 Specific Resistivity

The specific resistivity of a 90 nm gold (Au) layer differently structured (unstructured layer, hole array, coated 500-nm-PS monolayer) is determined according to the Van der Pauw method (section 3.1.5).

The measurements are performed twice at an interval of one week to estimate the measurement errors additional to that of the used equipment indicated by the manufacturer. The measurement errors of the calculated quantities are evaluated due to their multiplicative relations by means of the "ln-method", i.e. one applies first the logarithm to the respective equation followed by the total differential and subsequently replaces the differentials with finite differences. The measurement error as regards the correction factor results from a possible reading error at the plot.

The specific resistivity of the unstructured 90 nm Au layer, three different layers are measured (Tab. 6.1), corresponds reasonably well with the literature value for Au: $\rho = 2.44 \cdot 10^{-6}\,\Omega\cdot\text{cm}$ [37].

Table 6.1: Specific resistivity of the unstructured Au layers

I	driven current
U	voltage drop at opposite contacts
R_1	mean resistance: $R_1 = \frac{U_{AB}+U_{CD}}{2\,I}$
R_2	mean resistance: $R_2 = \frac{U_{BC}+U_{DA}}{2\,I}$
f	correction factor, according to [24]
t	layer thickness
ρ	calculated specific resistivity, according to Eq. 3.4

	PS67	PS81	PS77
I [mA]	10.10 ± 0.01	10.00 ± 0.01	10.00 ± 0.01
U_{AB} [µV]	578 ± 5	145 ± 3	700 ± 15
U_{BC} [µV]	734 ± 12	2009 ± 4	451 ± 3
U_{CD} [µV]	578 ± 6	145 ± 3	700 ± 14
U_{DA} [µV]	733 ± 12	2009 ± 4	451 ± 3
R_1 [mΩ]	57.8 ± 0.6	14.5 ± 0.3	70.0 ± 1.5
R_2 [mΩ]	73.4 ± 1.2	200.9 ± 0.4	45.1 ± 0.3
ratio of resistances	1.27 ± 0.03	13.86 ± 0.31	1.55 ± 0.04
f	1 ± 0.01	0.65 ± 0.01	0.99 ± 0.01
t [nm]	90 ± 3	91 ± 3	90 ± 3
ρ_{Au} [Ω·cm]	$(2.68 \pm 0.13) \cdot 10^{-6}$	$(2.89 \pm 0.15) \cdot 10^{-6}$	$(2.32 \pm 0.16) \cdot 10^{-6}$

In the case of the coated 500-nm-PS monolayer the specific resistivity (Tab. 6.2) is about twice the bulk value but due to the coating procedure one deposits metal on top of the spheres as well as through the interstices on the glass substrate. In the narrow sense the requirements for the Van der Pauw method (section 3.1.5) are not fulfilled, namely a flat and homogeneous sample, and thus the calculated value for specific resistivity has actually no significance.

Table 6.2: Specific resistivity of Au-coated 500-nm-PS monolayers

I	driven current
U	voltage drop at opposite contacts
R_1	mean resistance: $R_1 = \frac{U_{\mathrm{AB}}+U_{\mathrm{CD}}}{2\,I}$
R_2	mean resistance: $R_2 = \frac{U_{\mathrm{BC}}+U_{\mathrm{DA}}}{2\,I}$
f	correction factor, according to [24]
t	layer thickness
ρ	calculated specific resistivity, according to Eq. 3.4

	PS81 pos1	PS81 pos2
I [mA]	10.00 ± 0.01	10.00 ± 0.01
U_{AB} [µV]	446 ± 3	2439 ± 32
U_{BC} [µV]	3594 ± 35	716 ± 23
U_{CD} [µV]	445 ± 4	2439 ± 33
U_{DA} [µV]	3593 ± 36	717 ± 23
R_1 [mΩ]	44.6 ± 0.4	243.9 ± 3.3
R_2 [mΩ]	359.4 ± 3.6	71.7 ± 2.3
ratio of resistances	8.06 ± 0.15	3.40 ± 0.13
f	0.73 ± 0.01	0.87 ± 0.01
t [nm]	91 ± 3	91 ± 3
$\rho_{\mathrm{Au_PS}}$ [Ω·cm]	$(5.93 \pm 0.39) \cdot 10^{-6}$	$(5.92 \pm 0.39) \cdot 10^{-6}$

The Au hole arrays doesn't meet the requirements of the Van der Pauw method neither (holes inside contacted area) but the contacts are single connected due to the small size of the holes. The measured data including the calculated specific resistivities are summarized in Tab. 6.3. The specific resistivities are quite well understandable considering the images from the optical microscope (Fig. 6.13 to Fig. 6.15). The contacts are labelled if visible.

Starting with the Au hole array (2) owing hole diameter $d_{\text{hole}} = 450\,\text{nm}$ the specific resistivity $\rho_{\text{hole}} = (1.17 \pm 0.09) \cdot 10^{-5}\,\Omega\cdot\text{cm}$ is approximately 4.5 times higher than the mean specific resistivity of the unstructured layer. Assuming that the specific resistivity is related to the area covered with metal the covered area would correspond to a fill factor (see section 5.4 for details) of approximately 0.22. Considering the packing errors of the fabricated Au hole array this value comes fairly close to the fill factor of a perfectly close-packed arrangement of $\zeta = 0.27$.

Table 6.3: Specific resistivity of Au hole arrays, different hole diameters

I	driven current
U	voltage drop at opposite contacts
R_1	mean resistance: $R_1 = \frac{U_{\text{AB}}+U_{\text{CD}}}{2I}$
R_2	mean resistance: $R_2 = \frac{U_{\text{BC}}+U_{\text{DA}}}{2I}$
f	correction factor, according to [24]
t	layer thickness
d_{hole}	hole diameter
ρ	calculated specific resistivity, according to Eq. 3.4

	PS67 - pos1	PS67 - pos2	PS77
I [mA]	1.000 ± 0.001	1.000 ± 0.001	10.00 ± 0.01
U_{AB} [µV]	511 ± 11	432 ± 8	241 ± 7
U_{BC} [µV]	844 ± 25	153 ± 5	1537 ± 19
U_{CD} [µV]	512 ± 12	426 ± 7	248 ± 9
U_{DA} [µV]	841 ± 23	158 ± 10	1540 ± 24
R_1 [mΩ]	512 ± 12	429 ± 8	24.5 ± 0.9
R_2 [mΩ]	843 ± 25	156 ± 10	153.9 ± 2.4
ratio of resistances	1.65 ± 0.09	2.8 ± 0.2	6.28 ± 0.33
f	0.99 ± 0.01	0.98 ± 0.01	0.77 ± 0.01
t [nm]	90 ± 3	90 ± 3	90 ± 3
d_{hole} [nm]	450 ± 16	450 ± 16	320 ± 9
ρ_{hole} [Ω·cm]	$(2.74 \pm 0.22) \cdot 10^{-5}$	$(1.17 \pm 0.09) \cdot 10^{-5}$	$(2.80 \pm 0.21) \cdot 10^{-6}$

Unfortunately the bonding of the second area (Au hole array (1), optical microscope images at Fig. 6.13) could not be realized without scratches. The calculated specific resistivity is approximately 2.3 times higher than that of the contacted area without scratches (Au hole array (2)). This increased value is probably linked to the scratches but a detailed conclusion

could not be drawn because of the violated requirement of the Van der Pauw method, namely holes inside the contacted area.

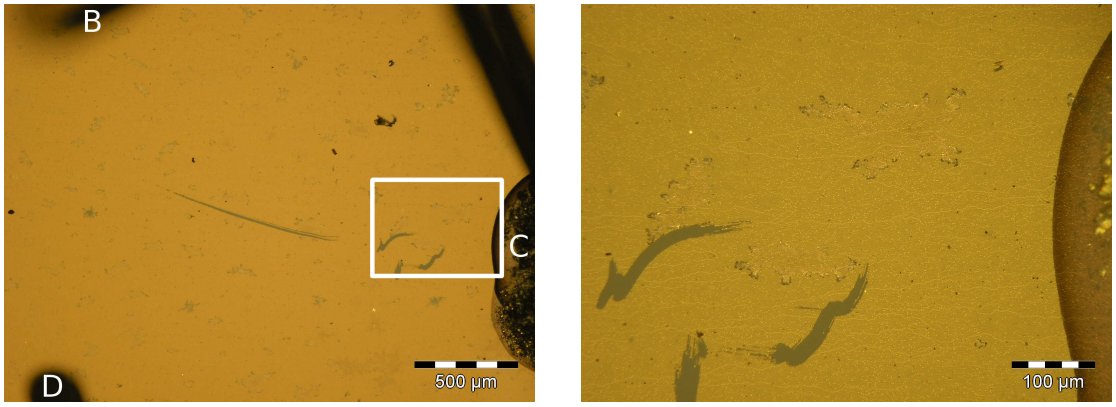

overview image detailed view

Figure 6.13: Contacted area of Au hole array (1): $t = 90\,\text{nm}$, $P = 500\,\text{nm}$, $d_{\text{hole}} = 450\,\text{nm}$
The white rectangle indicates the detailed view area.

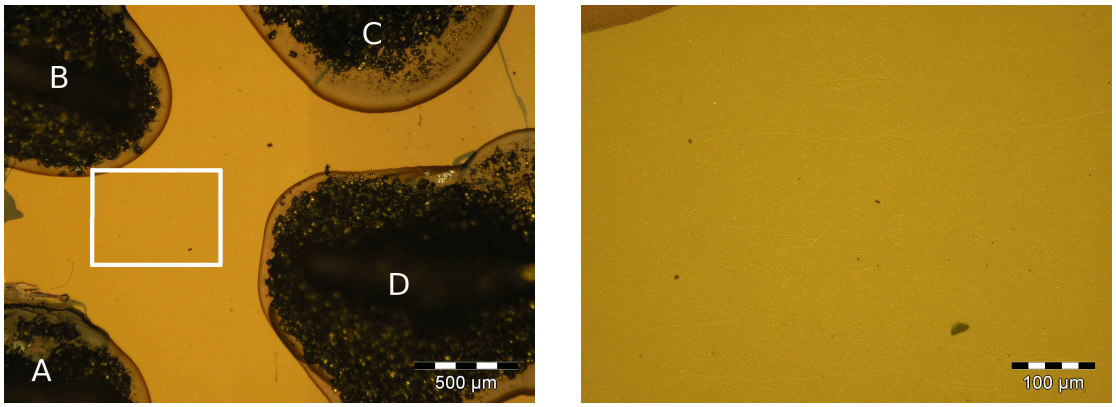

overview image detailed view

Figure 6.14: Contacted area of Au hole array (2): $t = 90\,\text{nm}$, $P = 500\,\text{nm}$, $d_{\text{hole}} = 450\,\text{nm}$
The white rectangle indicates the detailed view area.

The hole array with hole diameter $d_{\text{hole}} = 320\,\text{nm}$ evinces a specific resistivity in the range of that from the unstructured Au layer but checking the optical microscope images at Fig. 6.15 points out that this hole array still contains size reduced spheres which could not be removed both with the adhesion band and with dissolution in toluene.

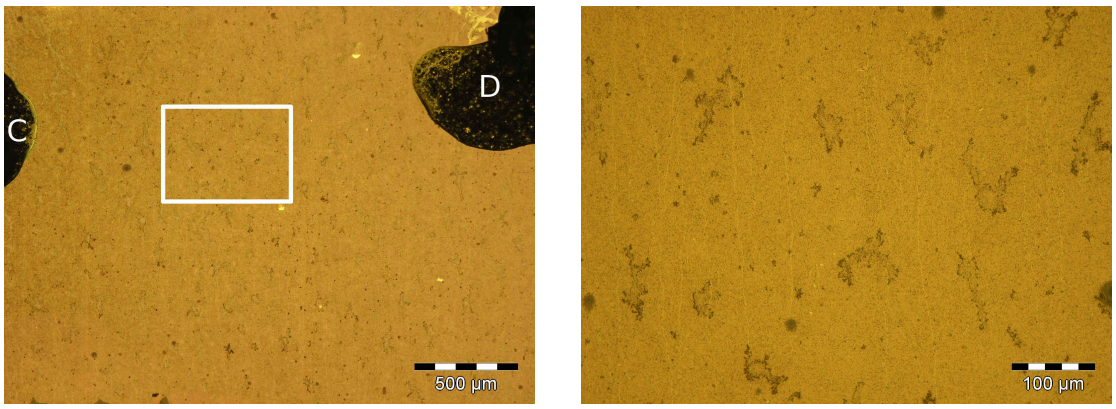

overview image detailed view

Figure 6.15: Contacted area of Au hole array (3): $t = 90\,\text{nm}$, $P = 500\,\text{nm}$, $d_{\text{hole}} = 320\,\text{nm}$ The white rectangle indicates the detailed view area.

6.3 Spectroscopic Ellipsometry

The dielectric function of Au hole arrays ($P = 500\,\text{nm}$, $d_{\text{hole}} = 450\,\text{nm}$, $t = 58\,\text{nm}$ and $t = 90\,\text{nm}$ respectively) is estimated by means of spectroscopic ellipsometry applying a microspot with spot diameter of 200 µm. Improving the accuracy of the obtained dielectric functions, the measurements are performed at two different angles of incidence (65° and 75°) yielding an effective spot ellipse with a major axes of approximately 475 µm and 775 µm respectively. The thickness of the arrays is assumed from the calibrated thermal evaporation procedure.

The thickness of the Cr adhesion layer is set to 1.5 nm instead of 3 nm taking into account that the dielectric function of Cr is only available for the bulk material. Varying the layer thickness between 1 nm and 3 nm, no significant change of the obtained results can be detected.

The ellipsometric spectra are adjusted with a single-wavelength fit using a multiple Gaussian oscillators model. Fig. 6.16 evinces the estimated dielectric functions for both Au hole arrays. This figure contains the respective values of the unstructured Au layer too. This data originates from transmission and reflectance measurements of thermally evaporated layers with thicknesses of 10 - 25 nm listed in [8].

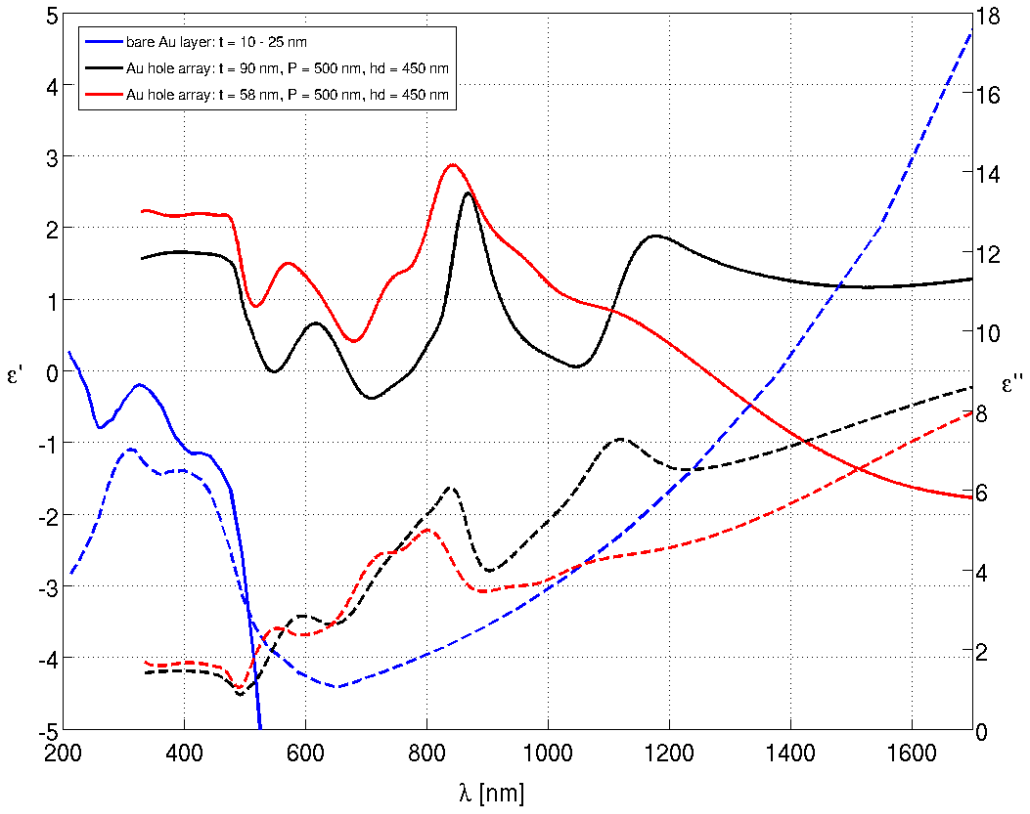

Figure 6.16: Dielectric functions of Au hole arrays with $P = 500\,\text{nm}$, $d_{\text{hole}} = 450\,\text{nm}$, $t = 90\,\text{nm}$ (black) or $t = 58\,\text{nm}$ (red) respectively compared to the dielectric function of a unstructured metal layer (blue)
The real part (ε') is plotted as solid line, the imaginary part (ε'') as dashed line

Apparently the dielectric functions of the patterned Au layers exhibit a totally different wavelength-dependence compared to that of the unstructured layer. This is true both for its real part ε' and for its imaginary part ε''. The thicker Au hole array ($t = 90\,\text{nm}$) shows an even more pronounced structure in ε' and ε'' especially for longer wavelengths. The real part ε' changes dramatically due to patterning with respect to profile and absolute value. At low energies (long wavelengths) the absolute value $|\varepsilon'|$ of the hole arrays is in the range of 1 while the respective value of the unstructured layer increases up to 160.

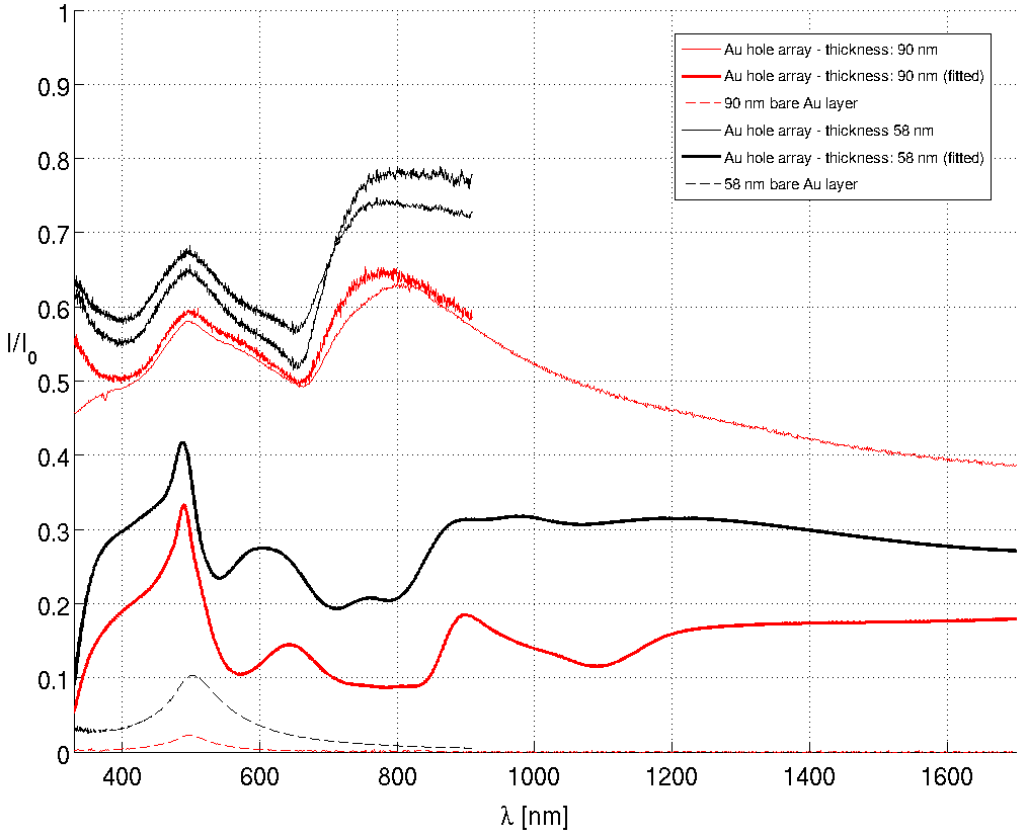

Figure 6.17: Measured and calculated transmission spectra of a Au hole array with different layer thicknesses t: period $P = 500\,\text{nm}$, hole diameter $d_{\text{hole}} = 450\,\text{nm}$. Reference ($I_0$): transmission through glass substrate

The estimated dielectric functions enable to calculate the relative transmission through the Au hole arrays. Fig. 6.17 evinces the calculated transmission spectra compared to the measured ones which feature 3 transmission resonances: one caused by the Au plasma resonance, the other ones by excitations of surface plasmons. Roughly considered, the calculated transmission spectra exhibit 3 transmission resonances too but except for the peak originating from the Au plasma resonance neither the peak positions nor the peak intensities coincide. This discrepancy seems to stem from the insufficient modeling of the surface plasmon influence on the transmission process and as consequence on the dielectric function too.
Nevertheless, these results again corroborate that the transmission through periodically patterned, optical thick metal films is mediated by surface plasmons at the metal - dielectric interfaces excited by the incident light.

7 Conclusion

This work demonstrates a rather simple and unconventional method called 'nanosphere lithography' to fabricate large areas of patterned thin metal films using the self-assembly of monodispersed spheres as template for etching and coating procedures. Based on close-packed monolayers of polystyrene (PS) spheres with diameters of 300 nm and 500 nm respectively, differently structured metal layers are obtained: PS sphere monolayers coated with gold or palladium and gold hole arrays each of cm^2 in area size. The hole periodicity of the gold hole arrays is determined by the sphere diameter.

This fabrication method enables to tailor the parameters of the fabricated structures, especially of the hole arrays, over a wide range: i) In principle all kinds of materials are usable assumed that the material can be deposited as homogeneous and uniform thin film. ii) Monodispersed spheres in an aqueous suspension are commercially available with diameters from about 50 nm to several micrometers facilitating to adapt the hole periodicity. iii) Different hole diameters are obtained by different etching times of the arranged sphere monolayers prior to the metal deposition. iv) With respect to the used sphere diameters the metal layer thickness can be varied within a wide range.

The periodic structure or in other words the photonic structure of the fabricated hole arrays favors its interaction with an incident beam of light which stimulates electron density oscillations right at the metal surface, so-called surface plasmons. At particular wavelength ranges depending on the periodicity of the array and on the dielectric properties of the involved media (metal and dielectric), this excitation possesses resonance character leading to an intense electromagnetic field in the surface of the patterned metal layer.

Based on this resonance amplification direct transmission measurements where the incident and the transmitted beam are collinear showing an exciting behavior: at resonant wavelengths more light is transmitted through the holes as compared to the light incident on the area occupied by the holes. In addition the transmission is almost suppressed at wavelengths where no surface plasmons are excited.

The intense electromagnetic field at the boundary between the metallic hole array and the dielectric give rise to potential future applications. There are already reports of applications in the field of molecule biosensing (surface plasmon resonance sensing) and spectroscopy (surface-enhanced Raman spectroscopy, surface-enhanced infrared spectroscopy). Furthermore a reduction in lifetime of fluorescent dyes deposited inside the holes as well as an efficiency enhancement of organic light emitting diodes using an aluminum hole array as cathode are observed.

The specific resistivity of gold hole arrays with hole diameter $d_{\mathrm{hole}} = 450\,\mathrm{nm}$ and periodicity $d = 500\,\mathrm{nm}$ as well as of the respective unstructured layer each exhibiting 90 nm of thickness

is estimated by means of the Van der Pauw method. The obtained value of the unstructured gold layer $\rho = (2.6 \pm 0.3) \cdot 10^{-6}\,\Omega\cdot\text{cm}$ corresponds well with the value of the bulk material indicated in literature. Comparing this specific resistivity to that of the hole array $\rho_{\text{hole}} = (1.17 \pm 0.09) \cdot 10^{-5}\,\Omega\cdot\text{cm}$, the result demonstrates that the specific resistivity scales with the metal fill factor $\zeta = 0.27$ of these hole arrays.

Investigations by means of spectroscopic ellipsometry of the gold hole arrays reveal a significant change of the dielectric function with respect to that of the unstructured layer: the wavelength dependence of both the real and the imaginary part of the dielectric function exhibits a more pronounced structure in the visible and near infrared wavelength range. The modelling of the dielectric function or rather the optical constants of unstructured layers is satisfactorily understood while the modelling of the patterned layers is insufficient at present. A comparision between the measured relative transmission spectra and the modelled ones demonstrates this mismatch.

Bibliography

[1] T.W. Ebbesen, H.J. Lezec, H.F. Ghaemi, T. Thio, and P.A. Wolff. Extraordinary optical transmission through sub-wavelength hole arrays. *Nature*, 391(6668):667–669, 1998.

[2] A.G. Brolo, E. Arctander, R. Gordon, B. Leathem, and K.L. Kavanagh. Nanohole-Enhanced raman scattering. *Nano Letters*, 4(10):2015–2018, 2004.

[3] A.G. Brolo, S.C. Kwok, M.G. Moffitt, R. Gordon, J. Riordon, and K.L. Kavanagh. Enhanced fluorescence from arrays of nanoholes in a gold film. *Journal of the American Chemical Society*, 127(42):14936–14941, 2005.

[4] S. Astilean. Noble-metal nanostructures for controlling surface plasmons and sensing molecules. *Radiation Physics and Chemistry*, 76(3):436–439, 2007.

[5] C. Liu, V. Kamaev, and Z.V. Vardeny. Efficiency enhancement of an organic light-emitting diode with a cathode forming two-dimensional periodic hole array. *Applied Physics Letters*, 86:143501, 2005.

[6] M. Born and E. Wolf. *Principle of Optics*. Cambridge University Press, 7th (expanded) edition, 2003.

[7] C. Kittel. *Introduction to Solid State Physics*. John Wiley & Sons, Inc., 8 edition, 2005.

[8] E.D. Palik. *Handbook of Optical Constants of Solids I and II*. Academic Press, Inc., 1985 / 1991.

[9] H. Raether. *Surface Plasmons on Smooth and Rough Surfaces and on Gratings*. Springer, 1988.

[10] C. Genet and T.W. Ebbesen. Light in tiny holes. *Nature*, 445(7123):39–46, 2007.

[11] S.G. Rodrigo, F.J. García-Vidal, and L. Martín-Moreno. Influence of material properties on extraordinary optical transmission through hole arrays. *Phys. Rev. B*, 77(7):075401, 2008.

[12] Center for Nanolithography Research, Rochester Institute of Technology. Optical Properties of Thin Films for DUV and VUV Microlithography. `http://www.rit.edu/kgcoe/microsystems/lithography/thinfilms/thinfilms/thinfilms.html`. accessed September 29, 2009.

[13] L.I. Maissel and R. Glang. *Handbook of Thin Film Technology*. McGraw-Hill, Inc., 1970.

[14] J.D. Joannopoulos. *Photonic Crystals - Molding the Flow of Light.* Princeton University Press, 2nd edition, 2008.

[15] S. Kinoshita, S. Yoshioka, and J. Miyazaki. Physics of structural colors. *Reports on Progress in Physics*, 71(7):076401, 2008.

[16] F.J. García de Abajo. Colloquium: Light scattering by particle and hole arrays. *Reviews of Modern Physics*, 79(4):1267–1290, 2007.

[17] M. Dragoman and D. Dragoman. Plasmonics: Applications to nanoscale terahertz and optical devices. *Progress in Quantum Electronics*, 32(1):1–41, 2008.

[18] R. Gordon, A.G. Brolo, D. Sinton, and K.L. Kavanagh. Resonant optical transmission through hole-arrays in metal films: physics and application. *Laser & Photonics Review*, pages 1–25, 2009.

[19] C. Genet, M.P. van Exter, and J.P. Woerdman. Fano-type interpretation of red shifts and red tails in hole array transmission spectra. *Optics Communications*, 225(4-6):331–336, 2003.

[20] J. Braun, B. Gompf, G. Kobiela, and M. Dressel. How holes can obscure the view: Suppressed transmission through an ultrathin metal film by a subwavelength hole array. *Physical Review Letters*, 103(20):203901, 2009.

[21] N. García and Ming Bai. Theory of transmission of light by sub-wavelength cylindrical holes in metallic films. *Optics Express*, 14(21):10028–10042, 2006.

[22] A.G. Brolo, R. Gordon, B. Leathem, and K.L. Kavanagh. Surface Plasmon Sensor Based on the Enhanced Light Transmission through Arrays of Nanoholes in Gold Films. *Langmuir*, 20(12):4813–4815, 2004.

[23] H. Kiessig. Interferenz von röntgenstrahlen an dünnen schichten. *Annalen der Physik*, 402:769–788, 1931.

[24] L.J. Van der Pauw. A method of measuring specific resistivity and hall effect of discs of arbitrary shape. *Philips Research Reports*, 13:1–9, 1958.

[25] C.L. Haynes and R.P. Van Duyne. Nanosphere lithography: A versatile nanofabrication tool for studies of Size-Dependent nanoparticle optics. *The Journal of Physical Chemistry B*, 105(24):5599–5611, 2001.

[26] Y. Xia, B. Gates, Y. Yin, and Y. Lu. Monodispersed colloidal spheres: Old materials with new applications. *Advanced Materials*, 12(10):693–713, 2000.

[27] F. Burmeister, C. Schäfle, B. Keilhofer, C. Bechinger, J. Boneberg, and P. Leiderer. From mesoscopic to nanoscopic surface structures: Lithography with colloidal monolayers. *Advanced Materials*, 10(6):495–497, 1998.

[28] N. Denkov, O. Velev, P. Kralchevski, I. Ivanov, H. Yoshimura, and K. Nagayama. Mechanism of formation of two-dimensional crystals from latex particles on substrates. *Langmuir*, 8(12):3183–3190, 1992.

[29] F. Jarai-Szabo, S. Astilean, and Z. Neda. Understanding self-assembled nanosphere patterns. *Chemical Physics Letters*, 408:241–246, 2005.

[30] R. Micheletto, H. Fukuda, and M. Ohtsu. A simple method for the production of a Two-Dimensional, ordered array of small latex particles. *Langmuir*, 11(9):3333–3336, 1995.

[31] Antony S. Dimitrov and Kuniaki Nagayama. Continuous convective assembling of fine particles into Two-Dimensional arrays on solid surfaces. *Langmuir*, 12(5):1303–1311, 1996.

[32] G.S. Oehrlein. *Reactive Ion Etching*. Handbook of Plasma processing Technology. Noyes Publications, 1990.

[33] C. Haginoya, M. Ishibashi, and K. Koike. Nanostructure array fabrication with a size-controllable natural lithography. *Applied Physics Letters*, 71(20):2934–2936, 1997.

[34] H. Sormann. Least-Squares-Approximation. In *Numerische Methoden in der Physik*. Institut für Theoretische Physik, TU Graz, 2006.

[35] L. Landström, D. Brodoceanu, K. Piglmayer, and D. Bäuerle. Extraordinary optical transmission through metal-coated colloidal monolayers. *Applied Physics A*, 84(4):373–377, 2006.

[36] L. Landström, D. Brodoceanu, D. Bäuerle, F.J. Garcia-Vidal, S.G. Rodrigo, and L. Martin-Moreno. Extraordinary transmission through metal-coated monolayers of microspheres. *Optics Express*, 17(2):761–772, 2009.

[37] D.R. Lide. *Resistivity of Metals*. Handbook of Chemistry and Physics. CRC Press, 1996.